LIU, YIYANG, PH.D. Metal (Manganese) Oxide Based Nano-Architectures and Supercapacitor Materials in Energy Storage Applications. (2017)
Directed by Dr. Jianjun Wei. 147 pp.

This study describes the growth mechanism, magneto-capacitance enhancement and separator-free design of α-MnO_2 on super-aligned electrospun carbon nanofibers (SA-ECNFs) as electrode materials for supercapacitor energy storage. The morphology of the SA-ECNFs/MnO_2hybrid electrodes were investigated by scanning electron microscope (SEM). The composite and crystal information was characterized by X-ray photoelectron spectroscopy (XPS), Energy-dispersive X-ray spectroscopy (EDX) and X-Ray Diffraction Spectroscopy (XRD). The energy storage performance was tested by cyclic voltammetry (CV), electrochemical impedance spectroscopy (EIS) and galvanostatic charging/discharging techniques. A time-dependent MnO_2 film growth analysis suggests a three-step kinetics mechanism for the electrodeposition of MnO_2 on SA-ECNFs and a self-cessation ending. The SA-ECNFs/MnO_2 hybrid electrodes provide with high specific capacitance energy storage. The MnO_2-modified ECNFs electrode presents mT magneto-energy storage enhancement ability due to the polarization of unpaired electrons' contribution in increased pseudocapacitance. Manipulation of the thickness of MnO_2 film suggests an ultra-thick MnO_2 coating capable for separator-free configuration for a supercapacitor. A bi-functional model of the MnO_2 film is proposed to explain its potential

to assemble a device without the use of separator, which, for the first time, demonstrates the supercapacitance energy storage.

METAL (MANGANESE) OXIDE BASED NANO-ARCHITECTURES AND SUPERCAPACITOR MATERIALS IN ENERGY STORAGE APPLICATIONS

by

Yiyang Liu

A Dissertation Submitted to
the Faculty of The Graduate School at
The University of North Carolina at Greensboro
in Partial Fulfillment
of the Requirements for the Degree
Doctor of Philosophy

Greensboro
2017

Approved by

_____
Committee Chair

APPROVAL PAGE

This dissertation written by YIYANG LIU has been approved by the following committee of the Faculty of The Graduate School at The University of North Carolina at Greensboro.

Committee Chair_____

Committee Members_____

_____

_____

_____

Date of Acceptance by Committee

_____

Date of Final Oral Examination

ACKNOWLEDGEMENTS

First, I extend my most heartfelt appreciation to Dr. Jianjun Wei, my advisor for his unwavering support from the very beginning of my time as a Ph.D. student. Not just as a great research advisor, but as a mentor in life offering insightful guidance and keen editing throughout my research and writing.

I want to thank other professors in the Joint School of Nanoscience and Nanoengineering. Prof. Lifeng Zhang, Prof. Joseph M Starobin and Prof. Hemali Rathnayake are members of my Dissertation Committees; Dr. Daniel Herr put a lot of efforts in editing my proposal work. I'm truly thankful to each of you for your willingness to share your immense knowledge in the field.

I also want to thank all my collaborators, Dr. Zheng Zeng for analyzing/modeling of the MnO_2 growth & magnetic properties; Dr. Alex Aboagye and Spero Gbewonyo for training me and help me with electrospun setup; Dr. Bloom Brian in University of Pittsburgh for XPS analysis.

With my respectful heart, I'd like to thank my former advisors Prof. Xianshun Zeng in Tianjin University of Technology and Prof. Yongsheng Chen in Naikai Univerity. Their extremely hard working and unbreakable perseverance had lifetime impressions on me.

Special thanks to my former collaborators Shanshan Huang, Prof. Yingpeng Wu & Dr. Lu Huang (and "Dr." Yiyi Wu in the future). They were my elder sisters & brother in the lab, taught me organic synthesis, UV-Vis & fluorescent microscopy, CNT & graphene synthesis & characterization and supercapacitor assembling. I'd also like to thank Dr. Yan Wang, Dr. Dong Sui, Mrs. Xuan Li, Dr. Long Zhang, Dr. Xi Yang, Dr. Yi Zuo, Dr. Tengfei Zhang, Dr. Yi Zhang, Dr. Miaomiao Li & Dr. Wang Ni, Dr. Fan Zhang & Dr. Ningbo Yi, Prof. Qian Zhang, Dr. Kai Leng, Dr. Bin Kan in Nankai University. They were my former colleagues, and will be my sincere friends in the rest of my life.

It’s my pleasure to work with a group of warmhearted and lovely people in JSNN, Wendy Zhang, Bhawna Bagra, Zuowei Ji, Ziyu Yin, Taylor Mabe, Alex Sheardy, Durga Arvapalli, Harish Chevva.

Overall, the boundless love, encouragement, and support from my family are my most cherished possessions.

TABLE OF CONTENTS

Page

LIST OF TABLES

Page

LIST OF FIGURES

Page

CHAPTER I

INTRODUCTION

This chapter has been published as: Y. Liu, Z. Zeng, J. Wei,* Nano-architectured Carbon-metal Oxide Electrodes for Supercapacitance Energy Storage, *Handbook of Nanoparticles and Architectural Nanostructured Materials*, Elsevier Publisher, 2017, In press.

I.I An Overview

Since the fossil fuel depletion has been identified as a future challenge, the needs of efficient, renewable, sustainable energy sources are very urgent in the long term. Energy storage systems, such as fuel cells, batteries and supercapacitors, are good power sources for electronic devices ranging from cellphones to vehicles. Electrochemical double layer capacitors (EDLC), are promising energy storage devices which provide higher energy density than conventional capacitors and higher power density than batteries, hence drawn a lot of attention due to their unique characteristics, such as high power density, fast charging/discharging rate, large cycling stability, and safety. There is an unmet need to develop a breakthrough solution that would complement existing EDLC structures with significantly enhanced energy storage capacity.

EDLC coupled with active materials (usually transition metal oxides) was developed in the past decade since it can enhance the energy density while maintaining a good cyclic performance which is categorized as supercapacitors (also called pseudo-

capacitors). In recent years, research on the topic of supercapacitors has greatly reduced since the overall performance is decreasing when large amount of active materials was introduced into the system. Therefore, there's an urgent need of the fundamental mechanism study of the active materials including their formation, crystallization, and potential enhancement during energy storage processes when their mass loading is high.

In this work, I describe the studies of energy storage through a super-aligned carbon fibers film with the deposition of manganese dioxide. In this chapter, a brief indroduction of fundamental energy storage mechanism, along with the review of studies in different platforms such as carbon-based nano-architectures, carbon-metal oxides-based nano-architectures, etc. for supercapacitors applications was introduced. In chapter II, a low-current electrodeposition of the α-MnO_2 film was described by a three-stage growth process offering a structure and crystal study during the high mass loading of MnO_2. The first step involves small cluster formation on a boundary layer distributed along the fibers (0-2 h). The second step involves "kebab"-like structure formation and growth from small to big nodules of MnO_2 around the SA-ECNF (2-4 h). The final step involves the cessation of MnO_2 nodule growth and establishment of a dense film with a self-limiting thickness (>4 h). In chapter III, I present a magnetization-induced capacitance enhancement in MnO_2/ECNFs nanocomposite electrodes fabricated by electrochemical deposition of MnO_2 on ECNFs. Experimental performance and data analysis indicate that the magnetic susceptibility largely increases the charge transfer rate thus improves the pseudo-reactions

of MnO_2 at the electrode and interfaces. A supercapacitor nanocomposite electrode composed of MnO_2 deposition on ECNFs exhibits significantly enhanced galvanostatic charge/discharge cycling at a 1.34 mT of magnetic field, suggesting that the enhanced magneto-supercapacitive performance is mainly attributed to magnetic susceptibility of the MnO_2 in the electrode because of the improvement of the pseudocapacitive behavior at the electrode and the electrode/electrolyte interfaces. In chapter IV, a separator-free configuration in which ultra-thick MnO_2 layers functions as both the pseudo-material and separator was presented. For the first time, we found the relationship between the thickness of deposited metal oxide and energy density generated from the electrode. To elucidate this, the important factor, h_{total}, should be divided into two parts: MnO_2 thickness as a pseudocapatance role (h_{ps}) and as a separator role (h_{sep}). Herein, h_{ps} contributes to the reversible redox reactions between Mn(IV)/Mn(III) species and K^+ intercalation/de-intercalation at the MnO_2/electrolyte interfaces while h_{sep} applies high resistance between two electrodes while allowing free ions to flow. Furthermore, since the h_{sep} is ascribed to different electrodeposition currents, to balance the pseudocapacitance role with the separator role of MnO_2, an optimal electrodeposition current (I_{opt}) should be modeled. Chapter V summarizes all the energy storage methodologies or mechanisms examined in this thesis work and provides a brief perspective comment on future research.

I.II A Brief Review

Energy drives the evolution of nature and human beings since the beginning of creation. However, modern civilization along with industrial revolution rapidly accelerates the consumption of fossil fuel energy and lead to serious greenhouse gas emissions and environmental pollution. Facing these challenges, humankind is forced to move towards efficient, renewable, sustainable energy sources.[3]

Energy storage systems, such as fuel cells, batteries, and supercapacitors, are good power sources for electronic devices ranging from cellphones to vehicles. Among these energy storage technologies, fuel cells have the highest energy density, but their power densities are the lowest and unit size/weight is large.[4] Batteries have high energy density, but their power densities are low and cycle lives are limited.[5]

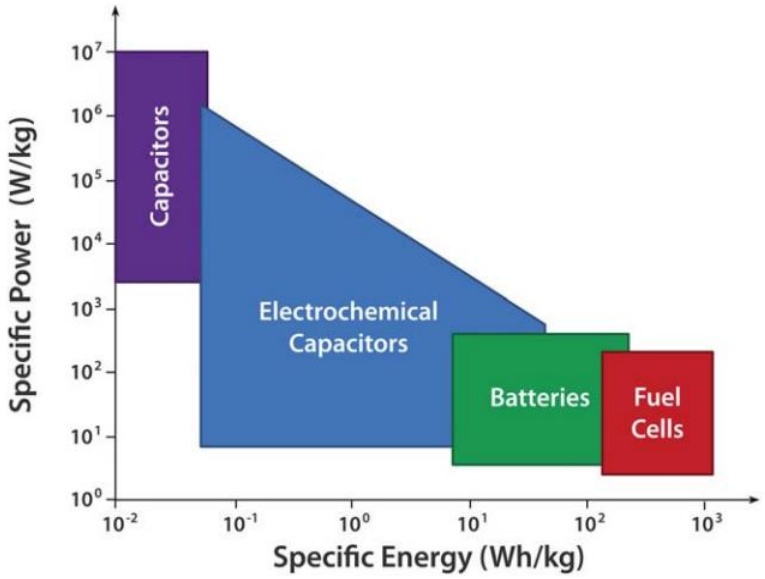

Figure 1.1. Specific Power as a Function of Specific Energy for Various Energy Storage Devices.[4]

Supercapacitors are promising energy storage devices which provide much higher energy density than conventional capacitors and higher power density than batteries (Figure 1.1), hence they have drawn a lot of attention due to their unique characteristics, such as high power density, fast charging/discharging rate, and large cycling stability.[4, 6, 7] However, the lower energy density limits its applications as compared to batteries. For example, carbon-based electrochemical double layer capacitors usually have energy density less than 10 Wh/kg, which is much lower than that of lead-acid batteries (33-42 Wh/kg)[8] and lithium-ion batteries (100–265 Wh/kg).[9] Such low energy density cannot fulfill the need of energy storage devices for vehicles and power plants. Thus there is a great demand for improving both capacitance and energy density of supercapacitors.

Batteries including primary battery (e.g. alkaline, lead acid) and secondary battery (e.g. silver zinc, lithium-ion) are dominating in use for portable devices.[10] There is a 1354% increase in the global market of supercapacitors in comparison to a 174% increase of battery. While based on the data in Figure 1.1 the performance of supercapacitors is still limited in energy density. Therefore, the potential supercapacitors market is huge and a breakthrough strategy is needed which can complement existing electrochemical double layer capacitors with significantly enhanced energy storage capacity. Fundamentally, supercapacitors use electric double layer capacitance (EDLC) or pseudocapacitance or a combination of both to store charges.

I.III Electric Double Layer Capacitance (EDLC)

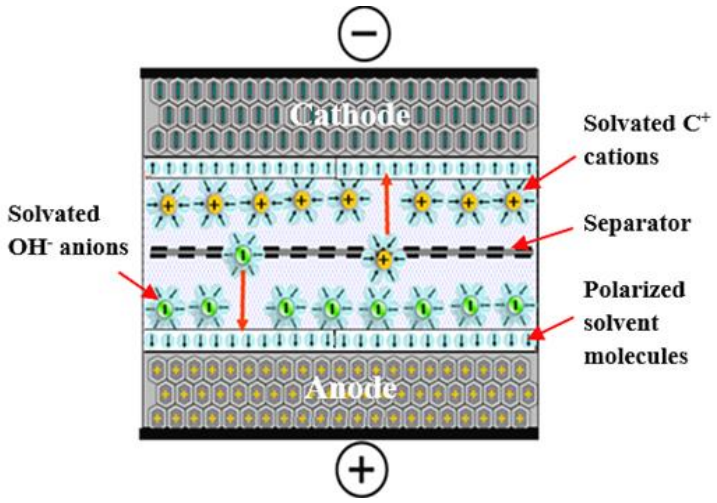

Figure 1.2. Scheme of Formation of Electric Double Layers.

EDLC comes from a capacitor consisting of electrolyte as the dielectric media, permeable membrane (usually nonwoven fiber or polymer film) as a separator, and conductive (usually carbon derived) materials as electrodes. For the formation of electric double layers as Figure 1.2 shown, the solvated anions and cations are polarized toward anode and cathode during a charging process. Then the polarized anions and cations move backward carrying charges when an external circuit is connected between the two electrodes, which is also called discharge. For the electrochemical (EC) activity center, high-performance electric double layer capacitors usually utilize activated carbon nanotubes, graphene, reduced graphene oxides (rGO), or carbon nanoparticles as electrodes since its capacitance is proportional to the surface area of the electrodes.

I.IV Pseudocapacitance

Pseudocapacitance comes from the processes when specific cations and anions were desolvated-adsorbed between the electrolyte and active materials (usually transition metal oxides) on the electrode as Figure 1.3 shown. It can be categorized as a faradaic charge transfer process which includes reversible faradaic redox, electrosorption or intercalation.

Equation (1.1) – (1.4) further describe these processes, including reversible faradaic redox reaction, intercalation, electrosorption or any of the combination when hybrid active materials are introduced.[2]

Redox system: $O_x + ne^- \leftrightarrow Red$ (1.1)

Intercalation system: $M_y + xLi + xe^- \leftrightarrow Li_xM_y$ (1.2)

Electrosorption system: $(MO)S + C^+ + e^- \leftrightarrow (C^+MO^-)S$ (1.3)

or $H^+ + e^- + S \leftrightarrow SH$ (1.4)

where O_x is the oxidizing agent, Red is the reducing agent, M is the transition metal (e.g., Mn, Fe, Ni, Co, Ti, or hybrid), C^+ is the insertion cations (e.g., Li^+, K^+, Na^+, Al^{3+}), and S is the surface lattice site.

A carbon nanomaterials-based pseudocapacitor usually has pseudocapacitance comes from the reversible reactions of the active materials in addition to double layer capacitance formed on electrode surface, which can largely improve the faradaic electron charge-transfer efficiency.

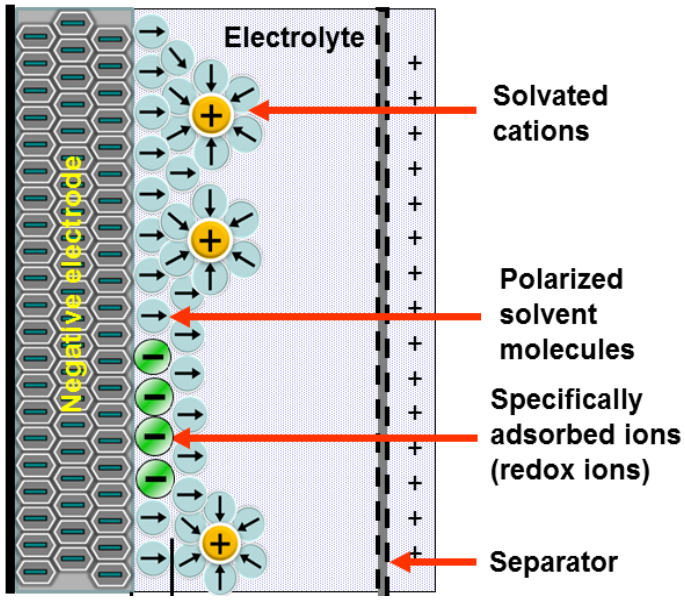

Figure 1.3. Scheme of a Pseudocapacitance Electrode.

In this chapter, recent progress on nano-architectured CNM and MO-CNM composites for high electrochemical performance supercapacitors will be introduced. The advanced design in terms of the critical parameters, e.g., architecture, specific surface area, mass loading will be presented and discussed in detail.

I.V Carbon Nano-architecture

Carbon nanomaterial (CNM), such as carbon nanotube (CNT), carbon nanotube forest (CNTF), graphene, reduced graphene oxide (rGO), templated graphene foam (TGF), carbon onion/sphere (CO/CS) and electrospun carbon nanofiber (ECNF), possesses unique sizes, surface dependent (e.g., morphological) properties and excellent intrinsic physical (e.g., electrical, thermal and mechanical) properties which are ideal for application in supercapacitors. Since CNT[3] and rGO[4] had been introduced to the applications of supercapacitors, tremendous progress has been made in the period of 1999-2010 including, but not limited to, zero-dimensional carbon nanoparticles (e.g. CO/CS),[5, 6] one-dimensional highly densely packed single-walled carbon nanotubes (SWNT),[7] one-dimensional ECNF,[8] and two-dimensional graphene-based Supercapacitors.[9]

In 2006, a study of a controlled synthesis of carbide-derived carbons showing that specific surface area (SSA, normally analyzed by Brunauer–Emmett–Teller (BET) method) and pore size are key factors of EDLC (Figure 1.4).[11] Inspired by this study, a universal model with equations (1.5)–(1.7) for nanoporous carbon materials was built to accurately estimate the contributions of pores with different sizes.[10]

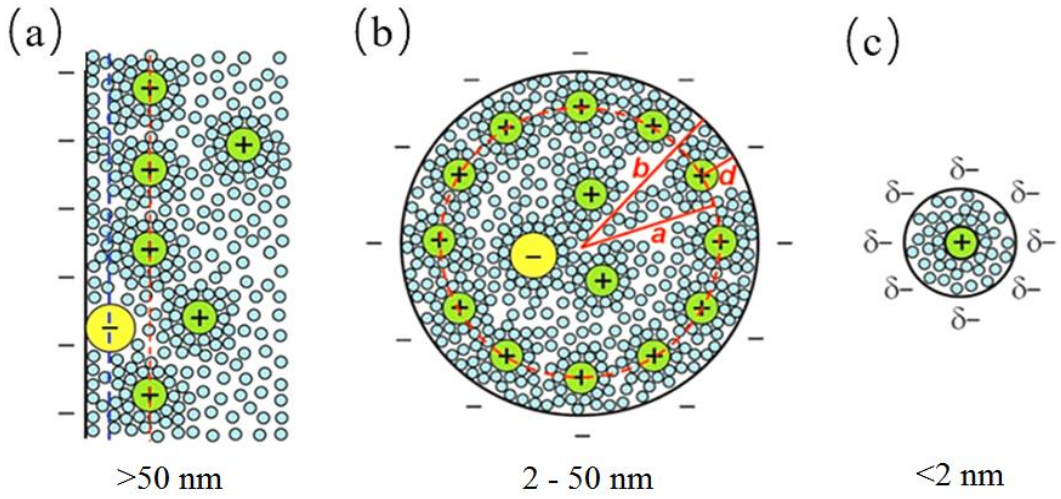

Figure 1.4. Schematic Diagrams (a) an Electric Double-layer Formed at the Carbon/electrolyte Interface (Anode). The inner and outer Helmholtz planes are represented by blue and red dashed lines (distance d), respectively. Cations are shown to be solvated by the solvent molecules. (b) a negatively charged mesopore with solvated cations approaching the pore wall to form an electric double-cylinder capacitor with radii b and a for the outer and inner cylinders, respectively, separated by a distance d, and (c) a negatively charged micropore of radius b with solvated cations of radius a_0 lining up to form an electric wire-in-cylinder capacitor. Reproduced with permission from [10].

Macropores (> 50 nm): $C = \varepsilon_r \varepsilon_0 A/d$ (1.5)

Mesopores (2 – 50 nm): $C = 2\pi\varepsilon_r \varepsilon_0 L/\ln(b/a)$ (1.6)

Micropores (< 2 nm): $C = 2\pi\varepsilon_r \varepsilon_0 L/\ln(b/a_0)$ (1.7)

where ε_r is the electrolyte dielectric constant, ε_0 is the permittivity of a vacuum, A is the SSA of the electrode, d is the thickness of the double layer and L is the pore length. As a milestone, it summarizes that the performance of EDLC capacitors can be estimated by three factors: SSA, pore size distribution (PSD) and conductivity.

A lot of efforts have been put into enlarging SSA of CNM with multiple techniques, e.g. control oxidation,[12] KOH thermal activation,[13] and microwave activation.[9] In 2010, a ‘‘surface-only solid’’ was synthesized by slowly heating the electrodes in dry air to a target temperature.[12] The SSA increment of the SWNT forests from 1300 m^2/g to 2240 m^2/g grants the electrode high energy (24.7 Wh/kg) and power (98.9 kW/kg) densities along with specific capacitance of 114 F/g. The novel “stretch out” process (Figure 1.5 inset) illustrates a new route for CNT activation.

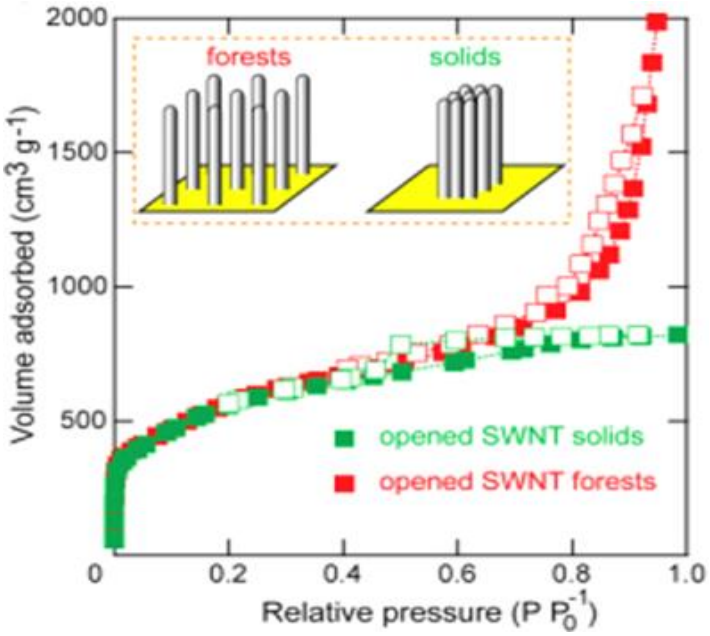

Figure 1.5. N_2 Adsorption and Desorption Isotherm of Opened-forests (Red) and Opened-solid (Green). The inset diagram depicts density difference between forest and solid. Reproduced with permission from [12].

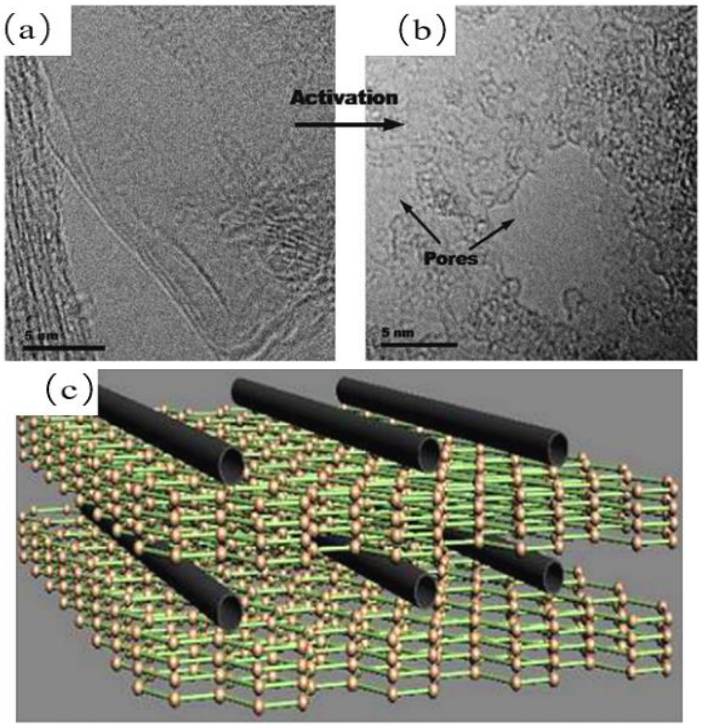

Figure 1.6. The High-resolution Transmission Electron Microscopy Images Before (a) and After (b) Activation. The graphene in (a) shows a smooth surface and (b) demonstrates the porous morphology. The arrows in (b) show the pores caused by the activation. (c) The illustration of SWNT grown between the graphene sheets, forming a unique network CNM. Reproduced with permission from [14].

In 2012, an in-situ synthesis of a hybrid structure of SWNT and graphene by arcing-discharge method was reported.[14] This unique sandwich-like structure (Figure 1.6c) offers channels and pores for electrolyte ions to penetrate. The SSA analysis shows an increase from 65 m^2/g to 190 m^2/g after KOH activation, which brings one of the best specific capacitance of 350 F/g among CNT or rGO electrodes. A high energy density of 68 Wh/kg with no decrease after 8000 cycles was observed. This work indicates a powerful and effective technique to enlarge the SSA of CNM.

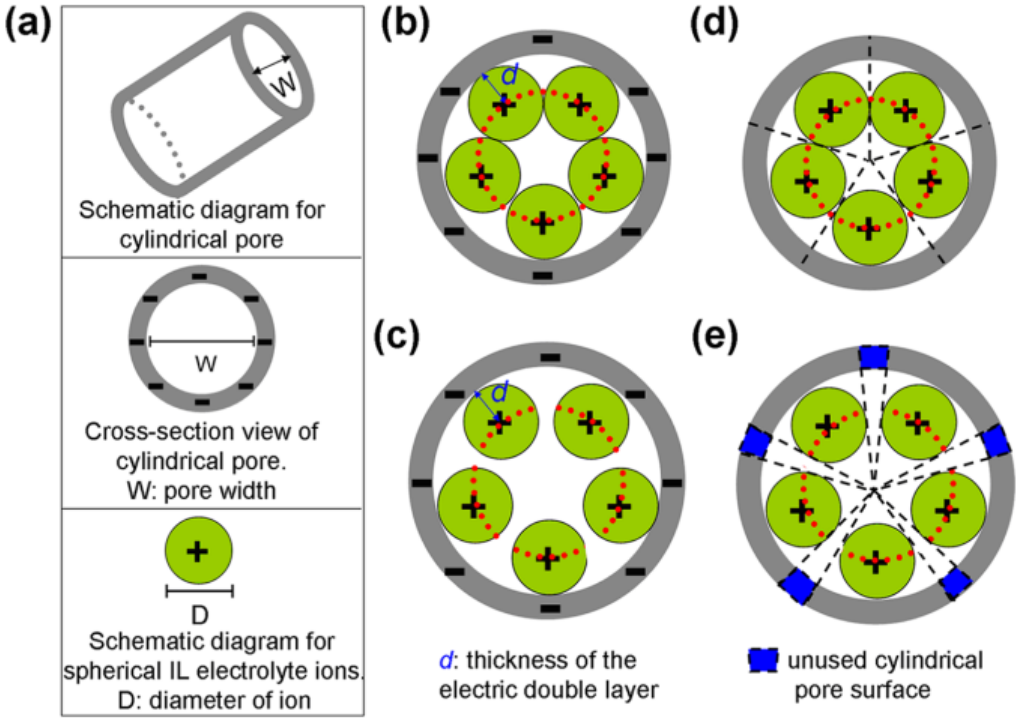

Figure 1.7. (a) Schematic Diagrams of Cylindrical Pore, Cross-section of Cylindrical Pore and Spherical IL Electrolyte Ions. The gray cycle represents the cylindrical pore wall with negative charges and the green ball represents the cations of IL electrolytes. Schematic diagrams of IL electrolyte ion packing mode in pores at the state of (b) tightly stacked ions together because of the completely matching between the ion and pore size and (c) not tightly stacked together due to mismatch. The d value is equal to the radius of electrolyte ions for both the two states. Schematic diagrams (d) and (e) for the utilized cylindrical pore surface in the states of (b) and (c). The blue part in (e) represents the unused or wasted cylindrical pore surface.[15]

In 2013, a detailed study of the SSA and pore size control of sp^2 carbon materials and their impacts on capacitance performance was realized.[15] Hydrothermal carbonization of different carbon sources has been done to control the SSA of the sp^2 carbon products. Furthermore, the as-prepared sp^2 carbon materials were treated with various chemicals (KOH, NaOH, K_2CO_3, $ZnCl_2$, H_3PO_4, and CaO) and various mass

ratio/temperature to control the PSD. Equation (1.8) has been established for specific capacitance calculation after a full study of the SSA (i.e. cumulative nonlocal-density-functional-theory-SSA of pores with size above the diameter of positive ions in ionic liquid (IL) electrolytes) of different sp^2 carbon materials, which is in good agreement with experimental results.

$$\mathrm{C(F/g)} = 0.142 \times \mathrm{SSA(m^2/g)} - 7.8 \quad (1.8)$$

The studies in this section have shown advances in increasing SSA and controlling PSD of CNM to acquire high EDLC solely for supercapacitors applications. Moreover, several fundamental strategies should be considered in the design of EDLC capacitors: 1. Solvated ions have a "dimensional effect" when ions' radii approached the pore size,[16] thus appropriate electrolyte should be considered based on given pore volume and PSD; 2. Mesopores with preferred length/diameter ratio can facilitate ion transport by providing entries to millions of micropores, which play the main role in both electroadsorption processes and electrodes' capacitance;[17] 3. Since non-solvated ions have smaller radii which may fit into ultra-micropores (< 0.7 nm), electrolyte such as IL is promising in nano-architectures with small pore sizes.

Transition MO (e.g., ruthenium(IV) oxide (RuO_2), manganese(IV) dioxide (MnO_2), Iron(II, III) oxide (FeO, Fe_2O_3), nickel(II) oxide (NiO), cobalt(II, III) oxide (CoO, Co_2O_3), nickel cobaltite ($NiCo_2O_4$), etc.) have been widely used in the studies of pseudocapacitors

as active materials due to their ultra-high theoretical specific capacitance (up to ~3560 F/g). However, the theoretical value of the active materials has rarely been achieved in experiment due to their limited electric conductivities. Thus, a series of CNM (e.g. CNT, CNTF, rGO, TGF, ECNF, etc.) were introduced into the systems to create a high electric conductive region to increase the electron charge transfer efficiency of these materials.

I.VI Carbon Nanotubes (CNT) Metal Oxide Nano-architecture

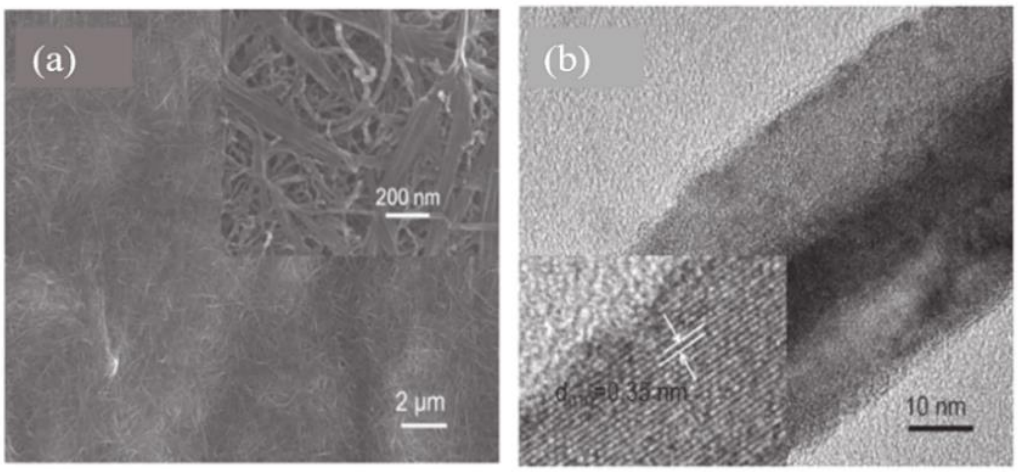

Figure 1.8. (a) Scanning Electron Microscope (SEM) Images of a Representative CNT-V_2O_5 Nanocomposite Film Containing 18 wt% of CNT. The same film etched by 1 wt% hydrogen fluoride solution (inset); (b) TEM and HRTEM (inset) images of a V_2O_5 nanowire with a layered crystalline structure. Reproduced with permission from [19].

CNT is well-known for the electrode materials of electrochemical energy storage devices owing to its unique tubular structures (high length to diameter ratio (up to 132,000,000:1)), excellent chemical stability, intrinsically metallic property and large SSA.[18] Furthermore, the electrical, optical and thermal properties of the CNT are

extremely anisotropic and tunable compared to those of typical semiconductors, which make it one of the most attractive materials in recent decades.

In 2011, a facial one-step hydrothermal fabrication of the CNT-V_2O_5 composites was reported.[19] The large voltage window of V_2O_5 allows the electrode to operate between 2.2 V – 4 V (vs. Li/Li^+) organic electrolyte. An energy density of 40 Wh/kg at a power density of 210 W/kg was achieved. While the relatively low specific capacitance (115 F/g) may attribute to its intertwined structure (Figure 1.8a inset) and densely formed MO layer (Figure 1.8b), which can lower the contact area between MO and electrolyte resulting in a moderate SSA (125 m^2/g). The retention of ~80% after 10,000 cycles benefits from the densely grown MO.

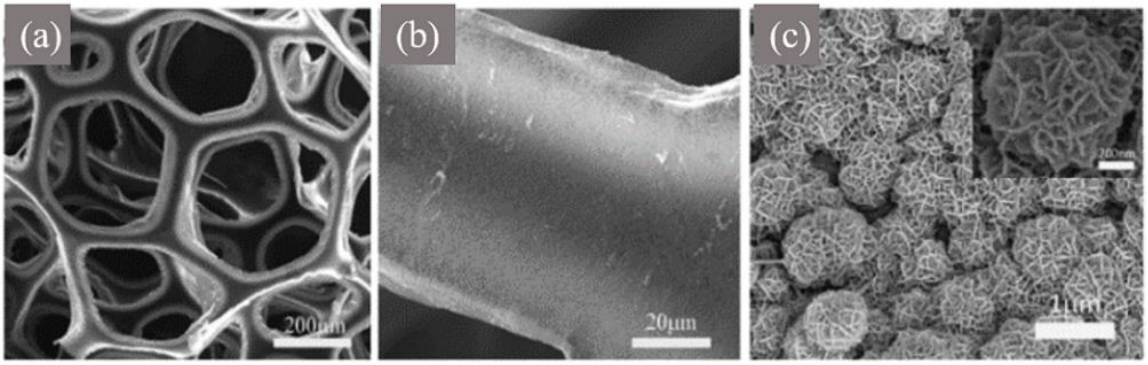

Figure 1.9. Characterizations of MnO_2-CNT-sponge. (a) An Overall View of 3D Macroporous Hierarchical MnO_2-CNT-sponge Electrode. (b) MnO_2 uniformly deposited on the skeleton of CNT-sponge; (c) high magnification of porous MnO_2 nanoparticles on CNT-sponge, inset shows an individual MnO_2 flower-like particle. Reproduced with permission from [20].

Templated methods were used to create a three-dimensional (3D) space for MO nano-architecture to coat onto.

In 2011, a scalable method was reported to fabricate MnO_2–CNT hybrid electrodes.[20] Carbon nanotubes are coated onto the sponge by a "dip-coating" method followed by galvanostatic electrochemical deposition of layered MnO_2 spheres. The high SSA (174 m^2/g) among foam materials results in a specific capacitance of 1230 F/g (based on the mass of MnO_2), the power density of 63 kW/kg and energy density of 31 Wh/kg, respectively. The outstanding cycle performance with only 2% degradation after 100,000 cycles may attribute to the delicate electrochemical deposition. The as-prepared CNT-sponge can serve as a moderate conductive substrate for depositing MO. However, the sponge takes up the limited space of the electrode and the removal process remains a problem (Figure 1.9a).

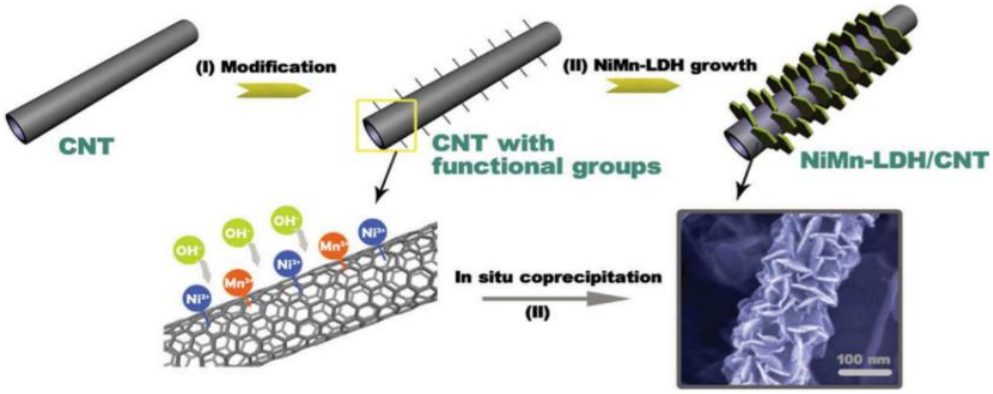

Figure 1.10. Schematic Illustration of the Synthesis and Morphology of NiMn-LDH/CNT. Step (I): the surface modification of CNT by functional groups. Step (II): the grafting of NiMn-LDH nanosheets onto CNT backbone by an in−situ growth method. High-resolution SEM image shows the detailed structure of NiMn-LDH on CNT. Reproduced with permission from [21].

Later in 2014, a hierarchical nano-architecture composed of nickel-manganese layered double hydroxide (LDH) crystals coated on CNT was developed by an in-situ room-temperature growth.[21]

The resulting material displays a porous structure with tunable Ni/Mn ratio, well-defined core-shell configuration (Figure 1.10), and enlarged surface area of 198 m^2/g. The superior capacitance of 2960 F/g (at 1.5 A/g) and energy density of 88.3 Wh/kg may attribute to the redox reactions of the hybrid MO. But the retention of 94 % after 1,000 cycles implies the low cyclic life may due to the infirm room-temperature deposition.

I.VII Carbon Nanotubes Forests (CNTF) Metal Oxide Nano-architecture

Individual CNT preserves an exceptional vertical growth mechanism facilitating the formation of a continuous network for perfect charge transport along the longitude direction. This mechanism can also form an excellent 3D nano-architecture, known as "vertically aligned CNT" or "CNT-forest", onto a silicon wafer by chemical vapor deposition (CVD) method.

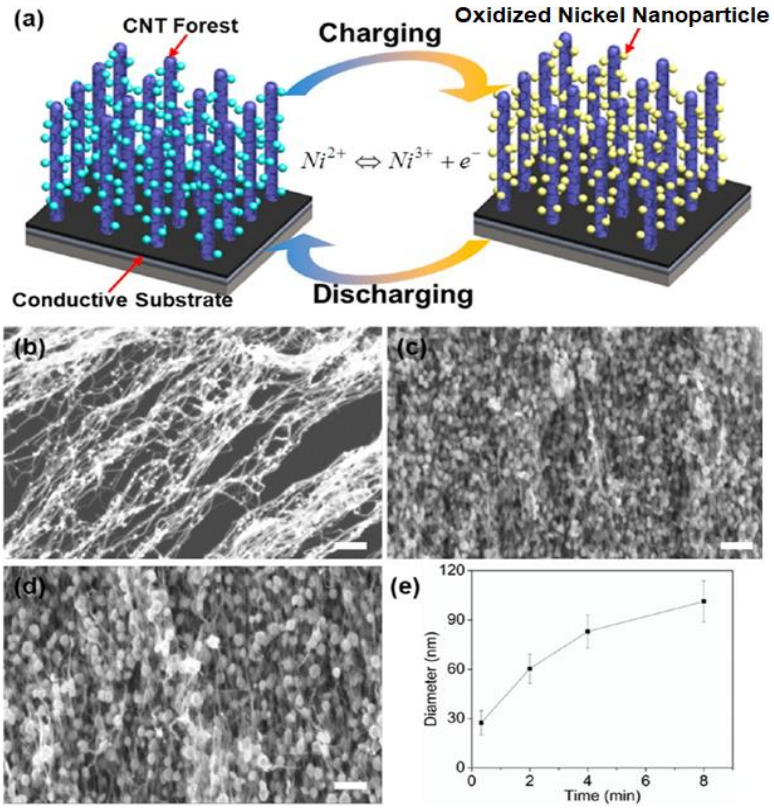

Figure 1.11. (a) Schematic of the CNTF Functionalized with NiO Nanoparticles as the Electrode. (b-d) The SEM images of the cross-sections of the NiO nanoparticle embedded the CNTF after the electrodeposition of 20 s (b), 2 min (c), and 8 min (d), respectively. The current density was 50 mA/cm^2 for all of the cases. The scale bar in b-d is 300 nm. (e) Relationship between NiO nanoparticle diameters versus deposition time. Reproduced with permission from [23].

Rather than thermal-assisted growth, electrochemical deposition has been applied to improve the morphology control of MO. Nickel nanoparticles were uniformly electrodeposited onto CNTF to improve the pseudocapacitance of the composite.[23] Electrochemical deposition offers excellent control of particle sizes (Figure 1.11e) to optimize the overall performance. Finally, the CNTF-NiO nanocomposite delivers 5.7 times higher capacitance (1.26 F/cm^3) comparing to pure CNTF and a capacitance retention of 94.2% after 10,000 cycles.

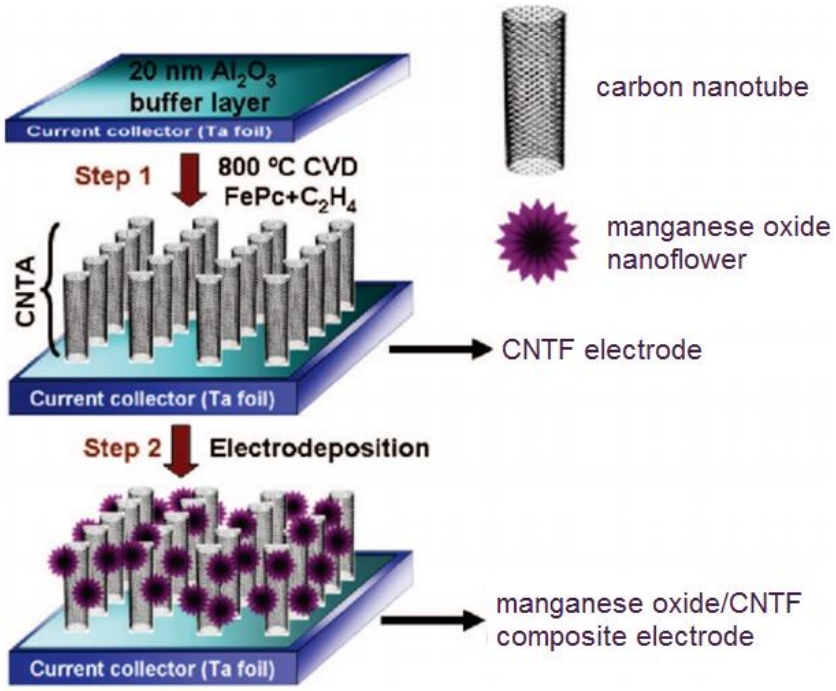

Figure 1.12. Procedure for the Preparation of Manganese Oxide/CNTF Composite Electrode. Reproduced with permission from [24].

In 2016, well-dispersed manganese oxide nanoflowers were synthesized with the combination of a CNTF framework by the electrochemical deposition (Figure 1.12).[24] The morphology and electrochemical capacitive properties of manganese oxide/CNTF composite can be simply controlled by changing the cyclic voltammetry (CV) cycle number (or current in a galvanic technique). The facial and accurate control created a good specific capacitance of 199 F/g and 305 F/cm^3, which may attribute to its dominating mesopore volume and high SSA of 234 m^2/g. Furthermore, long cycle life (3% capacity loss after 20,000 cycles) was achieved indicating the good stability of the MO nano-architecture deposited by electrochemical technique.

The as-prepared CNTF varies little in SSA value due to the exclusive synthesis method. Therefore, the MO and deposition method both play important roles in the energy storage performance of CNTF-MO composites. Dip-coating provides a simple and low-cost method for depositing MO onto CNM. However, the MO will stop growing at a certain thickness since the reactant can't access to the carbon surface. In contrast, electrochemical deposition, with controllable power output, can precisely control the morphology of the MO and easily scale up for industrial production.

I.VIII Reduced Graphene Oxide (rGO) Metal Oxide Nano-architecture

Graphene is one kind of two-dimensional (2D) carbon structures composed of the honeycomb-shaped crystal lattice. Graphene is the thinnest known material in the world

and possesses a theoretical SSA of 2620 m^2/g as well as the best mechanical and electrical properties.[25] Unlike SWNT, graphene is not soluble in water or organic solvents, which makes it difficult to handle with. Graphene oxide is obtained by treating graphite with strong oxidizers (usually by modified Hummers method), thus it contains a range of reactive oxygen groups (carbonyl (C=O), hydroxyl (-OH), phenol ($-C_6H_5$), etc.). Those functional groups grant the potential for further physical or chemical treatment, while after reduction it still maintains the excellent properties of graphene, e.g. electrical, mechanical, and thermal properties. Several studies have been done to demonstrate that rGO-MnO_2 composites are feasible materials for supercapacitors applications.

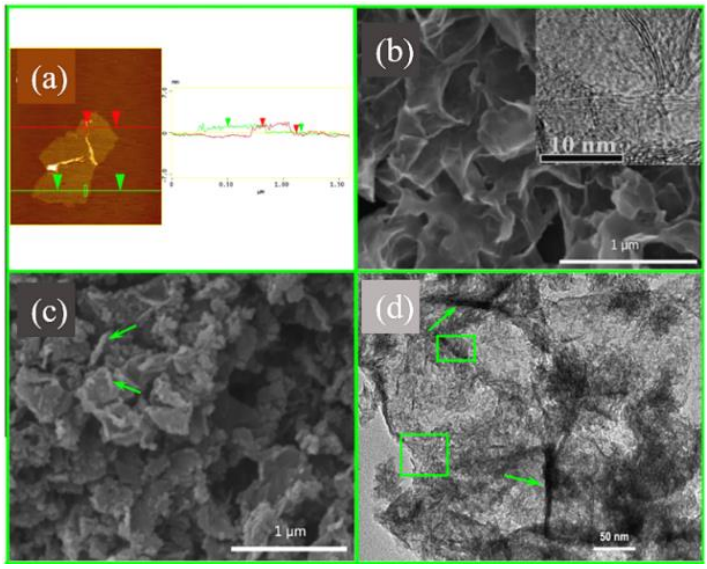

Figure 1.13. (a) AFM image of Exfoliated GO Sheets with Height Profiles. (b) SEM image of graphene (the inset shows the TEM image of graphene nanosheets with the thickness of about 2–5 nm). (c and d) Low-magnification SEM and TEM images of graphene–78 % MnO_2, showing the preferred growth of MnO_2 near the edges of graphene (marked by arrows). Reproduced with permission from [26].

In 2010, a self-limiting chemical deposition of MnO_2 on rGO sheets was reported.[26] The as-prepared composite has a specific capacitance of 310 F/g at 2 mV/s, which is almost three times higher than that of pure graphene (104 F/g). This huge increment is probably due to the growing surface of the lettuce-like MnO_2(Figure 13(b)). The SSA of graphene synthesized with such method is 267 m^2/g (far less than the theoretical value of 2600 m^2/g), which can be attributed to the agglomeration of rGO in solution-based processing.

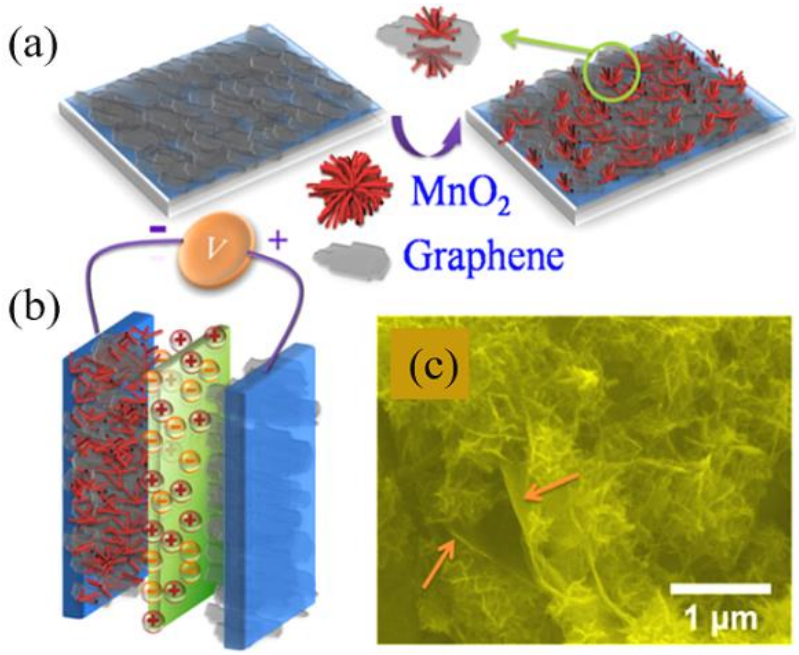

Figure 1.14. Schematics Illustrating Coating of Graphene with MnO_2 Nanoflowers. (a) Schematic of the graphene electrode and the MnO_2-coated graphene electrode. (b) Schematic of asymmetric SC with graphene as the anode and MnO_2-coated graphene as the cathode. (c) SEM image of the MnO_2-coated graphene. It also shows the graphene nanosheets which are indicated by arrows. Reproduced with permission from [27].

In another study, binderless SC electrodes were fabricated using rGO (reduced by hydrazine hydrate) and MnO_2-nanoflowers grown with electrochemical technique.[27] A high specific capacitance of 328 F/g for the MnO_2-nanoflowers coated graphene was achieved. Its energy and power density are 11.4 Wh/kg and 25.8 kW/kg with 1% decrease after 1300 charge-discharge cycles. Though the SSA of the rGO or composites were not characterized, SEM images illustrate that the MnO_2-nanoflowers obtained an increased SSA compared to the chemical deposited MnO_2 nano-architectures (Figure 1.14).

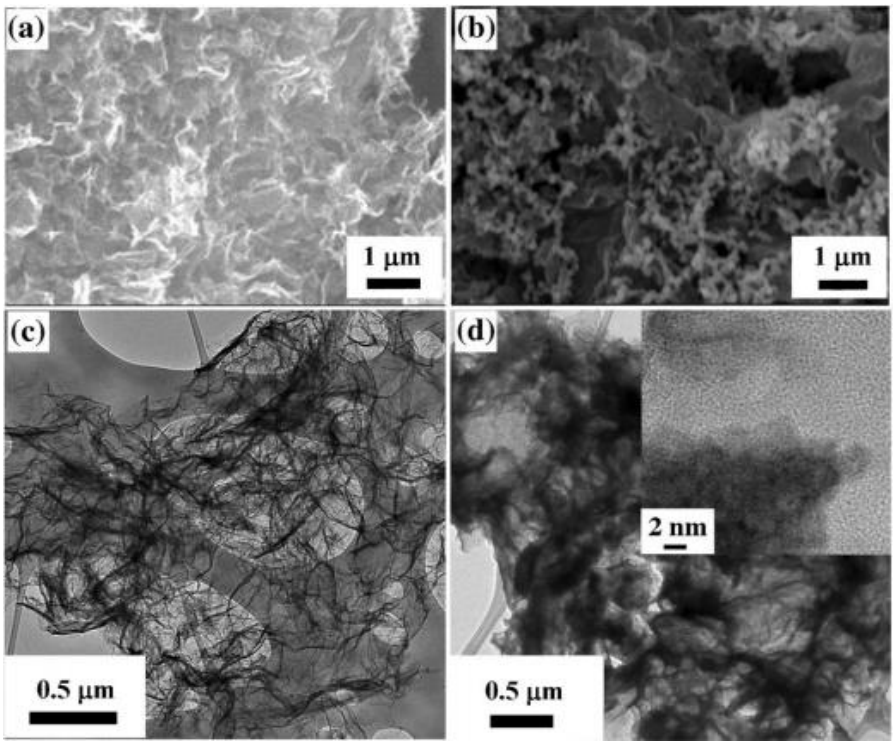

Figure 1.15. SEM Images of Graphene Aerogels (a) and MnO_2/graphene Aerogels (b) Composite. TEM images of (c) graphene aerogels and (d) MnO_2/graphene aerogels composite. Inset shows an HRTEM image for MnO_2/graphene aerogels composite. Reproduced with permission from [28].

In order to overcome the agglomeration problem of rGO, sol–gel chemical technique was deployed in synthesizing rGO-based nano-architectures. After the report of a new method of synthesis of graphene aerogels by either supercritical drying or freeze drying of hydrogel precursors,[29] a carbonaceous support (graphene aerogels) was developed in graphene-MnO_2 supercapacitors applications in 2014 (Figure 1.15).[28] Such graphene aerogels produce a wrinkled structure with SSA of 793 m^2/g and large pore sizes. A high specific capacitance of 410 F/g was achieved with 95 % retention after 50,000 cycles.

With the deployment of same CNM platform and MO active material, studies in this section indicate that the SSA is the primary parameter in the design of CNM-MO composite. Therefore, the advances of CNM synthesis and activation treatment toward high SSA is crucial in developing high-performance SC electrode.

I.IX Templated Graphene Foam (TGF) Metal Oxide Nano-architecture

Although the supercritical or freeze-drying method can relieve the agglomeration of rGO, graphene layers still partially aggregate and suffer from high inter-sheet junction contact resistance. Therefore, the synthesis of 3D TGF was developed by nickel foam-templated CVD with SSA of 850 m^2/g in 2010.[30] TGF is a good platform for depositing MO because there's no need to use binders or metal-based current collector, which dramatically decreases the total resistance as well as the total mass of the cell. Several

TGF-MO studies have been reported after that using paste-coating (nickel-aluminum double hydroxide,[31]), hydrothermal synthesis MnO_2,[32] Co_3O_4,[33] $CoMoO_4$,[34]), and electrochemical deposition ($NiCo_2O_4$[35]).

Nickel-aluminum LDH spheres have been paste-coated on TGF as a suitable electrode for pseudocapacitors.[31] In this study, a low SSA of 90.36 m^2/g was reported due to the failure to remove the nickel foam, which should have created a large amount of macro- and mesopores. This electrode material gives a specific capacitance of 1252 F/g and a capacitive retention of about 97% after 1000 cycles. The relatively high farad per gram value is probably due to the calculation is based on pristine MO only.

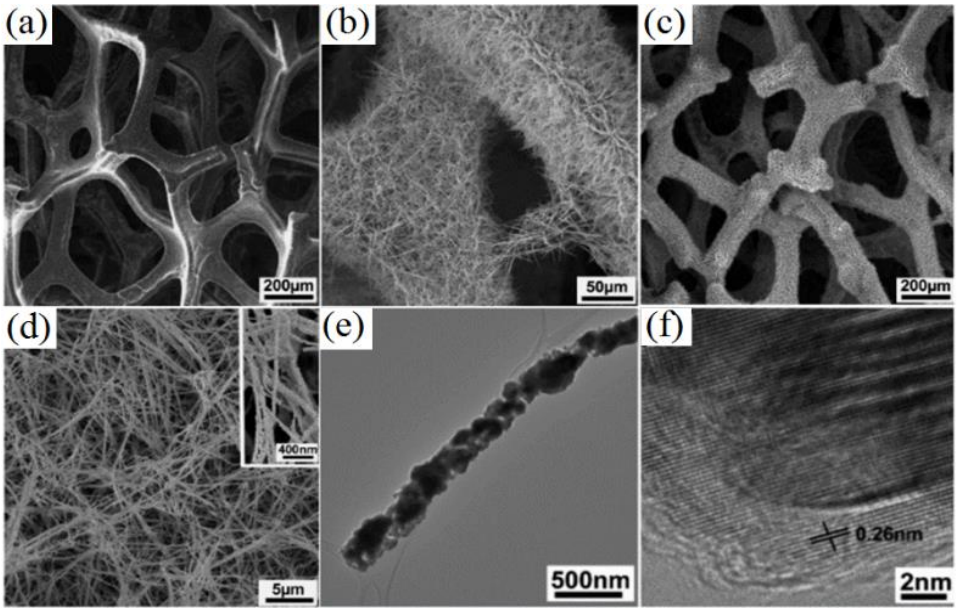

Figure 1.16. SEM Images of 3D Graphene Foam (a) and 3D Graphene/Co_3O_4 Nanowire composite (b). (c,d) Low- / high-magnification SEM images of graphene/Co_3O_4 nanowire composite. Inset panel d shows an enlarged view. (e,f) Low- and high- resolution TEM images of Co_3O_4 nanowire grown on the surface of 3D graphene foam. Reproduced with permission from [33].

Rather than nonuniform and infirm paste-coating, the hydrothermal method provides firm growth of the TGF-MO framework (Figure 1.16). 3D TGF-MnO_2 and TGF-Co_3O_4 hybrid electrodes were reported with the hydrothermal synthesis with $KMnO_4$ and $CoCl_2 \cdot 6H_2O$ as precursors by the same research group. The as-prepared flower-like MnO_2 and nanowire Co_3O_4 architecture offer specific capacitances of 560 F/g and 1100 F/g, respectively. The retention of TGF-MnO_2 is 79 % after 1000 cycles, while TGF-Co_3O_4 shows a stable performance after 500 cycles. TGF-MnO_2 has lower capacity, but the morphology of the MnO_2 nanostructures can be readily controlled by the solution acidity.

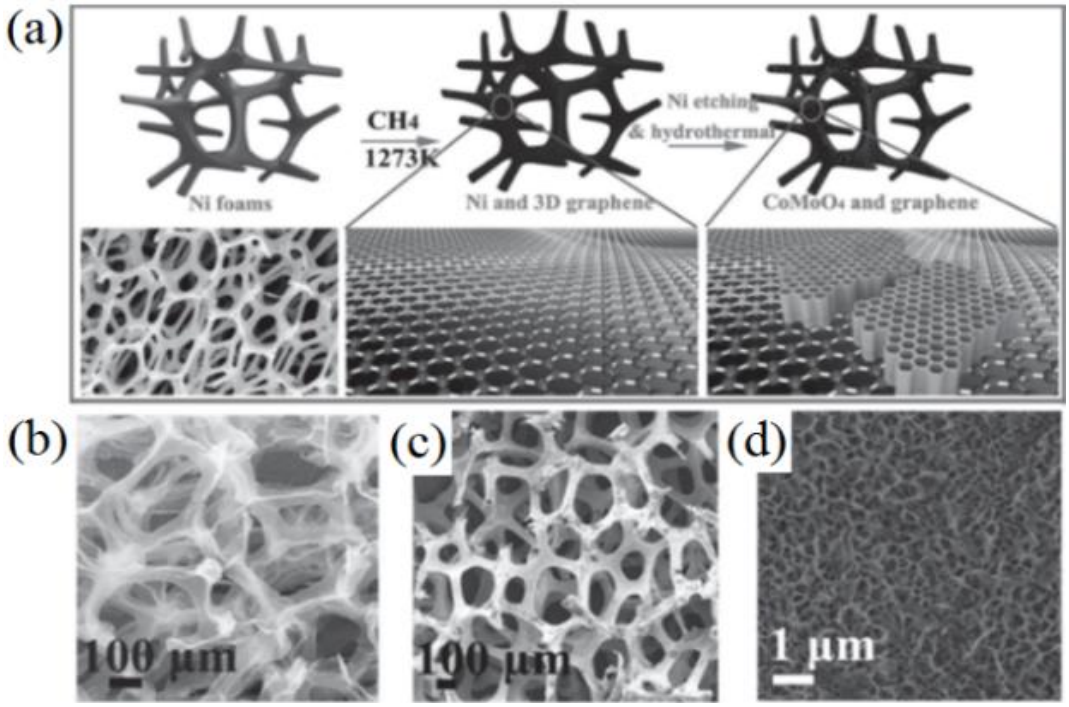

Figure 1.17. Growth Mechanism and the Morphology of $CoMoO_4$–3D Graphene Hybrid Electrodes. (a) the Typical Synthesis Procedure of the Graphene Hybrid Electrodes, (b) SEM images of 3D graphene, (c-d) honeycomb-like strongly coupled $CoMoO_4$–3D graphene hybrid at various magnifications. Reproduced with permission from [34].

Superior to single-phase MO, hybrid MO may have synergistic effects which can enhance the electrical/ionic conductivity, electrochemical reactivity, and mechanical stability of each component.[36] Furthermore, it can offer fast and effective surface intercalation/electrosorption by decreasing the surface energy of the active nanomaterials.[37] In 2013, a cost-effective strategy for the growth of novel honeycomb-like $CoMoO_4$ strongly coupled on 3D TGF was presented (Figure 1.17).[34] The nanohoneycomb-like strongly coupled TGF-$CoMoO_4$ illustrates an ultra-high pseudocapacitive performance from 1101 F/g to 2741 F/g at current densities from 85.71 to 1.43 A/g. It also exhibits an excellent cyclic stability (96.36% retention after 100,000 cycles).

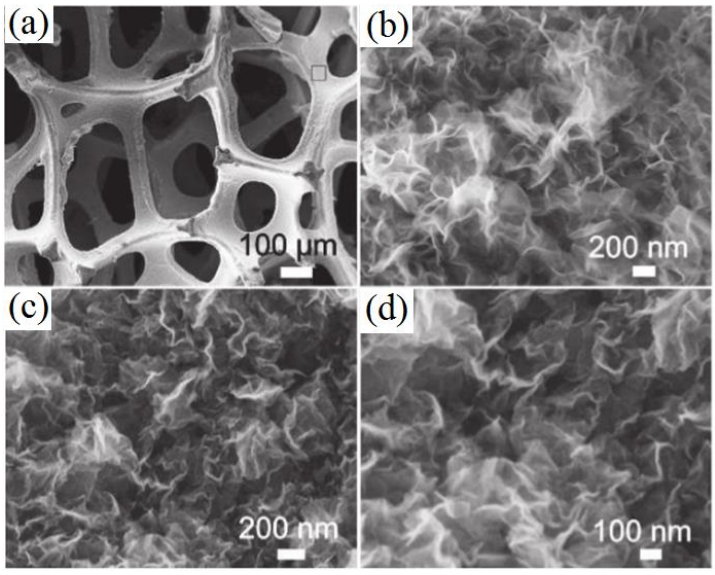

Figure 1.18. FESEM Images of Ni Foam Covered by the Bimetallic (Ni, Co) Hydroxide Precursor (a,b) and the Derived $NiCo_2O_4$ Ultra-thin Nanosheets/Ni Foam (c,d). Image in (b) is taken from the region marked with a rectangle in (a). Reproduced with permission from [35].

Electrochemical deposition has also been applied in hybrid MO system, ultrathin mesoporous $NiCo_2O_4$ nano-sheets were grown on Ni foam with strong adhesion for supercapacitors applications (Figure 1.18).[35] The as-obtained $NiCo_2O_4$ nano-sheets possess an ultrahigh specific capacitance of 2010 and 1450 F/g at current densities of 2 and 20 A/g, respectively, and able to retain 94 % of its initial capacitance after 2400 cycles. Generally, TGF is an ideal structure for depositing MO to realize high pseudocapacitance. However, the supercapacitors applications of TGF are limited because the CVD synthesis requires additional cost and time, and produces relatively low SSA.

I.X Electrospun Carbon Nanofiber (ECNF) Metal Oxide Nano-architecture

ECNF is well known for its large porosity, high conductivity, cheap and freestanding nature as electrode materials for supercapacitors applications and commercial production.[38, 39] Moreover, ECNF structures can also be served as scaffolds to uniformly support MO nano-architecture because of their reliable 3D-network structure significantly enhancing the rate capability by shortening the distance of electron transport. Therefore, huge amount of studies have been done focusing on ECNF-MO synthesis via co-electrospinning, dip-coating and electrochemical deposition[40].

Activated ECNF has been coupled with SnO_2[41] and Co_3O_4[42] by incorporating MO precursors (e.g. $SnCl_2 \cdot 2H_2O$, cobalt(II) acetylacetonate ($Co(acac)_2$)) into polyacrylonitrile (PAN) via a one-step co-electrospinning method. Activated porous

ECNF-SnO_2 electrode has been synthesized using this method with an enhanced SSA of 1082.1 m^2/g, total pore volumes of 0.64 cm^3/g, and volume percentages of mesoporous (35.0%) compared with conventional ECNF (Figure 1.19). The capacitive tests indicate a specific capacitance of 289.0 F/g, power density ranging from 80–8000 W/kg at 0.2-20 A/g current density, and energy density around 14.4–7.7 Wh/kg.

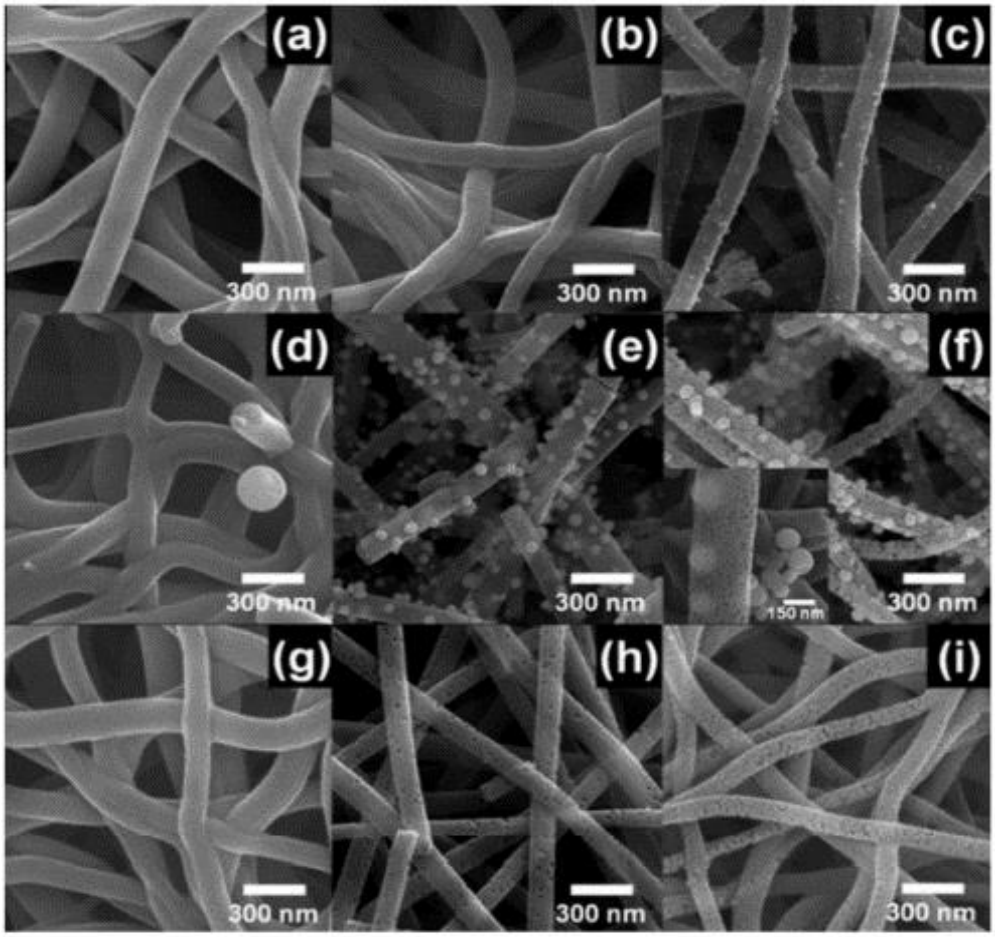

Figure. 1.19 FESEM Images of Samples Obtained After Carbonization at 800 °C Under N_2 Atmosphere (a–c). after H_2-reduction (d–f), and after acid treatment (g–i). Reproduced with permission from [41].

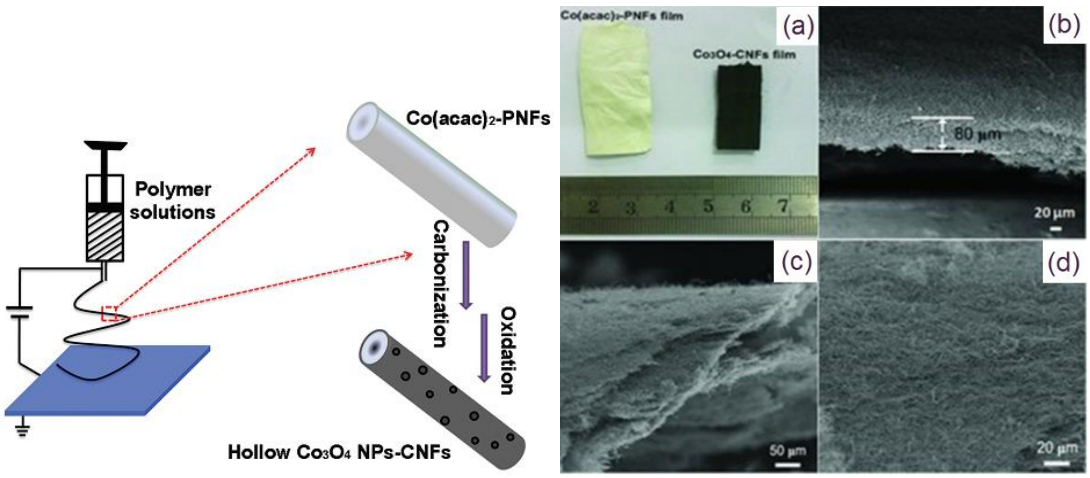

Figure 1.20. Left Panel: Ideal Schematic Illustration for Obtaining Porous ECNF Electrodes Synthesized Using Co-electrospinning Method with H_2-reduction and Post Annealing Strategy. Right panel: (a) the photograph of $Co(acac)_2$-PNFs and Co_3O_4-ECNF hybrid films. (b,c) The side-view SEM images and (d) the top-view SEM image of the Co_3O_4-ECNF hybrid films. Reproduced with permission from [42].

Similarly, activated ECNF-Co_3O_4 composites show a relatively high specific capacitance of 556 F/g with an excellent cyclic performance of 2000 cycles with a negligible specific capacitance decay of about 1%.[42] The advantage of this method is the facial synthesis/processes and ultrahigh surface area (>1000 m^2/g) compared to non-activated ECNF (<100 m^2/g). The activation treatment increases the SSA but undermines the internal structure of the ECNF network (Figure 1.20), therefore its potential applications in stretchable devices will be limited.

Carbon fiber paper (CFP), also known as carbon fabric or carbon cloth, is a commercial product physically similar to ECNF. $NiCo_2O_4$ is the most popular metal oxide material coupled with CFP in the forms of $NiCo_2O_4$ nanosheet arrays,[43] CFP-$NiCo_2O_4$-NiO,[44] CFP-NiCo LDH[45] and CFP-Ni/Co LDH-ZnO.[46] $NiCo_2O_4$ precursor was electrodeposited onto CFP to form ultrathin (10 nm) nanosheet arrays. The interconnected structure with a good conductivity of the composites delivered an astonishing high specific capacitance of 2658 F/g with retention of 80% after 3000 cycles.[43]

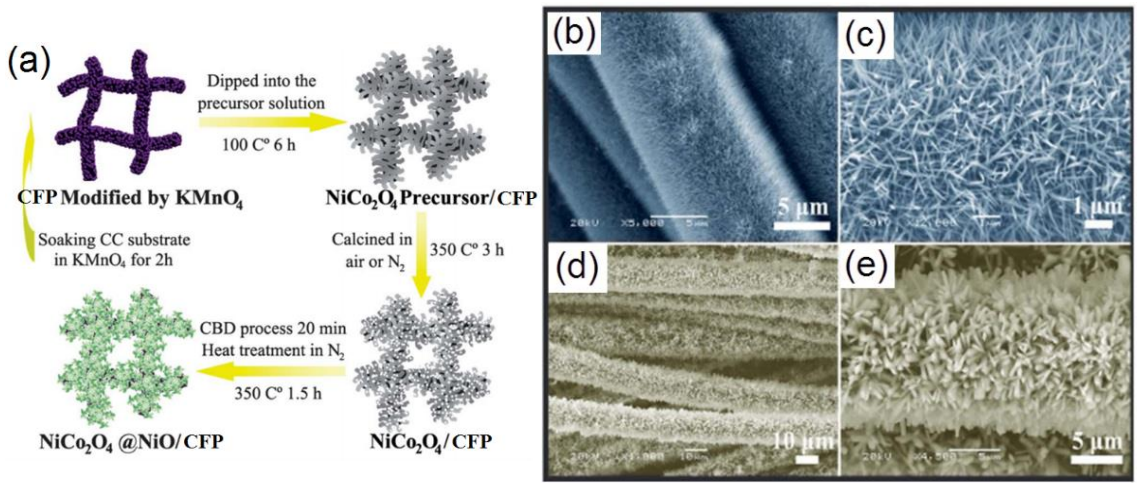

Figure 1.21. (a) Schematic Illustration of the Growth Process of Porous $NiCo_2O_4$ Nanowires on Carbon Cloth and Subsequent Chemical Bath to Deposit NiO Nanoflakes on $NiCo_2O_4$/CFP. To prepare the $NiCo_2O_4$@NiO/CFP composite, $NiCo_2O_4$@NiO/CFP composite and $NiCo_2O_4$/CC samples prepared by annealing their precursor in nitrogen ($NiCo_2O_4$/CFP-N_2) and in air ($NiCo_2O_4$/CFP-Air) respectively; SEM images of sample $NiCo_2O_4$/CFP-N_2 (b and c) and $NiCo_2O_4$/CFP-Air (d and e) at different magnifications. Reproduced with permission from [44].

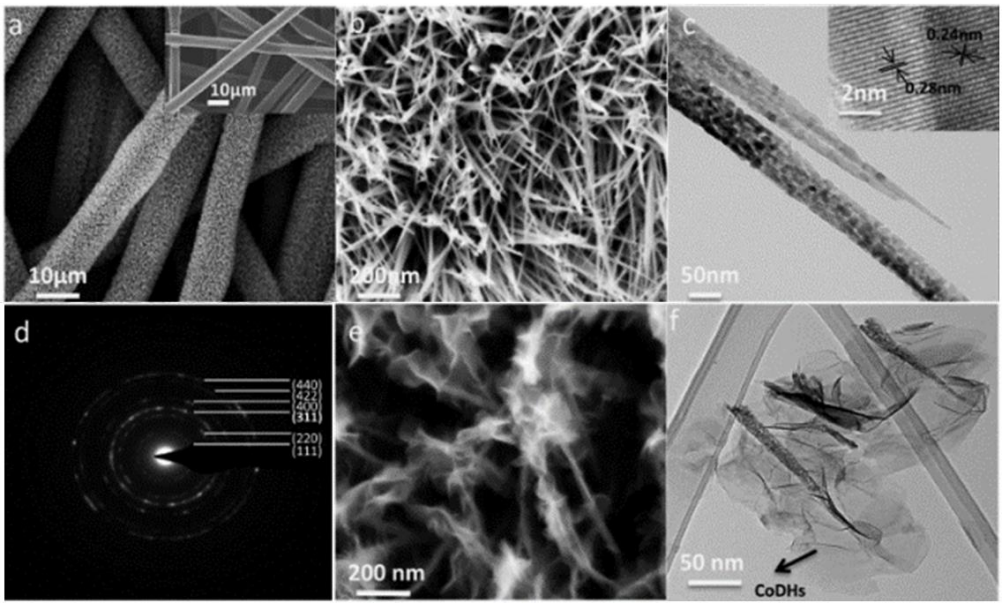

Figure 1.22. (a) SEM Image of CFP Before (inset) and After Growth of $NiCo_2O_4$ Nanowires. (b) High-magnification SEM image of $NiCo_2O_4$ nanowires grown on CFP. (c) TEM image and HRTEM image (inset) of 2 $NiCo_2O_4$ nanowires. (d) Diffraction pattern of a $NiCo_2O_4$ nanowire. (e) SEM image of a CoxNi1−x hydroxide coating on $NiCo_2O_4$ nanowire grown on CFP. (f) TEM image of CoDHs/ $NiCo_2O_4$ nanowires grown on CFP. Reproduced with permission from [45].

$NiCo_2O_4$-NiO core–shell hetero-nanowire on CFP (Figure 23) has been assembled by dip-coating for a high-performance flexible all-solid-state SC (Figure 1.21),[44] while Co_xNi_{1-x} hydroxide was electrodeposited onto CFP to form CFP-$NiCo_2O_4$ nanowire arrays (Figure 1.22).[45] Both of the designs have shown extraordinary performance in captivity, stability, and simplicity. Their high specific capacitances (1500-1800 F/g), energy density (33-42 Wh/kg) and power density (41-42 kW/kg) can be attributed to the unique 3D micrometer architecture of the CFP-Ni/Co-MO hybrid structures.

CNTF, TGF and ECNF are ideal for depositing MO since they optimize all CNM's characterizations to provide a conductive and mechanical 3D network. These structures can dramatically decrease the total resistance as well as the mass of the cell because there's no need to deploy binder or metal-based current collector. ECNF stands out due to its facial and scalable synthesis, thus it has good potential for the development of light, compact, and high-performance supercapacitors.

I.XI CNM Hybrid Nano-architecture

CNT, rGO, TGF and ECNF are the most promising carbon nano-architecture materials for energy storage applications. Each of them has some superior properties, e.g. physical, morphological. Therefore, the structures that bundle multiple CNM together as hybrid materials are very attractive since they may hold their intrinsic properties and grant new characteristics prior to single CNM.

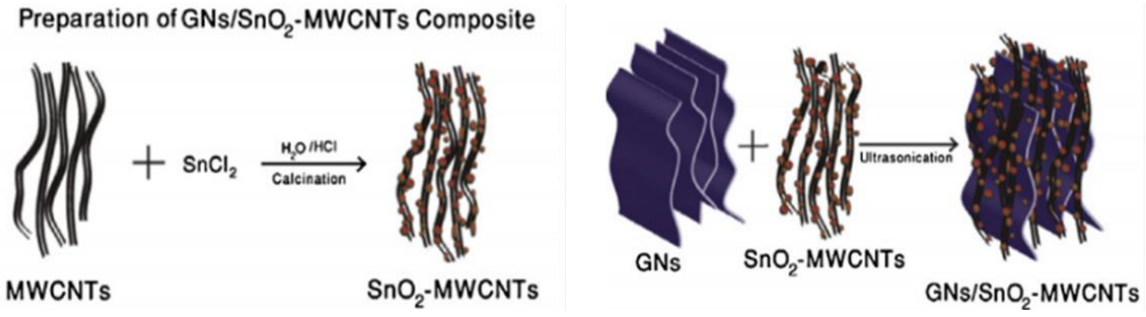

Figure 1.23. Schematic of Preparation of Supercapacitor Electrode Material. Reproduced with permission from [47].

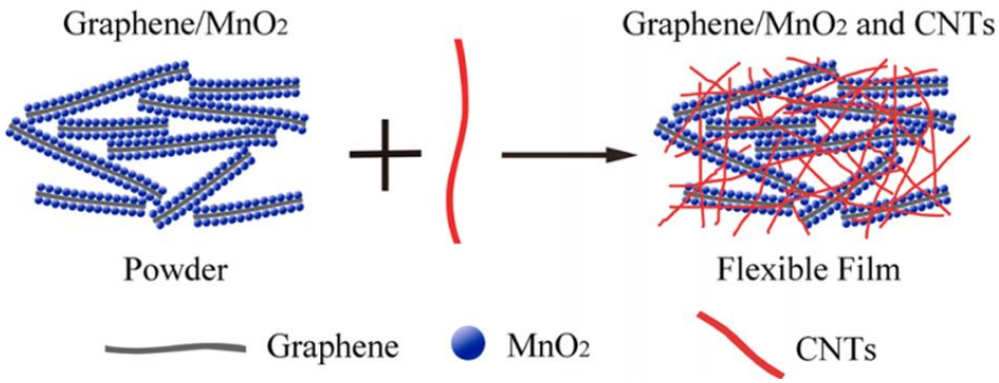

Figure 1.24. Schematic Illustration of the Fabricated Flexible and Conductive Film Using Graphene/MnO_2/CNT. Note the difference in the possible electron paths for the two architectures: electron has to pass the insulating MnO_2 layers for the graphene/MnO_2 composite. Reproduced with permission from [48].

Two hybrid syntheses of rGO-CNT electrode coupled with SnO_2 (Figure 1.23)[47] and MnO_2 (Figure 1.24)[48] were developed for supercapacitors applications. Their specific capacitance of 224 F/g and 372 F/g were obtained for SnO_2 and MnO_2, respectively. The difference is SnO_2 was firstly deposited onto CNT via calcination method at 350 °C then intercalated with rGO, while MnO_2 was chemically deposited onto rGO via coprecipitation method then CNT added as a conductive network. Their competing energy, power density, and cycle life were 31 Wh/kg versus 2.2 Wh/kg, 17.6 kW/kg versus. 42 kW/kg, and 81% ~ 6000 versus. 5% ~ 1000, respectively. The different coupling orders (CNT-rGO versus rGO-CNT) offer very close electrochemical performances except for the higher capacitance of MnO_2.

Rather than CNT and rGO, CNTF and TGF can offer excellent conductive network without agglomeration, thus they were combined then coupled with various MO for high-performance supercapacitors. TGF-CNTF with Fe_2O_3[49] and MnO_2[50] were developed as novel 3D hierarchical nano-architectures.

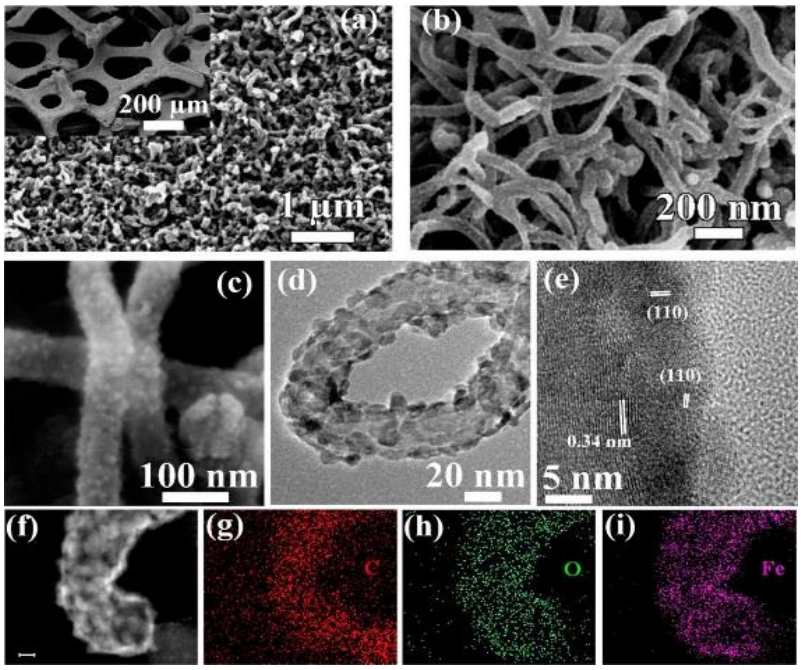

Figure 1.25. (a-c) SEM and (d-e) HRTEM Images of TGF-CNT@Fe_2O_3. (f) high-angle annular dark-field STEM image of a single CNT@Fe_2O_3 and (g-i) the corresponding STEM element mapping. The scale bar in (f) is 10 nm. Reproduced with permission from [49].

Atomic layer deposition (ALD) is an advanced deposition method which can produce thin, conformal films with control of the thickness and composition at an atomic level. A novel TGF-CNTF hybrid structure was firstly synthesized by growing CNT on the nickel-foam templated graphene 3D scaffold.[49] Then ALD has been utilized to deposit Fe_2O_3 on the TGF-CNTF for energy storage tests.[49] A record-breaking specific

capacitance of 2555.6 F/g was achieved plus the full-cell charge-discharge based test gave a high energy of 74.7 Wh/kg at the power density of 1400 W/kg. The combination of TGF and CNTF maximizes the conductivity and porosity of the composite (Figure 1.25), and the advanced ALD deposition leads to a superior cyclic performance of 95.4% retention after 50,000 cycles. The top-level specific capacitance may attribute to the relatively small mass loading of Fe_2O_3, which is lowered to 210 F/g when the whole electrode mass was considered.

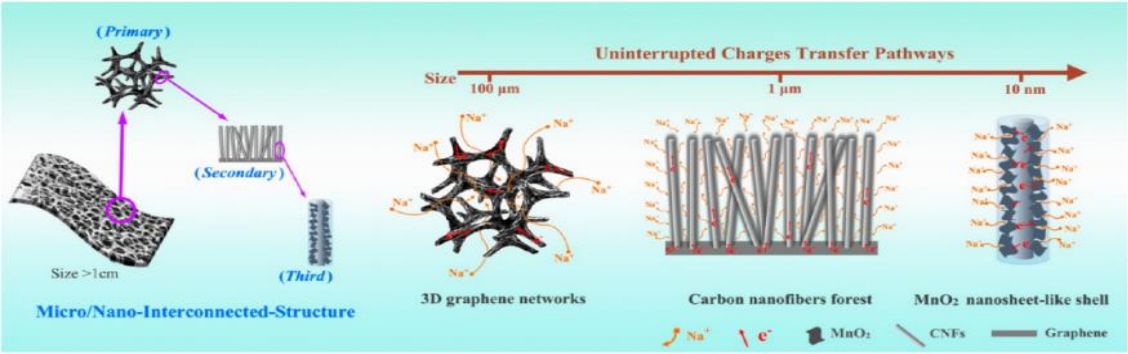

Figure 1.26. Schematic Illustration of 3D Micro/nano-interconnected Structure as Flexible SC Electrode. The designed 3D micro/nano-interconnected structure is based on the bulk hierarchical graphene/ECNF/MnO2 composite (with the dimension >1 cm), where primary structure (with a dimension of 100 μm) is made by the graphene networks, secondary structure (with a dimension of 1 μm) is made by the CVD grown-CNTF on graphene skeletons, and tertiary structure (with a dimension of 10 nm) is made by a hemicylindrical MnO2 nanosheet-like shell. Moreover, this 3D micro/nano-interconnected structure can provide uninterrupted charges transfer pathways in storage reaction. Reproduced with permission from [51].

Similarly, a synthesis of TGF-CNTF on nickel foam followed with dip-coating to deposit MnO_2 onto the hybrid structure was reported with a high specific capacitance of

948 F/g (Figure 1.26).[51] The as-prepared electrode delivers an energy density of 53.4 Wh/kg, a power density of 332.5 W/kg, and a retention of 94.1 % after 1000 cycles. The dip-coating method usually provides a higher mass loading than ALD, thus the specific capacitance based on whole electrode mass may be higher compared to ALD. However, the less stable binding between the TGF-CNTF and MnO_2 may undermine the retention performance.

I.XII Summary

As summarized from the results and discussions in this chapter, CNM such as CNT, rGO and CO/CS, intrinsically has large surface area, controllable PSD and excellent conductivity for EDLC applications. CNM nano-architecture may replace the current industrial supercapacitors materials with higher energy and power density. However, the increased energy density of CNM compare to activated carbon is still limited and the high cost of the synthesis is the bottleneck. CNM-based structures, such as CNTF, TGF, ECNF/CFP, possess extensive options of chemical modification and optimal mechanical property, which are used as substrates to stabilize active MO layers, e.g. by integrating pseudocapacitance with EDLC. Among these candidates, CNTF possesses the most uniform morphology with ballistic electron transport along the vertical direction, which provides the best interface-to-conductor conductivity, but the small gap between CNTF may block the electrolyte infiltration after deposited with MO. TGF has interconnected

foam-like structure with the best electric conductivity and mechanical strength of a 3D framework, but its pore size is limited by the foam template which is large (usually hundreds of micrometers). Furthermore, both of them utilize hash synthesis conditions which are costly. Therefore, ECNF/CFP stands out for its competitive properties, scalable and facial synthesis. However, the challenges remain on how to order the orientation of the fibers and prevent the active coating from deformation/degradation. The desirable deposition method for MO or post-treatment of the CNM-MO is one of the key factors for high energy storage performance. Thermal-chemical reaction, dip-coating, and paste-coating use the simplest apparatus with control of the coating time. They offer MO loose and porous nano-architectures from moderate to good, but the immobility of the MO is poor. Hydrothermal method offers homogeneous MO morphology with control of the temperature and the concentration of the solution, but the crystals typically have high density with no porosity which lowers the SSA of MO architecture. Same as hydrothermal, microwave-assisted synthesis is taken in an autoclave reactor but with different nucleation mechanism. Thus the later is better in controlling the morphology of MO with porous nano-architecture with higher SSA. ALD demonstrates its outstanding capacitance and high stability with the most accurate control of MO thickness, however, the mass loading is low and the cost is high. Electrochemical deposition is a facial and applicable method which provides relatively firm deposition with high SSA and low cost. Vast opportunities remain for developing nano-architecture electrodes by electrochemical deposition with

performances from great to superior. Based on the discussion above, the combination of ECNF and electrochemical deposition is a promising route towards the next generation supercapacitors. Though many exciting results have been reported, they are not representing the overall performance since the mass ratio of MnO_2/cell are very small. Research have been done to increase the whole cell performance by loading large amount of MnO_2 onto the electrode.[7-9] These studies offered solutions toward commercial level mass loading but also indicating that the accumulation of MnO_2 will suffer from high electronic resistance which can lower their galvanic charge-discharge efficiency.[10, 11]

In this thesis, the crucial factors including deposition time, specific capacitance, etc. of ECNF/metal oxide hybrid electrodes synthesized via dip-coating will be discussed. The electrochemical growth processes of MnO_2 on super-aligned ECNF (SA-ECNF) will be reported with respect to mass loading, energy density and retention life. The energy storage ability enhancement of MnO_2 regards magnetic properties will be studied. Moreover, a unique self-sustainable separator-free configuration of a MnO_2-SA-ECNF electrodes which is capable of providing good energy storage performance while saving the space of a separator will be presented.

I. XIII References

[1] M. Winter, R.J. Brodd, Chemical reviews, 104 (2004) 4245-4270.

[2] B. Conway, W. Pell, Journal of Solid State Electrochemistry, 7 (2003) 637-644.

[3] R. Ma, J. Liang, B. Wei, B. Zhang, C. Xu, D. Wu, Journal of Power Sources, 84 (1999) 126-129.

[4] M.Winter, R. J. Brodd, Chemical reviews, 104 (2004) 4245-4270.

[5] D. Pech, M. Brunet, H. Durou, P. Huang, V. Mochalin, Y. Gogotsi, P.-L. Taberna, P. Simon, Nature nanotechnology, 5 (2010) 651-654.

[6] H.-J. Liu, W.-J. Cui, L.-H. Jin, C.-X. Wang, Y.-Y. Xia, Journal of Materials Chemistry, 19 (2009) 3661-3667.

[7] D.N. Futaba, K. Hata, T. Yamada, T. Hiraoka, Y. Hayamizu, Y. Kakudate, O. Tanaike, H. Hatori, M. Yumura, S. Iijima, Nature materials, 5 (2006) 987-994.

[8] C. Kim, K. Yang, Applied physics letters, 83 (2003) 1216-1218.

[9] Y. Zhu, S. Murali, M.D. Stoller, K. Ganesh, W. Cai, P.J. Ferreira, A. Pirkle, R.M. Wallace, K.A. Cychosz, M. Thommes, Science, 332 (2011) 1537-1541.

[10] D.P. Harrop, D. H. Zervos, in, IDTechEx report, 2010.

[11] J. Chmiola, G. Yushin, R. Dash, Y. Gogotsi, Journal of Power Sources, 158 (2006) 765-772.

[12] T. Hiraoka, A. Izadi‐Najafabadi, T. Yamada, D.N. Futaba, S. Yasuda, O. Tanaike, H. Hatori, M. Yumura, S. Iijima, K. Hata, Advanced Functional Materials, 20 (2010) 422-428.

[13] K. Kierzek, E. Frackowiak, G. Lota, G. Gryglewicz, J. Machnikowski, Electrochimica Acta, 49 (2004) 515-523.

[14] Y. Wu, T. Zhang, F. Zhang, Y. Wang, Y. Ma, Y. Huang, Y. Liu, Y. Chen, Nano Energy, 1 (2012) 820-827.

[15] L. Zhang, X. Yang, F. Zhang, G. Long, T. Zhang, K. Leng, Y. Zhang, Y. Huang, Y. Ma, M. Zhang, Journal of the American Chemical Society, 135 (2013) 5921-5929.

[16] M. Noked, E. Avraham, A. Soffer, D. Aurbach, The Journal of Physical Chemistry C, 113 (2009) 21319-21327.

[17] X. Zheng, J. Luo, W. Lv, D.W. Wang, Q.H. Yang, Advanced Materials, 27 (2015) 5388-5395.

[18] M. Terrones, Annual review of materials research, 33 (2003) 419-501.

[19] Z. Chen, V. Augustyn, J. Wen, Y. Zhang, M. Shen, B. Dunn, Y. Lu, Advanced materials, 23 (2011) 791-795.

[20] W. Chen, R. Rakhi, L. Hu, X. Xie, Y. Cui, H.N. Alshareef, Nano letters, 11 (2011) 5165-5172.

[21] J. Zhao, J. Chen, S. Xu, M. Shao, Q. Zhang, F. Wei, J. Ma, M. Wei, D.G. Evans, X. Duan, Advanced Functional Materials, 24 (2014) 2938-2946.

[22] M. Mazloumi, S. Shadmehr, Y. Rangom, L.F. Nazar, X. Tang, ACS nano, 7 (2013) 4281-4288.

[23] Y. Jiang, P. Wang, X. Zang, Y. Yang, A. Kozinda, L. Lin, Nano letters, 13 (2013) 3524-3530.

[24] H. Zhang, G. Cao, Z. Wang, Y. Yang, Z. Shi, Z. Gu, Nano letters, 8 (2008) 2664-2668.

[25] A.K. Geim, science, 324 (2009) 1530-1534.

[26] J. Yan, Z. Fan, T. Wei, W. Qian, M. Zhang, F. Wei, Carbon, 48 (2010) 3825-3833.

[27] Q. Cheng, J. Tang, J. Ma, H. Zhang, N. Shinya, L.-C. Qin, Carbon, 49 (2011) 2917-2925.

[28] C.C. Wang, H.C. Chen, S.Y. Lu, Chemistry–A European Journal, 20 (2014) 517-523.

[29] X. Zhang, Z. Sui, B. Xu, S. Yue, Y. Luo, W. Zhan, B. Liu, journal of materials chemistry, 21 (2011) 6494-6497.

[30] Z. Chen, W. Ren, L. Gao, B. Liu, S. Pei, H.-M. Cheng, Nature materials, 10 (2011) 424-428.

[31] D. Momodu, A. Bello, J. Dangbegnon, F. Barzeger, F. Taghizadeh, M. Fabiane, A.C. Johnson, N. Manyala, AIP Advances, 4 (2014) 097122.

[32] X. Dong, X. Wang, J. Wang, H. Song, X. Li, L. Wang, M.B. Chan-Park, C.M. Li, P. Chen, Carbon, 50 (2012) 4865-4870.

[33] X.-C. Dong, H. Xu, X.-W. Wang, Y.-X. Huang, M.B. Chan-Park, H. Zhang, L.-H. Wang, W. Huang, P. Chen, ACS nano, 6 (2012) 3206-3213.

[34] X. Yu, B. Lu, Z. Xu, Advanced Materials, 26 (2014) 1044-1051.

[35] C. Yuan, J. Li, L. Hou, X. Zhang, L. Shen, X.W.D. Lou, Advanced Functional Materials, 22 (2012) 4592-4597.

[36] Y. Wang, Y. Wang, E. Hosono, K. Wang, H. Zhou, Angewandte Chemie International Edition, 47 (2008) 7461-7465.

[37] T. Fang, J.-G. Duh, S.-R. Sheen, Journal of the Electrochemical Society, 152 (2005) A1701-A1706.

[38] H. Hou, D.H. Reneker, Advanced Materials, 16 (2004) 69-73.

[39] S. Ramakrishna, K. Fujihara, W.-E. Teo, T. Yong, Z. Ma, R. Ramaseshan, Materials today, 9 (2006) 40-50.

[40] J. Miao, M. Miyauchi, T.J. Simmons, J.S. Dordick, R.J. Linhardt, Journal of nanoscience and nanotechnology, 10 (2010) 5507-5519.

[41] G.-H. An, H.-J. Ahn, Carbon, 65 (2013) 87-96.

[42] F. Zhang, C. Yuan, J. Zhu, J. Wang, X. Zhang, X.W.D. Lou, Advanced Functional Materials, 23 (2013) 3909-3915.

[43] J. Du, G. Zhou, H. Zhang, C. Cheng, J. Ma, W. Wei, L. Chen, T. Wang, ACS applied materials & interfaces, 5 (2013) 7405-7409.

[44] W. Yang, Z. Gao, J. Ma, X. Zhang, J. Wang, J. Liu, Journal of Materials Chemistry A, 2 (2014) 1448-1457.

[45] L. Huang, D. Chen, Y. Ding, S. Feng, Z.L. Wang, M. Liu, Nano letters, 13 (2013) 3135-3139.

[46] I. Shakir, M. Shahid, U.A. Rana, I.M. Al Nashef, R. Hussain, Electrochimica Acta, 129 (2014) 28-32.

[47] R. Rakhi, H.N. Alshareef, Journal of Power Sources, 196 (2011) 8858-8865.

[48] Y. Cheng, S. Lu, H. Zhang, C.V. Varanasi, J. Liu, Nano letters, 12 (2012) 4206-4211.

[49] C. Guan, J. Liu, Y. Wang, L. Mao, Z. Fan, Z. Shen, H. Zhang, J. Wang, ACS nano, 9 (2015) 5198-5207.

[50] W. Wang, S. Guo, I. Lee, K. Ahmed, J. Zhong, Z. Favors, F. Zaera, M. Ozkan, C.S. Ozkan, Scientific reports, 4 (2014).

[51] Y. He, W. Chen, J. Zhou, X. Li, P. Tang, Z. Zhang, J. Fu, E. Xie, ACS applied materials & interfaces, 6 (2013) 210-218.

CHAPTER II

STABLE LOW-CURRENT ELECTRODEPOSITION OF α-MnO_2 ON SUPER-ALIGNED ELECTROSPUN CARBON NANOFIBERS FOR HIGH-PERFORMANCE ENERGY STORAGE

This chapter has been published as: **Liu, Y.**, Zeng, Z., Bloom, B., Waldeck, D. H., Wei, J. Stable Low-Current Electrodeposition of α-MnO_2 on Superaligned Electrospun Carbon Nanofibers for High-Performance Energy Storage. *Small*, **2017**, 1703237.

II.I Introduction

Manganese dioxide (MnO_2) has been demonstrated to be one of the most promising electrode materials for lithium batteries and pseudocapacitors/ supercapacitors, with a theoretical specific capacitance of 1370 F/g,[1] ecofriendly, magneto property,[2] and abundant earth reserves.[3] However, MnO_2 electrodes often suffer from low proton diffusion constant ($\sim 10^{-13}$ $cm^2/(V\ s)$) and low electrical conductivity ($\sim 10^{-5}$ S/cm) which can lower their galvanic charge-discharge capacity.[4, 5] In contrast, carbon-based nanomaterials, e.g. carbon nanotubes (CNT), graphene,[6] and carbon nanofibers (CNF), can display high electrical conductivity, high charge transfer capability, large specific surface area mesoporosity, and high electrolyte accessibility.[7] In the past decade, a series of carbon nanomaterials (CNT,[8-12] CNT-forest (CNTF),[13] reduced graphene

voxide,[14-16] templated graphene foam (TGF),[17-19] CNF[20]) have been coupled with MnO_2 to lower their electrical resistance while retaining high charge capacity.

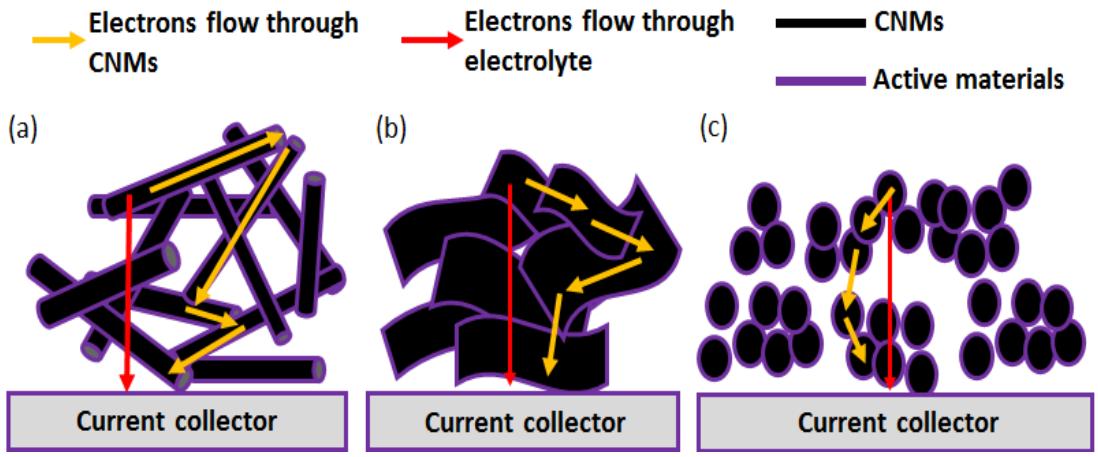

Figure 2.1. Schematic Illustration of the Electrons Flow Through Different Carbon Nanomaterials (CNMs). (a) CNT, (b) graphene/rGO, and (c) carbon spheres/onions coupled with active materials (MnO_2 in this case) to the current collector. Yellow and red arrows indicate the electron flow through CNMs and electrolyte, respectively.

Figure 2.1 illustrates the scheme of electrons flow in a typical "CNMs-active material" platform. Since these CNMs usually are individual particles or flakes, the active materials deposited on their surfaces will largely increase the resistance when electrons flow between CNMs particles or flakes which lead to an electron transfer route similar to typical batteries (entirely through electrolyte) with decreased power density and lifetime. In contrast, CNTF and CNF have shown great potential in building CNMs-active materials hybrid electrodes for energy storage applications when optimized to provide a conductive network and maintain mechanical strength (Figure 2.2).[21] These structure can direct the

electrons generated from the redox reaction of the pseudo-active materials (adsorbed-desolvated ions) flow through the tubular carbon structures to current collector instead of through electrolyte, downsizing the energy consumed by electrolyte or dielectric active materials to a insignificant level.

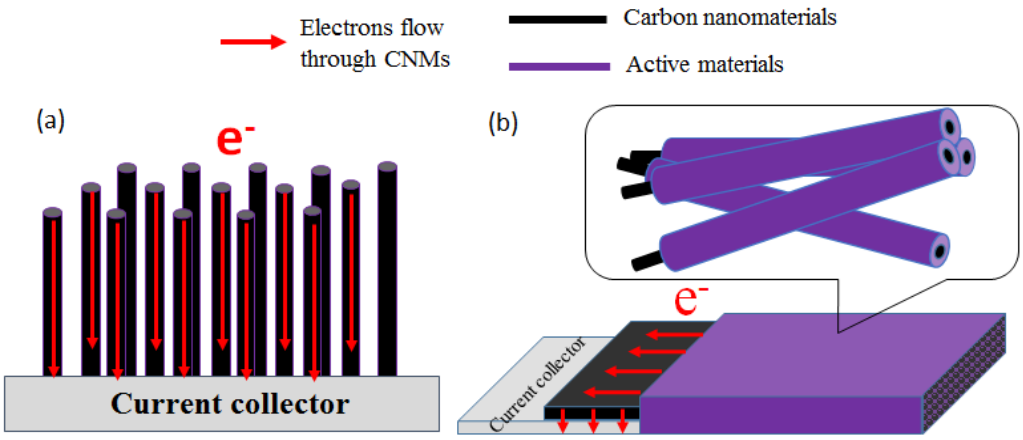

Figure 2.2. Schematic Illustration of Electrons Flow Through CNTF (a) and Super-aligned CNF (b) which Coupled with Active Material (MnO_2 in this Case) to the Current Collector. Red arrows indicate the electron flow through CNMs.

A number of studies report on well-aligned MnO_2/CNT and MnO_2/CNF with different morphologies and crystal structures, rarely do they address the mechanism of the MnO_2 crystal formation during the electrode preparation. In 2008, the fabrication of MnO_x nanoflowers on CNTF using techniques of chemical vapor deposition and electrodeposition was reported.[22] This study showed that MnO_x nucleated at the junctions of CNTF, rather than at the curved surfaces, during electrodeposition and demonstrated a strategy for forming MnO_2 on an aligned structure for high-capacity

electrochemical energy storage devices. The mass loading of metal oxides on CNTF is, however, limited and the synthesis of CNTF is time-consuming and costly.

Electrospun carbon nanofibers (ECNF) are well known for their inexpensive production, freestanding nature, large porosity, and high conductivity as electrode materials for supercapacitor applications. Electrospinning is a facial and versatile technique for generating ultrathin fibers especially carbon nanofibers. In electrospinning, a continuous solid fiber is drawn out of the droplet composed of a highly viscous polymer solution on the syringe needle. The high voltage electric field is applied between the needle and metal collector to introduce electrostatic repulsions forces between the surface charges and the evaporation of solvent.[23, 24] The collected fiber mats are usually with diameter range from nanometers to microns. (Figure 2.3)

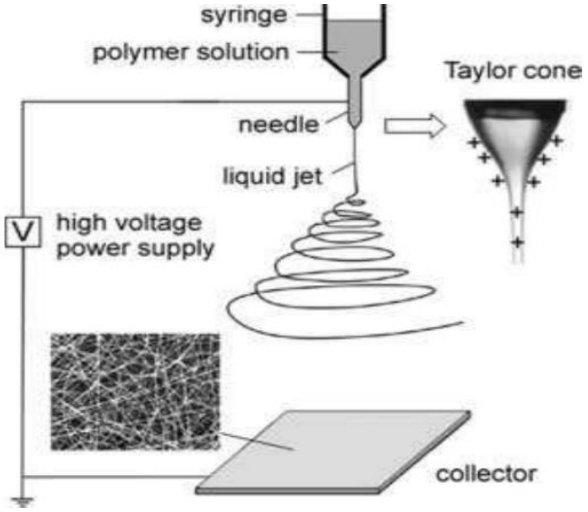

Figure 2.3. Schematic Illustration of the Setup for Electrospinning. The insets show a drawing of the electrified Taylor cone and a typical SEM image of the nonwoven mat of poly(vinyl pyrrolidone) (PVP) nanofibers. Reproduced with permission from [25].

Electrospinning usually form randomly distributed nonwoven mat due to lack of driven force and orientation control which may lead to low uniformity in thickness and homogeneity in electrical properties.[26] Yet the SA-ECNF structure can be used as scaffolds to uniformly support metal oxide nano-architectures because their alignment can significantly enhance the deposition rate by shortening the distance of electron transport. Figure 2.4 illustrates a self-designed setup for SA-ECNF synthesis. Metal oxide/carbonaceous nanomaterials are promising candidates for energy storage applications.[21] However, inhomogeneous mass and charge transfer across the electrode/electrolyte interface due to unstable metal oxide/carbonaceous nanomaterial synthesis limit their performance in supercapacitors. The above problems can be mitigated through a stable low-current electrodeposition of MnO_2 on super-aligned electrospun carbon nanofibers (SA-ECNF). The key to this approach is coupling a self-designed four steel poles collector for aligned SA-ECNF and a constant low-current (40 μA) electrodeposition technique to form a uniform Na^+ induced α-MnO_2 film which proceeds by a time-dependent growth mechanism involving cluster-"kebab" structures and ending with a compact, uniform MnO_2 film.

Because of the importance of structure of metal oxide/carbonaceous nanomaterials in determining their chemical and electrochemical properties, architectural control of metal oxides in the nano- and micro-scale regime is an important goal in materials science.[1, 27, 28] Metal oxides are essential electrode materials in lithium-ion batteries[5, 29, 30] and

pseudocapacitors/ supercapacitors,[31, 32] and the study of their stable synthesis and growth mechanism can lead to better strategies for improving their electrochemical performance in specific capacitance, energy density, and lifecycle stability.[33, 34]

We hypothesize that the combination of these two materials (MnO_2 and super-aligned SA-ECNF) in a nanoscale structure will exhibit excellent electrical, electrochemical, and mechanical properties for electrochemical energy storage. In this study, we describe the rational design and fabrication of MnO_2/SA-ECNF by wrapping MnO_2 onto super-aligned SA-ECNF. The low-current electrodeposition of the α-MnO_2 film can be described by a three-stage growth process. The as-prepared MnO_2/SA-ECNF (formed by a 4 h electrodeposition) electrode exhibits a high capacitance of 630 F/g, high specific energy density of 56.4 Wh/kg and flexibility, enabling a practical supercapacitor with a lifespan of 2000 cycles of a desirable retention value.

II.II Synthsis of SA-ECNF

The fabrication technique for the super-aligned SA-ECNF is based on a facile electrospinning method with a self-designed sample collector; see the schematic diagram in Figure 2.4a. Different from a normal cylinder design, four steel poles were welded on a plate in order to collect the SA-ECNF without any substrates. A 10 wt.% polyacrylonitrile (PAN, Mw = 150,000) solution in dimethylformamide was electrospun onto the collector. The applied positive voltage was 18 kV and the distance between the needle tip and the

collector was 15 cm. The collector was maintained at a rate of 2000 revolutions per minute during the electrospinning to form super-aligned precursors. The obtained sheets were then put into a furnace for stabilization to ensure that the fibers did not melt during pyrolysis. The heating rate was 1 °C/min from room temperature to 280 °C and kept for 6 h. The as-stabilized nanofibers were finally carbonized at 1200 °C for 1 h at a heating rate of 5 °C/min under N_2 atmosphere to yield high mechanical strength SA-ECNF.

II.III MnO_2 Electrodeposition on SA-ECNF

After the super-aligned SA-ECNF were prepared, MnO_2 was electrodeposited onto 1 cm^2 SA-ECNF by a galvanostatic method with a three-electrode setup using a charging current of 40 μA. Here, an Au electrode taped with SA-ECNF, platinum wire, and Ag/AgCl were used as working electrode, counter electrode, and reference electrode, respectively. To assure that the deposition of MnO_2 took place uniformly and firmly at the SA-ECNF' surfaces, the SA-ECNF electrode was treated with 4 M HNO_3 solution at 70 ℃ for 2 h to introduce –OH and –COOH groups to facilitate the deposition. An aqueous precursor solution with 10 mM $MnSO_4$ and 100 mM Na_2SO_4 was used as the supporting electrolyte. After the deposition, the working electrodes were washed with deionized water and then dried at 80 °C for 5 h.

II.IV Materials Characterization

Field emission scanning electron microscope (FESEM) (Carl Zeiss Auriga-BU FIB FESEM Microscope) was performed to study the morphological properties of MnO_2/SA-ECNF.

X-ray powder diffraction (XRD) (Agilent Technologies Oxford Germini X-Ray Diffractometer) was employed to study the crystal structures of MnO_2/SA-ECNF.

Energy-dispersive X-ray spectroscopy (EDX) (Hitachi S-4800-I FESEM w/Backscattered Detector & EDX) was performed to study the atomic ratio on MnO_2/SA-ECNF.

X-ray photoelectron spectroscopy (XPS, Thermo Fisher ESCALAB 250 Xi) was used to determine the elemental composition of MnO_2/SA-ECNF.

II.V Electrochemical Measurements

Electrochemical performance of the as-prepared electrodes was performed on a bio-logic VMP3 electrochemical workstation using a three-electrode system. The SA-ECNF film was cut into 1 cm^2 pieces then attached onto a gold electrode as the working electrode. A platinum wire was used as the counter-electrode and Ag/AgCl was used as the reference electrode in a 6 M KOH electrolyte solution.

The three-electrode was used for cyclic voltammetry (CV), electrochemical impedance spectroscopy (EIS), and galvanostatic charge/discharge experiments.

The voltammetry was scanned from a potential of 0.0 V to 0.8 V vs Ag/AgCl at different scan rates. Electrochemical impedance spectroscopy (EIS) was performed from 100 kHz to 0.1 Hz, and charge/discharge tests were performed at different current densities.

II.VI Calculation Section

From the cyclic voltammograms, the specific capacitance was calculated using the following equation: [1-3]

$$C = \int_{E_1}^{E_2} \frac{idE}{2mS(E_2 - E_1)} \tag{2.1}$$

From the charge/discharge curves, the specific capacitance was calculated using the following equation:

$$C = \frac{It}{m(E_2 - E_1)} \tag{2.2}$$

where C is the specific capacitance (F/g), $\int_{E_1}^{E_2} idE$ is the integrated area in the voltammograms, m is the mass of the active sample (g), S is the scan rate (V/s), (E_2-E_1) is the potential window (V), I is the discharge current (A), and t is the discharge time in the potential window (s).

The energy density (D_e) of the capacitors was calculated using the following equation:

$$D_e = C(E_2 - E_1)^2 / 2 \quad (2.3)$$

The power density (D_p) of the capacitors was calculated using the following equation:

$$D_e = D_p / t \quad (2.4)$$

where t is the discharge time.

II.VII Results

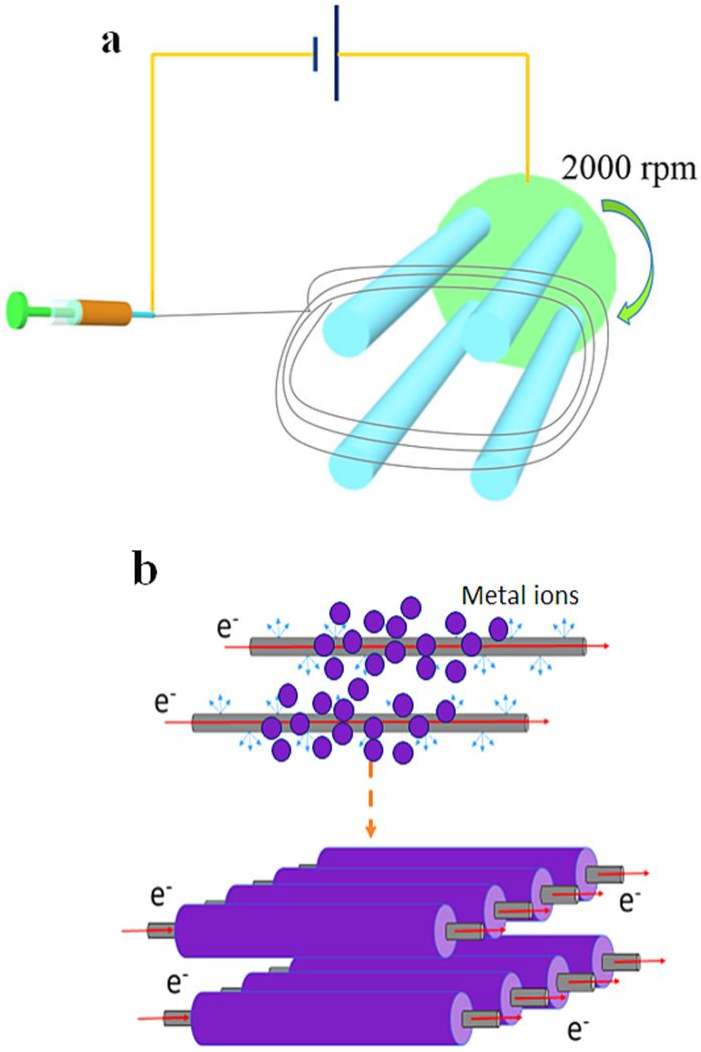

Figure 2.4. (a) Illustrations of the Aligned Electrospinning Technique. (b) ordered electron flows that initiate uniform electrodeposition on the super-aligned SA-ECNF using a three-electrode setup with a SA-ECNF working electrode, an Ag/AgCl reference electrode, and a platinum counter electrode.

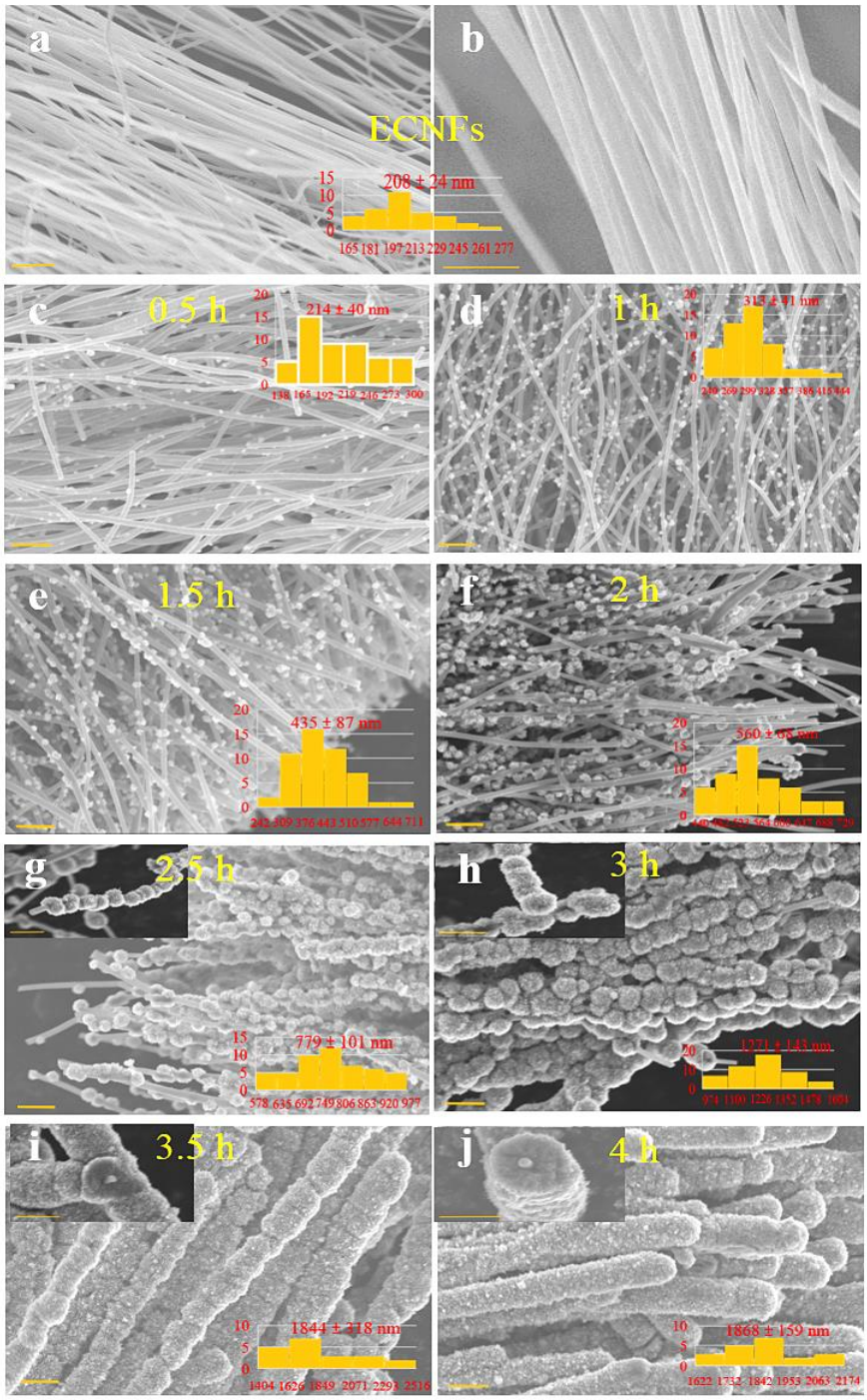

Figure 2.5. SEM Images of Super-aligned SA-ECNF and MnO_2/SA-ECNF for Different Electrodeposition Times from 0.5 h to 4 h with the Histograms of Size Distribution Analysis. All of the scale bars are 2 μm. Note that enlarged images are shown for super-aligned SA-ECNF and MnO_2/SA-ECNF (2.5 h, 3 h, 3.5 h, and 4 h).

The as-prepared pure SA-ECNF exhibit super-aligned structure (Figure 2.5a-b). It is hypothesized that the alignment of SA-ECNF can reduce disordered electron flow, leading to a more uniform electrodeposition process. A nitric acid pre-treatment, which introduces hydroxyl and carboxyl groups, was used to make the SA-ECNF surface more hydrophilic and to introduce reaction sites for nucleation of MnO_2 crystallites. MnO_2 was electrodeposited onto the SA-ECNF with a three-electrode setup (Figure 2.4b). A constant low current (40 μA) was applied by an electrochemical workstation for various times ranging from 0.5 h to 4 h under an inert N_2 atmosphere with an aqueous precursor solution containing 10 mM $MnSO_4$ and 100 mM Na_2SO_4. The composites' structure and morphology were characterized by scanning electron microscopy (SEM) (Figure 2.5c-j). When the electrodeposition starts, small clusters form on the functionalized sites distributed on the fibers (Figure 2.5c-d). As the electrodeposition continues, the clusters begin to grow larger into a morphology (Figure 2.5e-f) that is denser than that of the porous flowers reported elsewhere using high current or cyclic voltammetry (CV) techniques in the electrodeposition.[9-11, 35] After electrodeposition for 2 h, the clusters begin to merge with one another to form small balls around the SA-ECNF (Figure 2.7a-b); the SEM images clearly show surface structures corresponding to these firmly merged balls (Figure 2.5g-h). As the electrodeposition time increases, the "kebab"-like structures keep growing until the fibers are fully covered (Figure 2.5i-j, Figure 2.6a-b).

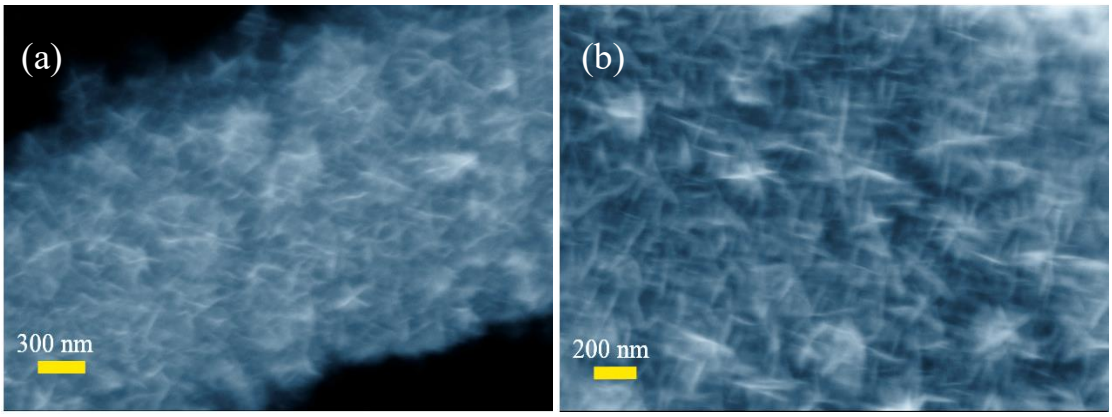

Figure 2.6. SEM Image of Aligned MnO_2/SA-ECNF After Deposition Time for 4 Hours Showing Detail Structures of MnO_2 Crystals at Different Magnifications.

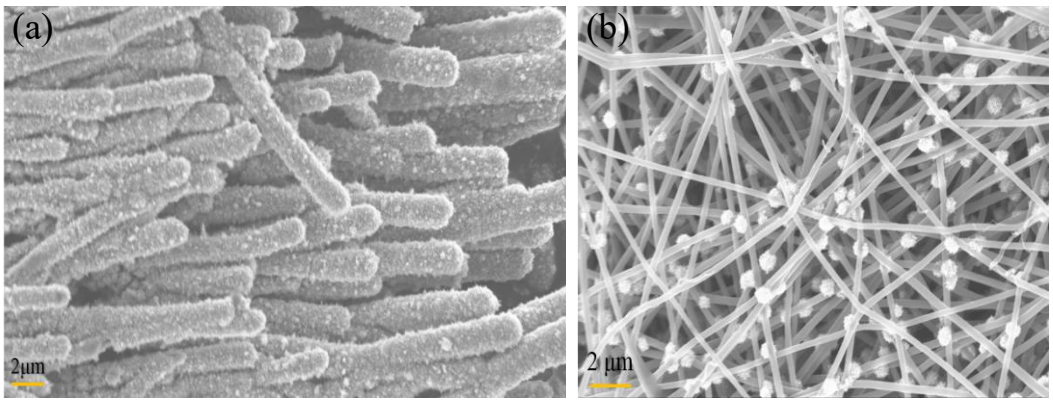

Figure 2.7. SEM Image of Aligned MnO_2/SA-ECNF After Deposition Time for 8 Hours (a) and MnO_2/SA-ECNF without Alignment After Deposition Time for 3 Hours (b).

A size distribution analysis shows a monotonic increase in average size of the nodules ("kebab"-like structures) with the increase of the electrodeposition time (Figure 2.5c-j). After electrodeposition for 4 h, the SA-ECNF with nanofiber diameter of about 208 nm are decorated by a MnO_2 film with a thickness of about 1660 nm, making a total diameter of ~1868 nm (Figure 2.5j, Figure 2.6a-b). MnO_2 electrodeposition beyond a 4 h time (Figure 2.7a of 8 h deposition) does not show an obvious increase in thickness with

the applied current, a feature that probably arises from the high resistance of the MnO_2 layers. In a control experiment, MnO_2 was electrodeposited on randomly distributed SA-ECNF using the same electrochemical conditions (Figure 2.7b). Under these conditions MnO_2 favors the nucleation and growth of clusters at the junctions of SA-ECNF rather than the uniform distribution along the fiber surfaces that is found for super-aligned SA-ECNF. These data corroborate the inference that the SA-ECNF' alignment promotes the homogenous electron flow and facilitates the uniform MnO_2 growth.

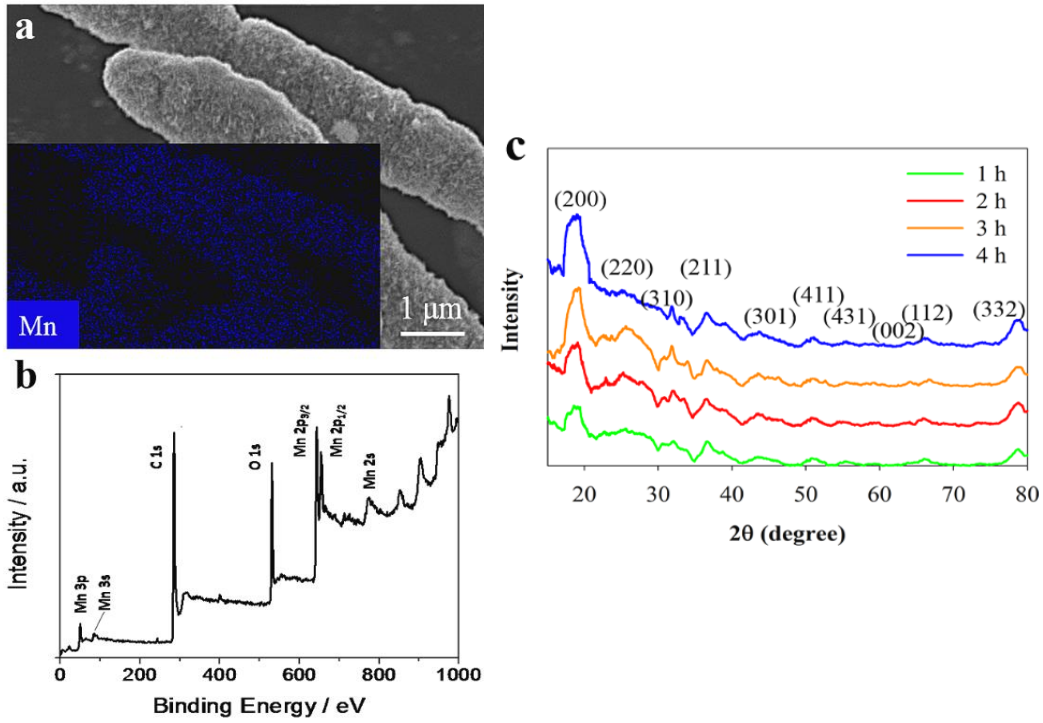

Figure 2.8. (a) SEM Associated with EDX Mapping Analysis and (b) XPS Spectrum of the MnO_2/SA-ECNF Under Electrodeposition for 4 h. (c) XRD analysis of the MnO_2/SA-ECNF under electrodeposition for 1 h, 2 h, 3 h, and 4 h.

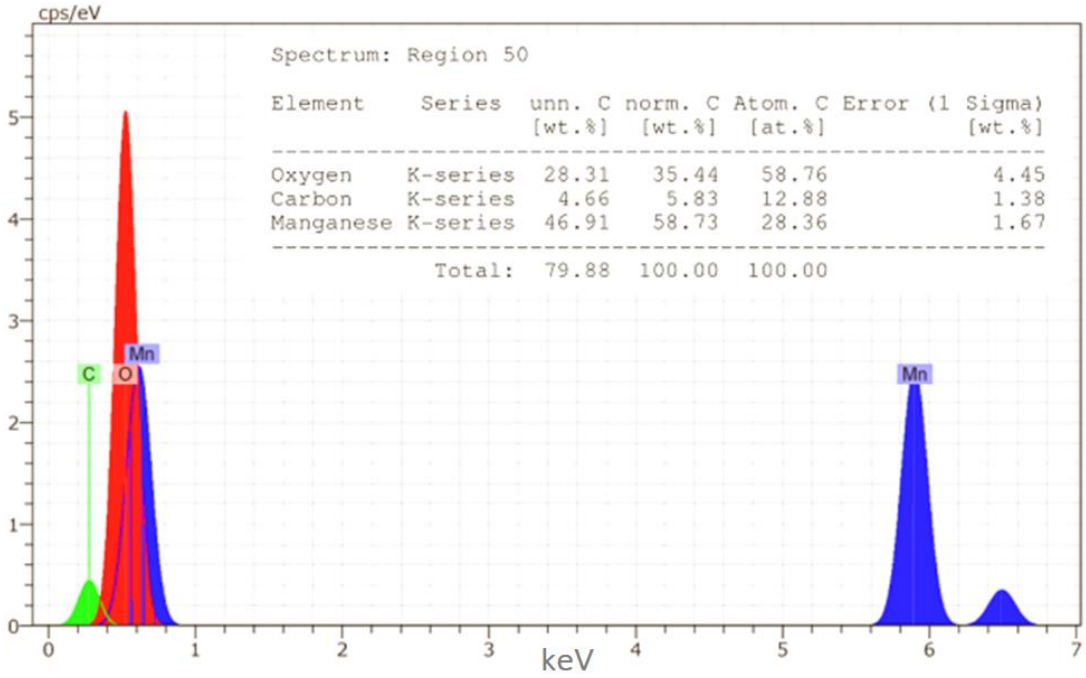

Figure 2.9 EDX of MnO_2/SA-ECNF after Electrodeposition for 4 Hours. The atom% of C, O and Mn is 12.88%, 58.76%, 28.36% respectively.

The chemical composition of the MnO_2/SA-ECNF was analyzed by energy dispersive X-ray (EDX) spectroscopy and X-ray photoelectron spectroscopy (XPS). The EDX spectrum (Figure 2.8a, Figure 2.9) shows that the surface composition of the electrochemically deposited electrodes is composed of the elements C, O, and Mn. The atomic ratio of O and Mn is close to 2:1, which implies the formation of MnO_2. The chemical composition of the MnO_2/SA-ECNF sample was also investigated by XPS. The strong C (supported by SA-ECNF (Figure 2.10b)), Mn, and O signals in the survey XPS spectrum reveal the existence of Mn atoms (Figure 2.8b). The high resolution Mn 2p spectra for MnO_2/SA-ECNF is presented in Figure 2.11. Two strong peaks at 642.3 and

653.9 eV can be clearly seen, corresponding to the Mn $2p_{3/2}$ and Mn $2p_{1/2}$ spin–orbit peaks of MnO_2, respectively.[36, 37] The pronounced peak in the O 1s XPS spectrum (Figure 2.12) at 530.0 eV is assigned to Mn−O−Mn in the composite, and the peak at 531.4 eV can be assigned to Mn-OH formation.[38, 39]

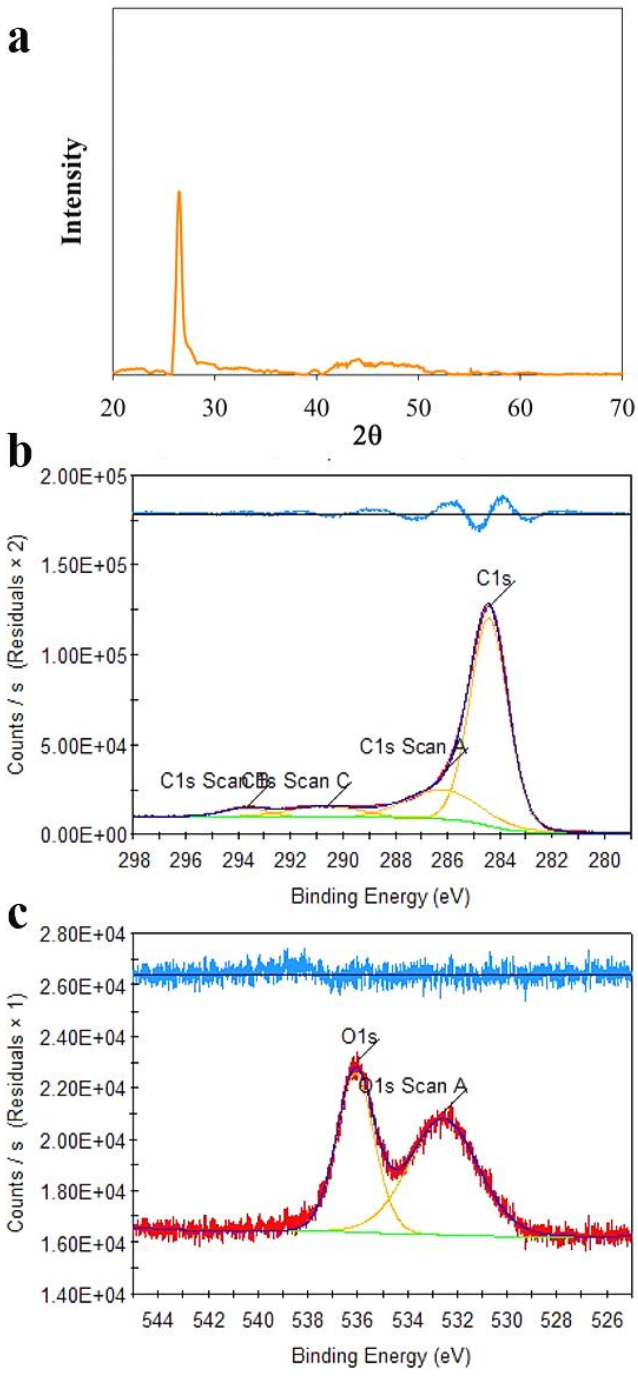

Figure 2.10. XRD (a) and XPS (with C (b) and O (c)) of the Pure SA-ECNF.

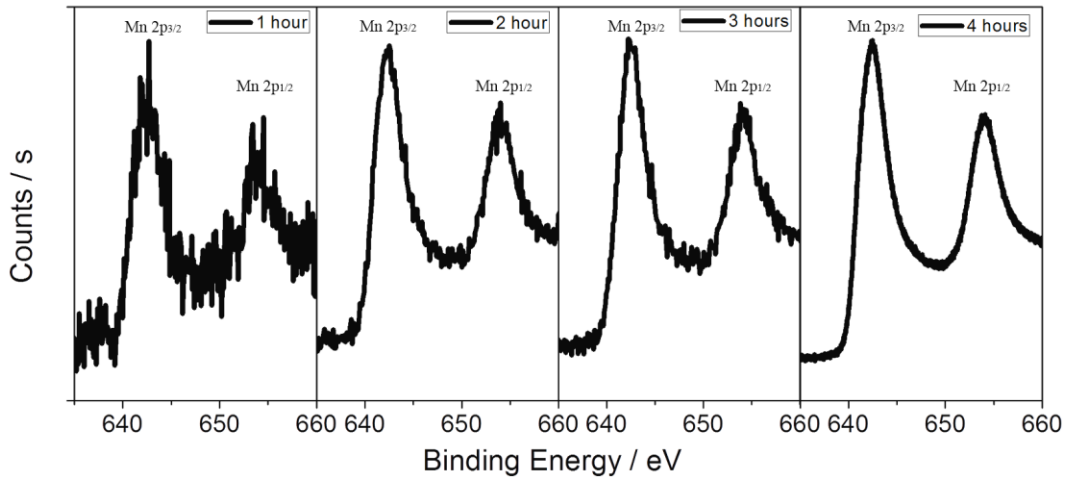

Figure 2.11. Mn 2p XPS Spectrum of the MnO_2/SA-ECNF Under Electrodeposition for 1 h, 2 h, 3 h, and 4 h.

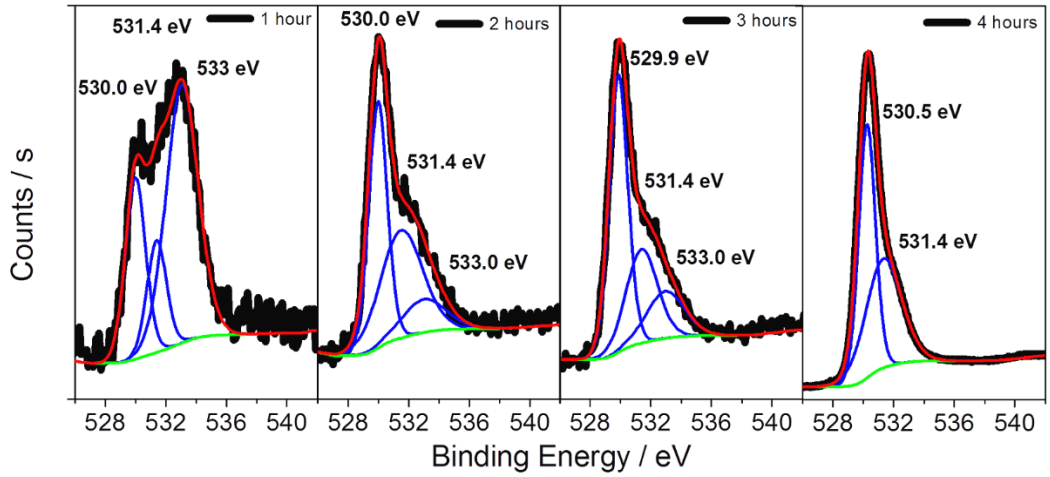

Figure 2.12. O1s XPS Spectrum (Black Line) and Its Simulated Peak Fitting (Blue Lines) of the MnO_2/SA-ECNF Under Electrodeposition for 1 h, 2 h, 3 h, and 4 h. The green line is the background for the XPS spectrum. The peak at 530.0 is associated with Mn-O-Mn, the peak at 531.4 is associated with Mn-OH and the peak at 533.0 is associated with H-O-H.

To investigate the MnO_2 crystal structure, the as-prepared MnO_2/SA-ECNF materials were examined by X-ray diffraction (XRD) (Figure 2.8c). The XRD patterns could be fully indexed to α-MnO_2 (JCPDS No. 44-0141), and become more distinct (like the (200) plane) with longer electrodeposition time.[40]

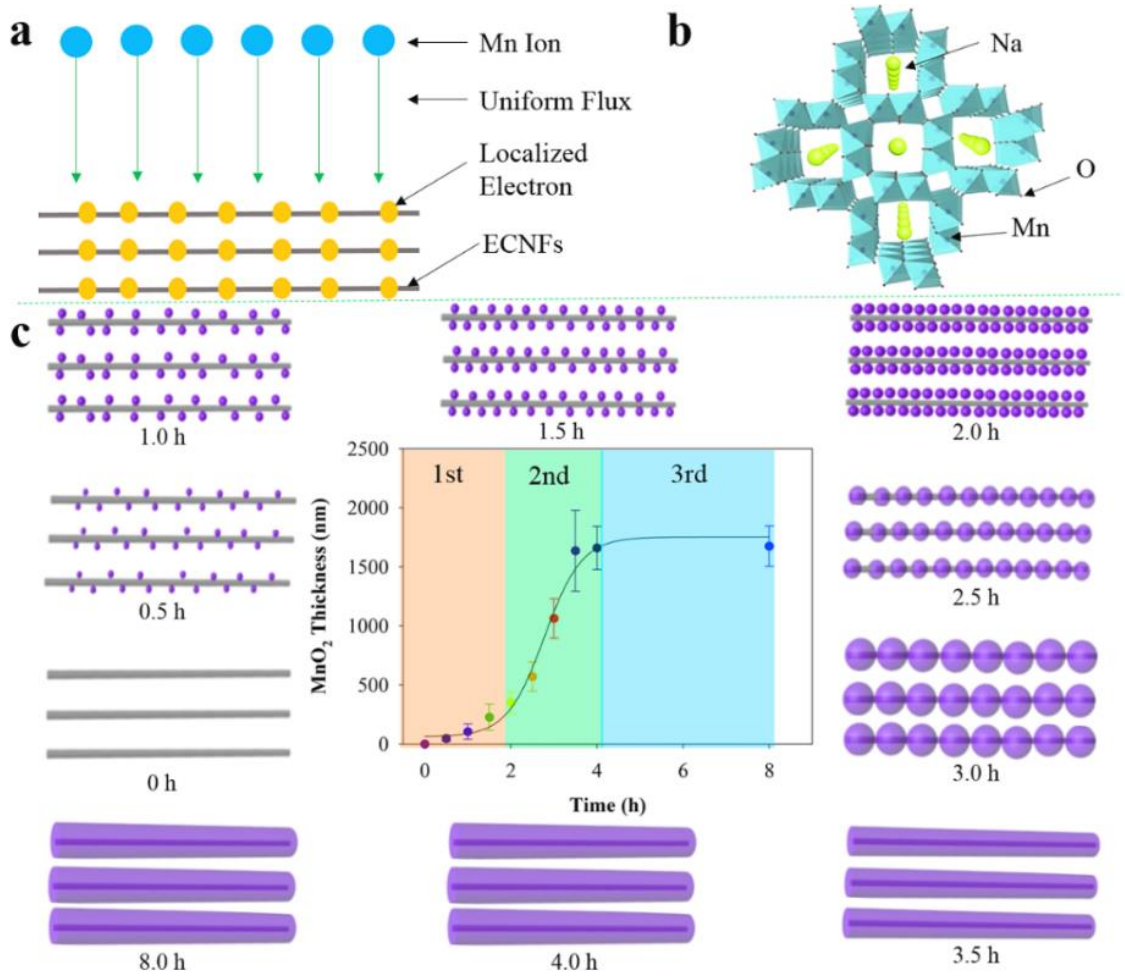

Figure 2.13. Mechanistic View of the MnO_2 Growth Including the Schematic Description of Mn^{2+} Uniform Flux. (a), α-MnO_2 crystalline (b), and time-dependent MnO_2 growth with data analysis (c).

The comprehensive electrodeposition of MnO_2 originates from the stable structure of SA-ECNF, which contributes to a uniform Mn^{2+} flux (Figure 2.13a).

The electrochemical reaction occurs according to:[41]

$$Mn^{2+} + 2H_2O \rightarrow MnO_2 + 4H^+ + 2e^-$$

The MnO_2 matrix has different structural motifs arising from edge- or corner-sharing MnO_6 octahedra in different connectivity schemes, resulting in channels that extend in a direction parallel to the unit cell; and the MnO_2 appears in a number of crystallographic polymorphs, such as α-, β-, γ-, δ-, and ε-MnO_2.[42, 43] In this study, cations (Na^+) were introduced during the synthetic process, but the 1×1 channels (with a size of 0.189 nm) are too small for Na^+ to intercalate and stabilize the structure, which results in the formation of α-MnO_2.

In contrast double chains of edge-sharing MnO_6 octahedra, which are linked at the corners to form 2×2 channels (with a size of 0.46 nm) and 1×1 tunnel structures, are large enough for cation placement (Figure 2.13b).[42, 43] The cations, which reside inside the 2×2 channels of α-MnO_2, increase the electronic conductivity of the MnO_2/SA-ECNF' system and indirectly enhance the electrodeposition of α-MnO_2.[44] The time-dependent growth analysis suggests a three-step kinetics mechanism for the electrodeposition (Figure 2.13c).

The first step involves small cluster formation on a boundary layer distributed along the fibers (0-2 h).

The second step involves “kebab”-like structure formation and growth from small to big nodules of MnO_2 around the SA-ECNF (2-4 h).

The final step involves the cessation of MnO_2 nodule growth and establishment of a dense film with a self-limiting thickness (>4 h).

In the growth process, the thickness of the MnO_2 film can be controlled by the electrodeposition time (Figure 2.5).

We can write a kinetic equation (2.5) to describe the MnO_2 growth for the electrodeposition as:[45]

$$dh/dt = c\left(j - j_d\right) \tag{2.5}$$

where dh/dt is the rate of MnO_2 film formation and growth, c is the coulombic efficiency (cm^3/C), j is the measured current density, and j_d is the required current density to prevent dissolution. The measured current density has a nonlinear exponential relationship with the applied voltage (V):[46]

$$\mathrm{j} = \mathrm{A}\exp(\mathrm{B}\cdot \mathrm{V}/\mathrm{h}) \tag{2.6}$$

where A and B are characteristic constants of the system. According to the nonlinear relationship between current density and electric field strength, the saturation of film growth is thus given by the equation:

$$h_{\max} = BV \Big/ \left(\ln\left(j_d / A \right) \right) \tag{2.7}$$

Figure 4c shows a best fit of the MnO_2 thickness (h) versus deposition time (t) data by the equation:

$$h = h_{\max} \Big/ (1 + 10^{(\tau_{0.5} - t)}) \left(t > 0 \right) \tag{2.8}$$

with a h_{max} of about 1693 nm and a half-life time constant ($\tau_{0.5}$) of about 2.78 h. The MnO_2 thickness increases in a time-dependent manner (from 0.5 h to 8 h) until the MnO_2 thickness is observed to plateau after 4 hours of electrodeposition, which supports a three-stage kinetic mechanism for the MnO_2 electrodeposition process.

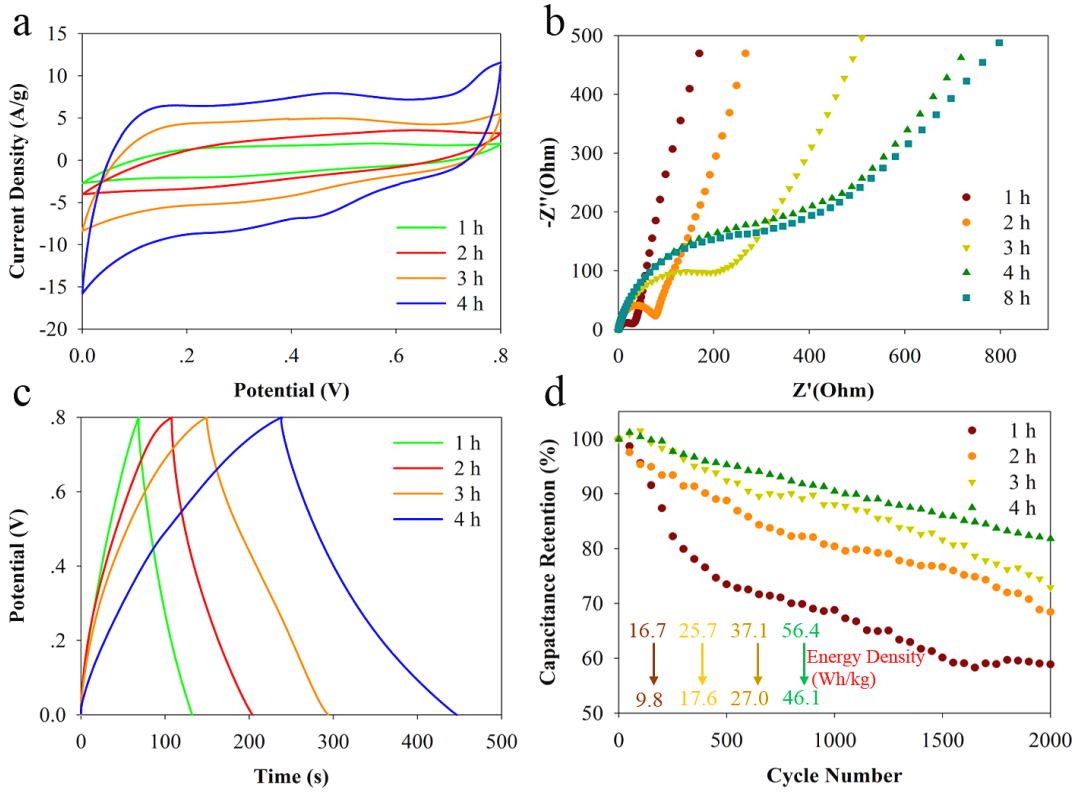

Figure 2.14. Electrochemical Characterization of the Films Includes Cyclic Voltammetry at 20 mV/s in 6.0 M KOH Electrolyte. (a), electrochemical impedance spectroscopy at frequencies from 100 kHz to 0.1 Hz (b), galvanic charge-discharge profiles at 1 A/g (c), and retention performance (d) of MnO2/SA-ECNF under 1 h, 2 h, 3 h and 4 h electrodeposition. Note that the impedance spectra also include an 8 h electrodeposition data and the insert in (d) shows the specific energy density changes after 2000 cycles.

The as-prepared MnO_2/SA-ECNF films were examined for their performance as supercapacitor electrodes. Cyclic voltammetry studies (Figure 2.14a, Figure 2.15) in a three electrode-electrochemical cell with 6.0 M KOH electrolyte solution were performed to calculate the specific capacitance of the MnO_2/SA-ECNF electrodes (details in Experimental Section).

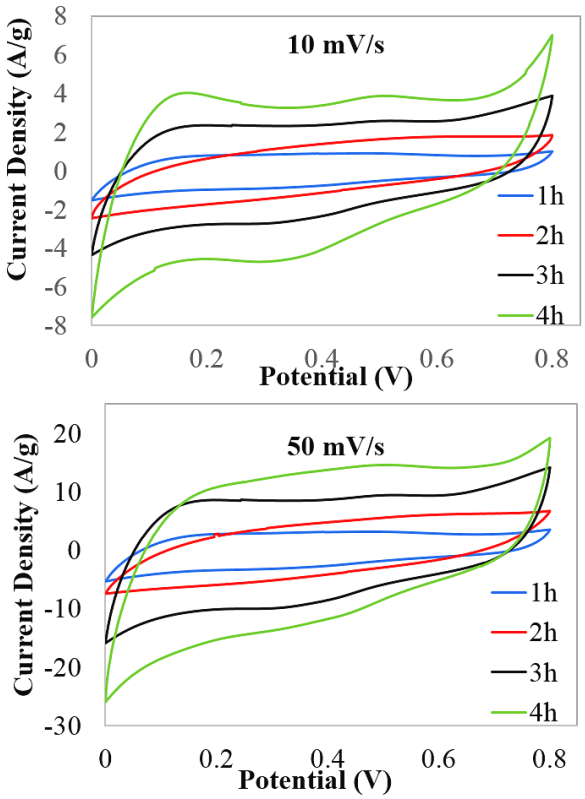

Figure 2.15. Cyclic Voltammetry of MnO_2/SA-ECNF Electrodes at 10 mV/s and 50 mV/s in 6.0 M KOH Electrolyte Solution.

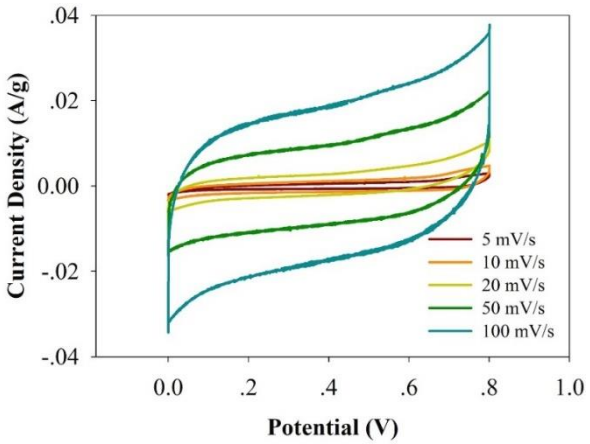

Figure 2.16. CV of the Pure SA-ECNF Electrodes Tested at Different Scan Rates.

The specific capacitance calculated with respect to the whole mass of the MnO_2/SA-ECNF electrodes shows a monotonic increase with the MnO_2 electrodeposition time (up to 4 h). The capacitance of the MnO_2/SA-ECNF with 1h, 2h, 3h, and 4h deposition is 146, 219, 336, and 630 F/g, respectively.

MnO_2/SA-ECNF electrodes with less than 2 h electrodeposition time show an enhanced specific capacitance as compared to bare SA-ECNF (Figure 2.16) while maintaining flat (parallelogram) voltammogram shapes. Moreover, the MnO_2/SA-ECNF electrode possesses a combined contribution of the electrochemical double layer capacitance and the pseudocapacitance from MnO_2. The double layer stores charge electrostatically, mainly based on the specific surface area and the adsorption of ions at electrode surface. The pseudo-capacitance depends on the reversible redox reactions between Mn(IV)/Mn(III) species and K^+ intercalation/de-intercalation at the MnO_2/electrolyte interfaces.[47-49] The longer electrodeposition (3 h and 4 h) results in thicker and more uniform MnO_2 films, which enhances the successive multiple surface redox reactions between the Mn(IV)/Mn(III) complexes as the redox peaks in Figure 5a shown.

The electrochemical equilibrium involves the KOH electrolyte and can be expressed as:[31, 50]

$$Mn(IV)O_2 + mH^+ + nK^+ \leftrightarrow Mn(III)Mn(IV)OOH_mK_n$$

In addition, the presence of K^+ inside the 2×2 channels of the α-MnO_2 has a strong beneficial effect on the electrochemical performance of the electrodes by enhancing the electronic conductivity through electron hopping between Mn^{4+}/Mn^{3+}. The MnO_2/SA-ECNF electrodes with 3 h (charge transfer resistance of about 257 Ohms) and 4 h (charge transfer resistance of about 326 Ohms) electrodeposition have higher resistance, which is deduced from the electrochemical impedance spectroscopy (EIS) Nyquist plots (Figure 2.14b). These plots consist of a semicircle in the high-frequency region and a straight line in the low-frequency region, which display an increase in charge transfer resistance and diffusive resistance with an increase in electrodeposition time.[51, 52] No obvious difference was found between the 4 h and 8 h electrodeposited MnO_2/SA-ECNF, further corroborating the conclusion that MnO_2 film growth ceases after 4 h of electrodeposition.

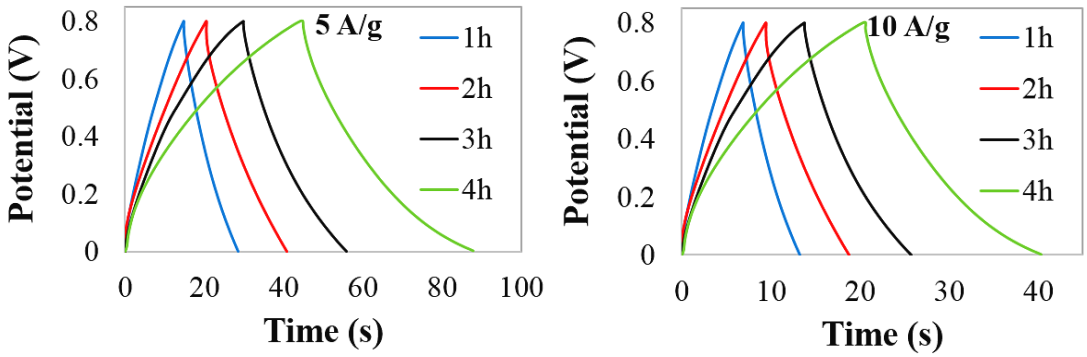

Figure 2.17. Galvanic Charge-discharge Profiles of MnO_2/SA-ECNF Electrodes at 5 A/g and 10 A/g.

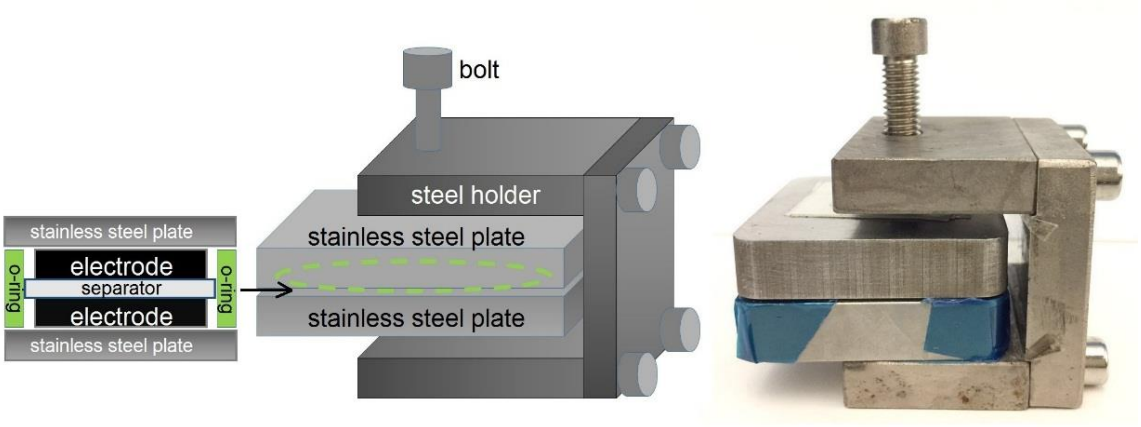

Figure 2.18. Schematic and Photo of a Self-designed Platform. It consists of two stainless steel plates as current collectors, an o-ring to seal the cell, U-shape holder and a fasten bolt to adjust the distance between the electrodes.

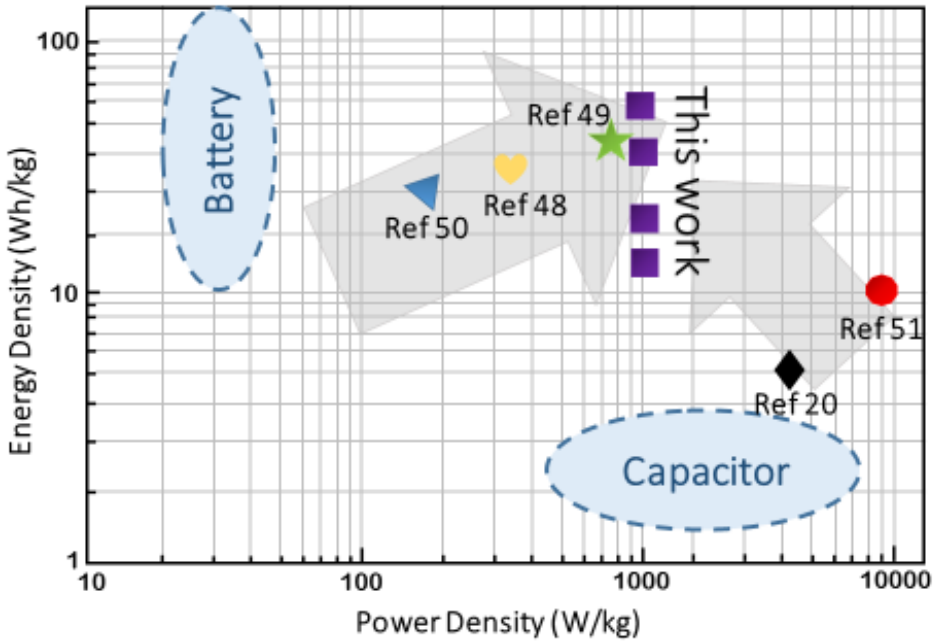

Figure 2.19. Ragone Plot of this Work Compare to Others.

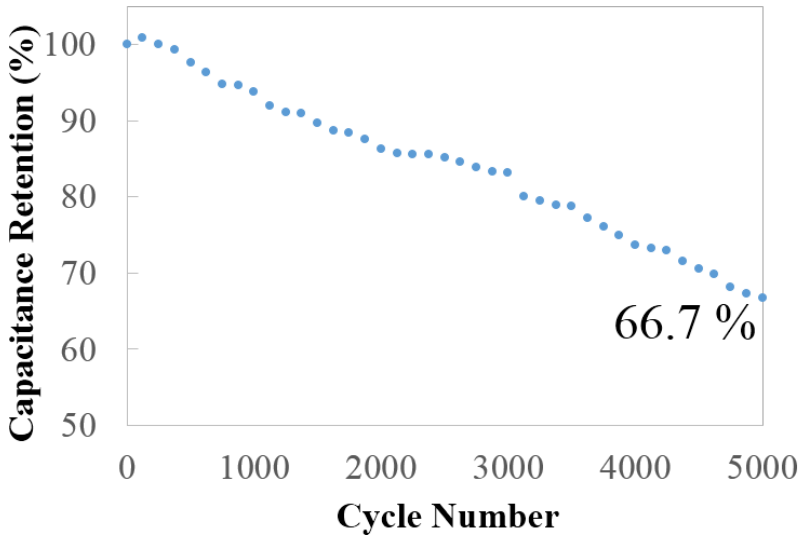

Figure 2.20. Retention Performance at 1 A/g of MnO_2/SA-ECNF Under 4 h Electrodeposition.

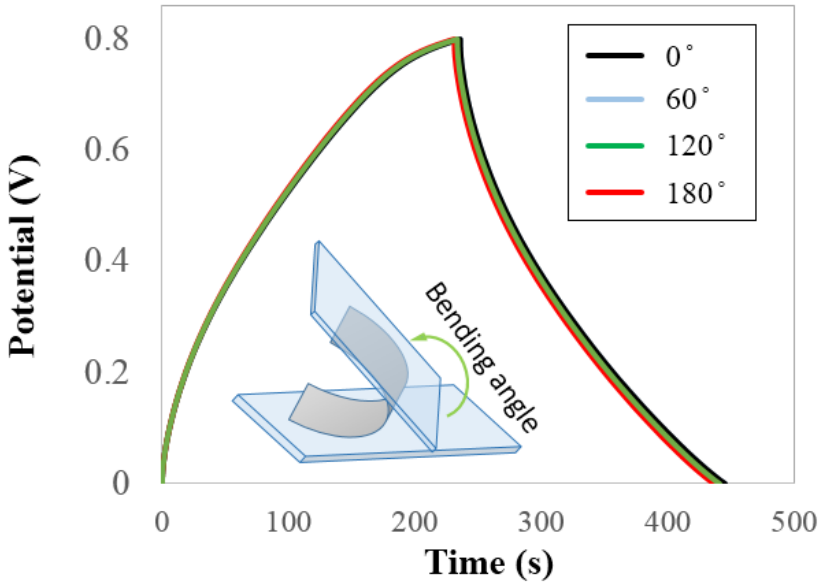

Figure 2.21. Charge-discharge with Folding with 0° (original), 60°, 120°, 180°, Respectively.

The galvanic charge/discharge time under longer electrodeposition time increases more significantly than that under shorter electrodeposition time (Figure 2.14c, Figure 2.17). Note that both EIS and galvanic charge−discharge were tested in a self-designed symmetrical capacitor platform (Figure 2.18, provided by colleagues for supercapacitor testing[30-32]) assembled in a glove box.

For practical purposes, retention tests were also performed for up to 2000 cycles of charge and discharge at current densities of 1 A/g. Figure 2.14d shows the first cycle of each sample and its specific energy density is 16.7, 25.7, 37.1, and 56.4 Wh/kg, respectively. Considering that a power density of around 1 kW/kg was achieved at the current density of 10 A/g, it is superior among most recent reports (Figure 2.19[53-56]).

After 2000 cycles, the MnO_2/SA-ECNF electrode with 1 h electrodeposition drops to 58.9% of its initial energy density. This loss may occur because the small MnO_2 clusters have higher surface contact with the electrolyte and undergo irreversible solvation and reduction. The MnO_2/SA-ECNF electrodes with 2 h and 3 h electrodeposition show higher retention performances of 68.4% and 72.9%, respectively.

The 4 h MnO_2/SA-ECNF electrode has the highest retention value of 81.8 % (an extended test of 5000 cycles were performed with retention value of 66.7 % in Figure 2.20) which agrees with the conclusion that the compact and uniform MnO_2 coatings provide stable ion exchange and charge-discharge rates while maintaining a high pseudocapacitance. In order to verify its flexibility, a folding test was also performed. The

4 h MnO_2/SA-ECNF electrode can be folded at different degrees within 2% changes in discharge time. (Figure 2.21)

II.VIII Conclusions

This work demonstrates a new strategy for uniformly electrodepositing MnO_2 on aligned SA-ECNF and the change in the mechanism of MnO_2 growth with the electrodeposition time was explored. In contrast to earlier studies with a much higher current, the reported electrodeposition was conducted with a constant low-current of 40 μA. Film growth proceeds by a three-stage kinetic process with a halfway growth time of 2.78 h. From the electrochemical performance, MnO_2/SA-ECNF with a 4 h electrodeposition display a high capacitance of 630 F/g and a specific energy density of 56.4 Wh/kg. These findings represent a significant improvement in stable metal oxide/carbonaceous nanomaterial-based pseudocapacitance energy storage.

II.IX References

[1] S. Mann, Angewandte Chemie International Edition, 39 (2000) 3392-3406.

[2] Z. Zeng, Y. Liu, W. Zhang, H. Chevva, J. Wei, Journal of Power Sources, 358 (2017) 22-28.

[3] M. Antonietti, G.A. Ozin, Chemistry – A European Journal, 10 (2004) 28-41.

[4] H. Cölfen, S. Mann, Angewandte Chemie International Edition, 42 (2003) 2350-2365.

[5] P. Poizot, S. Laruelle, S. Grugeon, L. Dupont, J.M. Tarascon, Nature, 407 (2000) 496-499.

[6] Y. Wu, T. Zhang, F. Zhang, Y. Wang, Y. Ma, Y. Huang, Y. Liu, Y. Chen, Nano Energy, 1 (2012) 820-827.

[7] A.S. Arico, P. Bruce, B. Scrosati, J.-M. Tarascon, W. van Schalkwijk, Nat Mater, 4 (2005) 366-377.

[8] L. Hu, W. Chen, X. Xie, N. Liu, Y. Yang, H. Wu, Y. Yao, M. Pasta, H.N. Alshareef, Y. Cui, Acs Nano, 5 (2011) 8904-8913.

[9] Y. Jiang, X. Ling, Z. Jiao, L. Li, Q. Ma, M. Wu, Y. Chu, B. Zhao, Electrochimica Acta, 153 (2015) 246-253.

[10] P. Yang, Y. Chen, X. Yu, P. Qiang, K. Wang, X. Cai, S. Tan, P. Liu, J. Song, W. Mai, Nano Energy, 10 (2014) 108-116.

[11] C. Choi, S.H. Kim, H.J. Sim, J.A. Lee, A.Y. Choi, Y.T. Kim, X. Lepró, G.M. Spinks, R.H. Baughman, S.J. Kim, Scientific Reports, 5 (2015) 9387.

[12] K. Liang, T. Gu, Z. Cao, X. Tang, W. Hu, B. Wei, Nano Energy, 9 (2014) 245-251.

[13] R. Amade, E. Jover, B. Caglar, T. Mutlu, E. Bertran, Journal of Power Sources, 196 (2011) 5779-5783.

[14] L. Peng, X. Peng, B. Liu, C. Wu, Y. Xie, G. Yu, Nano Letters, 13 (2013) 2151-2157.

[15] S.-M. Li, Y.-S. Wang, S.-Y. Yang, C.-H. Liu, K.-H. Chang, H.-W. Tien, N.-T. Wen, C.-C.M. Ma, C.-C. Hu, Journal of Power Sources, 225 (2013) 347-355.

[16] L. Deng, Z. Hao, J. Wang, G. Zhu, L. Kang, Z.-H. Liu, Z. Yang, Z. Wang, Electrochimica Acta, 89 (2013) 191-198.

[17] D. Momodu, A. Bello, J. Dangbegnon, F. Barzeger, F. Taghizadeh, M. Fabiane, A.T.C. Johnson, N. Manyala, AIP Advances, 4 (2014) 097122.

[18] Y. He, W. Chen, J. Zhou, X. Li, P. Tang, Z. Zhang, J. Fu, E. Xie, ACS Applied Materials & Interfaces, 6 (2014) 210-218.

[19] Z. Yu, M. McInnis, J. Calderon, S. Seal, L. Zhai, J. Thomas, Nano Energy, 11 (2015) 611-620.

[20] J. G. Wang, Y. Yang, Z.-H. Huang, F. Kang, Carbon, 61 (2013) 190-199.

[21] Y. Liu, Z. Zeng, J. Wei, Frontiers in Nanoscience and Nanotechnology, 2 (2016) 78-85.

[22] H. Zhang, G. Cao, Z. Wang, Y. Yang, Z. Shi, Z. Gu, Nano letters, 8 (2008) 2664-2668.

[23] Z. Zeng, Y. Liu, W. Zhang, H. Chevva, J. Wei, Journal of Power Sources, 358 (2017) 22-28.

[24] A. Aboagye, H. Elbohy, A.D. Kelkar, Q. Qiao, J. Zai, X. Qian, L. Zhang, Nano Energy, 11 (2015) 550-556.

[25] D. Li, Y. Xia, Advanced materials, 16 (2004) 1151-1170.

[26] S.F. Fennessey, R.J. Farris, Polymer, 45 (2004) 4217-4225.

[27] M. Antonietti, G.A. Ozin, Chemistry–A European Journal, 10 (2004) 28-41.

[28] H. Cölfen, S. Mann, Angewandte Chemie International Edition, 42 (2003) 2350-2365.

[29] J.M. Tarascon, M. Armand, Nature, 414 (2001) 359-367.

[30] N. Fukata, M. Mitome, Y. Bando, W. Wu, Z.L. Wang, Nano Energy, 26 (2016) 37-42.

[31] P. Simon, Y. Gogotsi, Nat Mater, 7 (2008) 845-854.

[32] L.L. Zhang, X.S. Zhao, Chemical Society Reviews, 38 (2009) 2520-2531.

[33] X. Xia, J. Tu, Y. Zhang, J. Chen, X. Wang, C. Gu, C. Guan, J. Luo, H.J. Fan, Chemistry of Materials, 24 (2012) 3793-3799.

[34] R. Liu, S.B. Lee, Journal of the American Chemical Society, 130 (2008) 2942-2943.

[35] J. Sodtipinta, W. Pon-On, W. Veerasai, S.M. Smith, P. Pakawatpanurut, Materials Research Bulletin, 48 (2013) 1204-1212.

[36] S.W. Lee, J. Kim, S. Chen, P.T. Hammond, ACS Nano, 4 (2010) 3889-3896.

[37] W. Zilong, Z. Zhu, J. Qiu, S. Yang, Journal of Materials Chemistry C, 2 (2014) 1331-1336.

[38] L. Yuan, X.-H. Lu, X. Xiao, T. Zhai, J. Dai, F. Zhang, B. Hu, X. Wang, L. Gong, J. Chen, C. Hu, Y. Tong, J. Zhou, Z.L. Wang, ACS Nano, 6 (2012) 656-661.

[39] J.-G. Wang, Y. Yang, Z.-H. Huang, F. Kang, Journal of Materials Chemistry, 22 (2012) 16943-16949.

[40] P. Yu, X. Zhang, D. Wang, L. Wang, Y. Ma, Crystal Growth & Design, 9 (2009) 528-533.

[41] S. Devaraj, N. Munichandraiah, Electrochemical and Solid-State Letters, 8 (2005) A373-A377.

[42] T. Gao, H. Fjellvåg, P. Norby, Analytica Chimica Acta, 648 (2009) 235-239.

[43] W. Xiao, D. Wang, X.W. Lou, The Journal of Physical Chemistry C, 114 (2010) 1694-1700.

[44] Y. Yuan, C. Zhan, K. He, H. Chen, W. Yao, S. Sharifi-Asl, B. Song, Z. Yang, A. Nie, X. Luo, H. Wang, S.M. Wood, K. Amine, M.S. Islam, J. Lu, R. Shahbazian-Yassar, Nature Communications, 7 (2016) 13374.

[45] K.J. Vetter, CHAPTER 3 - Methods of Determining Electrochemical Reaction Mechanisms, in: Electrochemical Kinetics, Academic Press, 1967, pp. 396-454.

[46] P.E. Pierce, Z. Kovac, C. Higginbotham, Industrial & Engineering Chemistry Product Research and Development, 17 (1978) 317-322.

[47] C. Liu, Z. Yu, D. Neff, A. Zhamu, B.Z. Jang, Nano letters, 10 (2010) 4863-4868.

[48] Z. Fan, J. Yan, T. Wei, L. Zhi, G. Ning, T. Li, F. Wei, Advanced Functional Materials, 21 (2011) 2366-2375.

[49] X. Dong, X. Wang, J. Wang, H. Song, X. Li, L. Wang, M.B. Chan-Park, C.M. Li, P. Chen, Carbon, 50 (2012) 4865-4870.

[50] M. Toupin, T. Brousse, D. Bélanger, Chemistry of Materials, 16 (2004) 3184-3190.

[51] C. Shang, S. Dong, S. Wang, D. Xiao, P. Han, X. Wang, L. Gu, G. Cui, ACS Nano, 7 (2013) 5430-5436.

[52] J. Xu, S. Gai, F. He, N. Niu, P. Gao, Y. Chen, P. Yang, Dalton Transactions, 43 (2014) 11667-11675.

[53] S.-C. Lin, Y.-T. Lu, Y.-A. Chien, J.-A. Wang, T.-H. You, Y.-S. Wang, C.-W. Lin, C.-C.M. Ma, C.-C. Hu, Journal of Power Sources, 362 (2017) 258-269.

[54] Y. Lv, H. Che, A. Liu, J. Mu, C. Dai, X. Zhang, Y. Bai, G. Wang, Z. Zhang, Journal of Applied Electrochemistry, 47 (2017) 433-444.

[55] M. Cakici, R.R. Kakarla, F. Alonso-Marroquin, Chemical Engineering Journal, 309 (2017) 151-158.

CHAPTER III

IMPROVED SUPERCAPACITOR PERFORMANCE OF MnO_2-ELECTROSPUN CARBON NANOFIBERS ELECTRODES BY mT MAGNETIC FIELD

This chapter has been published as: Zeng, Z., **Liu, Y.**, Zhang, W., Chevva, H., & Wei, J. Improved supercapacitor performance of MnO_2-electrospun carbon nanofibers electrodes by mT magnetic field. *Journal of Power Sources*, **2017**, *358*, 22-28.

III.I Introduction

Electrochemical double layer supercapacitors have drawn a lot of attention due to fast charging/discharging rate, increased energy density and power density, and large lifecycle stability.[1-4] However, regarding the energy storage capability, there is an emerging need to develop supercapacitors with high relative dielectric constant in the double layer and surface area of the electrode for higher energy density.[5-7] Some of the electroactive metal oxide, e.g. ruthenium oxide (RuO_2),[8] manganese oxide (MnO_x),[9] nickel oxide (NiO_x),[10] cobalt oxide (Co_3O_4),[11] tin oxide (SnO_2),[12] zinc oxide (ZnO),[13] and vanadium (V) oxide (V_2O_5) [14] etc. were used in supercapacitor (so-called pseudocapacitor) electrodes to offer fast and reversible redox reactions, contributing to higher energy density capacity.[15] To increase surface area, carbon nanomaterials, such

as carbon nanotubes (CNTs),[16] carbon nanofibers (CNFs),[17] graphene nanofoam (GF),[18] and reduced graphene oxide (rGO)[19] were used in supercapacitors, which not only provide unique size and surfacedependent properties but also excellent intrinsic chemical and physical (e.g. electrical, thermal, and mechanical) properties. Among these, electrospun carbon nanofibers (ECNFs) is known for its relatively large porosity, high conductivity, low cost in production with freestanding nature, and good scaffolds to uniformly support nanostructured metal oxide.[20]

Electrospinning is an efficient fiber production method which uses electric force to draw charged threads of polymer solutions or polymer melts up to form polymer nanofibers[21] which can be converted to porous ECNFs with subsequent carbonization.[22] Electrospinning has become a powerful and easy method to form carbon nanofibers in large scale for broad applications. It has been used for electrode production or separator materials for supercapacitors,[23-25] Li-ion batteries,[26-29] as well as preparation of electrical double-layer capacitor half-cells.[30]

Recently, the influence of an external magnetic field over the capacitance of electrodes has won some attention due to effects of Lorentz force acting on moving charges/ions, charge density gradient modulation, electron state excitation and oscillatory magnetization,[31-33] thus energy storage improvement. Two magnetic strategies for enhancing the electrochemical process in capacitors have been demonstrated. One is to introduce magnetic nanoparticles into the electrode in the presence of an external magnetic

field. For instance, Fe_2O_3/graphene nanocomposites,[33] Fe_3O_4/active carbon nanocomposites,[34] and Fe_3O_4/active carbon nanocomposites[35] demonstrated enhancement of the capacitance and energy density with an external magnetic field. The other one is to reconstruct the charge density and electric polarization in the magnetic material system. For example, ionic liquid was used in charge carrier engineering to achieve tunable dielectric permittivity.[31]

During the past years, MnO_2 has been one of the most commonly used transition-metal oxides that have been used as pseudocapacitive electrode materials due to its unique characteristics, such as easy-for-deposition, stability and significantly enhanced energy storage performance;[36,37] however, little is known about the magnetic field effect on its energy storage. Herein, for the first time, we present a magnetization-induced capacitance enhancement in MnO_2/ECNFs nanocomposite electrodes fabricated by electrochemical deposition of MnO_2 on ECNFs.

The MnO_2/ECNFs electrode was characterized by scanning electron microscopy (SEM), x-ray powder diffraction (XRD), energy-dispersive x-ray spectroscopy (EDX), Raman spectroscopy, Fourier transform infrared spectroscopy (FTIR), thermogravimetric analysis (TGA), and superconducting quantum interference device vibrating sample magnetometer (SQUID VSM). The electrochemical performance of the MnO_2/ECNFs electrodes for capacitive energy storage was studied by cyclic voltammetry (CV), galvanostatic charge/discharge, electrochemical impedance spectroscopy (EIS), and

lifecycle stability tests in the presence/absence of milli-Tesla (mT) to sub-mT magnetic fields derived by Helmholtz coils.

III.II Synthesis of MnO_2/ECNFs Nanocomposites

Electrospinning was used to produce carbon nanofibers. 10 wt.% Polyacrylonitrile (PAN, Mw = 150,000, Aldrich) solution in dimethylformamide was electrospun onto a collector to form a fiber fabric film. The applied positive voltage was 18 kV and the distance between the needle tip and the collector was 15 cm. The dense fiber fabric was collected from the steel collector covered with aluminum foil and pressed by two heated metal plates into a compact sheet at 100 °C under 5 MPa pressure for 5 min. The obtained sheet was then put into a furnace for stabilization. The heating rate was 3 °C/min from room temperature to 280 °C and kept for 2 h. The as-stabilized nanofibers were carbonized at 1000 °C for 2 h at a heating rate of 5 °C/min under N_2 atmosphere. After the ECNFs were prepared, MnO_2 was electrodeposited onto 1 cm^2 ECNFs by the galvanostatic method with a three-electrode setup using the charging current of 40 μA, and the charge time of 3 h, where Au electrode taped with ECNFs, platinum wire and Ag/AgCl were used as working electrode, counter electrode and reference electrode, respectively. To assure that the deposition of MnO_2 took place uniformly and firmly at the ECNFs' surfaces, the ECNFs electrode was treated with 5% HNO_3 solution for 2 h to introduce –OH and –COOH groups to facilitate the deposition. An aqueous precursor solution with 10 mM $MnSO_4$ and 100

mM Na_2SO_4 was used as the supporting electrolyte. After the deposition, the working electrodes were washed with distilled water and then dried at 80 °C for 5 h.

III.III Electrochemical Measurements

Electrochemical performance of the as-prepared electrodes was performed on a bio-logic VMP3 electrochemical workstation using a three-electrode testing system with a platinum wire as counter-electrode and Ag/AgCl as reference electrode in 6 M KOH electrolyte solution. The ECNFs film was cut 1 cm^2 for cyclic voltammetry (CV), electrochemical impedance spectroscopy (EIS), and galvanostatic charge/discharge tests. CV was carried out at different scan rates with a potential window of 0.8 V vs Ag/AgCl. CV tests were performed at scan rates range from 5 mV s^{-1} to 100 mV s^{-1}, electrochemical impedance spectroscopy (EIS) was performed between 0.01 Hz -10 kHz, and charge/discharge tests were performed at current density from 0.5 A/g to 20 A/g.

III.IV Magnetic Field Setup

Since the magnetic field of each coil is non-uniform, the arrangement of the two narrow coils with a large radius r is built parallel to one another and on the same axis with a distance of the same radius size r, so that the magnetic field is uniform in a typical region based on the superimposition of the two fields. Given the Helmholtz arrangement of the pair of coils, the following equation is used to calculate the magnetic field:

$$B = 0.72\mu I\frac{n}{r} \quad (3.1)$$

where B is the magnetic flux density, μ is the magnetic field constant, I is the coil current, n is the number of turns in each coil, and r is the coil radius. In this way, we can get the magnetic field of 0.45 mT, 0.89 mT, and 1.34 mT by setting the power supply current for the Helmholtz coils as shown in Figure 3.2a.

III.V Materials Characterization

Field emission scanning electron microscope (FESEM) (Carl Zeiss Auriga-BU FIB FESEM Microscope) was performed to study the morphological properties of ECNFs/MnO_2. Raman spectroscopy (Horiba XploRA One Raman Confocal Microscope System), x-ray powder diffraction (XRD) (Agilent Technologies Oxford Germini X-Ray Diffractometer), and Fourier transform infrared spectroscopy (FTIR) (Varian 670) were employed to study the elements components of ECNFs/MnO_2. Thermogravimetric analysis (TGA) (SDT Q600) and energy-dispersive X-ray spectroscopy (EDX) (Hitachi S-4800-I FESEM w/Backscattered Detector & EDX) were performed to study the weight ratio of MnO_2 on MnO_2/ECNFs. Superconducting quantum interference device vibrating sample magnetometer (SQUID VSM, Quantum Design, Inc.) was used to measure the magnetic properties of the MnO_2/ECNFs electrodes.

III.VI Calculation and Analysis Method

From the CV curves, the specific capacitance could be calculated on the basis of the following equation:

$$C = \int_{E1}^{E2} i\,dE / 2mS(E2\text{-}E1) \tag{3.2}$$

From the charge/discharge curves, the specific capacitance could be calculated as the following equation:

$$C = It/m(E2\text{-}E1) \tag{3.3}$$

where C is the specific capacitance (F/g), $\int_{E1}^{E2} i\,dE$ is the integrated area in cyclic voltammograms, m is the mass of the active sample (g), S is the scan rate (V/s), and (E2-E1) is the potential window (V), I is the discharge current (A), t is the discharge time in the potential window (s).[1-3]

For an electron transfer at electrode:

$$A + e \longrightarrow D \tag{3.4}$$

Based on molecular basis, transition state theory expresses the electron transfer rate at the equilibrium state as:

$$k = A\exp\left[-\frac{\Delta G_0^{*}}{k_B T}\right] \tag{3.5}$$

where k (s^{-1}) is rate constant, k_B is Boltzmann's constant ($1.3806568 \times 10^{-23}$ J/K), and T is temperature in Kelvin. For an activated redox group,

$$\Delta G_0^* = \Delta H_0^* - T\Delta S_0^* \tag{3.6}$$

$$k_0 = A\exp\left[\frac{\Delta S_0^*}{k_b}\right]\exp\left[-\frac{\Delta H_0^*}{k_b T}\right] \tag{3.7}$$

When a magnetic field applied to the MnO_2 electrode:

entropy: $\Delta S_0^* \longrightarrow \Delta S_0^* + \Delta S_m^*$

enthalpy: $\Delta H_0^* \longrightarrow \Delta H_0^* + \Delta H_m^*$

The rate constant then is expressed as:

$$k_m = A\exp\left[\frac{\Delta S_0^*}{k_b}\right]\exp\left[\frac{\Delta S_m^*}{k_b}\right]\exp\left[-\frac{\Delta H_0^*}{k_b T}\right]\exp\left[-\frac{\Delta H_m^*}{k_b T}\right] \tag{3.8}$$

$$\text{with} \quad \Delta H_m^* = -gHS\beta$$

In Eq. 3.8, the effects of magnetic field are expressed in enthalpy and entropy, and separated from non-magnetic entropy and enthalpy.

To simplify the process, only one of the unpaired electrons in Mn(IV/III) with spin ½ is considered for this derivative regarding the rate constant, scheme 3.1 below illustrates the simplified model for the energetics of the electron transfer/exchange reaction between Mn(IV/III).

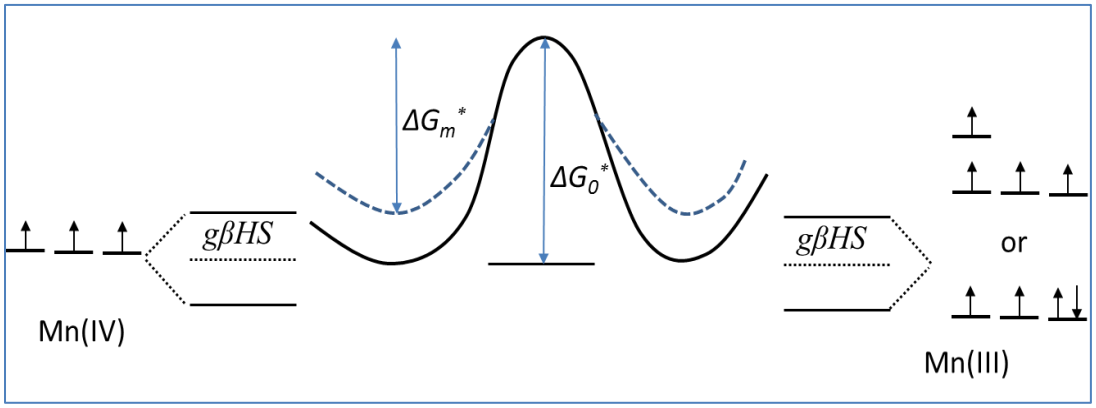

Figure 3.1. Schematic Illustration of a Case at Magnetic Field Effects on the Electron Transfer/exchange Between Mn(IV/III). The gβHS represents the energetic degeneracy of the electron spin S under magnetic field. Two electron configurations (high spin and low spin) of the Mn(III) are illusSStrated.

The ratio of the rate constant change of magnetic field to non-magnetic field is:

$$\frac{k_m}{k_0} = \exp\left[\frac{\Delta S_m^*}{k_b}\right]\exp\left[-\frac{\Delta H_m^*}{k_b T}\right] = \exp\left[\frac{\Delta S_m^*}{k_b}\right]\exp\left[\frac{gHS\beta}{k_b T}\right] \tag{3.9}$$

If $gHS\beta << k_bT$, and $\lim_{x\to 0}\exp[x] \to 1+x$, the Equation 3.9 becomes:

$$\frac{k_m}{k_0} = \left[1+\frac{gHS\beta}{k_b T}\right]\exp\left[\frac{\Delta S_m^*}{k_b}\right] \tag{3.10}$$

The entropy of spin state can be expressed as:

$$\frac{S^*}{k_b} = -\sum_i n_i p_i \ln p_i \tag{3.11}$$

where the n is the number of species (electrons) and each electron has several assessable states and the probability of the species being in a state i is p_i. With sufficient magnetic

field for spin polarization, one unpaired spin only has one state then the entropy term is one; while no magnetic field, the unpaired electron may be present in one of the two states, spin up and spin down. Thus the equation 3.10 can be derived as:

$$\frac{k_m}{k_0} = 2\left[1 + \frac{gHS\beta}{k_b T}\right] \tag{3.12}$$

This equation gives us how the magnetic field induced degeneracy effects on the electron transfer reaction rate constant between Mn(IV/III) at the electrode. The actual case is more complicated because the number of unpaired electrons and spin states involved while also changes with the redox status. However, one can conclude that the magnetic field polarization on unpaired electron spin and the energy degeneracy would facilitate the redox reaction.

III.VII Results and Discussion

The morphologies of ECNFs and MnO_2/ECNFs were characterized by SEM (Figure 3.2b,d). The ECNFs with nanofiber diameter of about 521 nm (Figure 3.2c) are decorated by MnO_2 coating with thickness of ~2.1 μm making a total diameter of the fiber as about 2.63 μm (Figure 3.2e). The charge current of 40 μA, the charge time of 3 hours in an aqueous precursor solution with 10 mM $MnSO_4$ and 100 mM Na_2SO_4 were applied to achieve the electrochemical deposition of the MnO_2 at the 1 cm^2 ECNFs film. The success of MnO_2 deposition was confirmed with Raman spectra (Figure 3.3 Mn-O at the Raman shift of 627 cm^{-1}), XRD pattern (in Figure 3.4, the well resolved peak at 37.1° is attributed to MnO_2), and FTIR spectra (in Figure 3.5 Mn-O stretch is presented at the wavenumber of 648 cm^{-1} and 731 cm^{-1}).[38,39] TGA shows the weight fraction of MnO_2 of the MnO_2/ECNFs electrode is about 53% (Figure 3.6), which was verified using EDX analysis by averaging different spectrum zones (Figure 3.7).

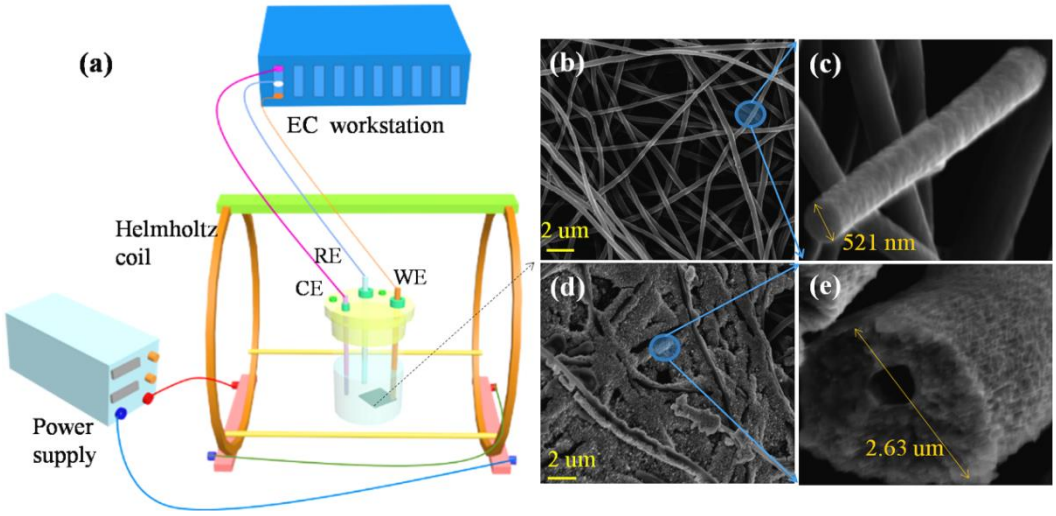

Figure 3.2. (a) The Schematic Illustration of the Electrochemical Cell in the Presence of an External Magnetic Field. (b)-(e) SEM images of the electrode materials (b) ECNFs, (c) enlarged ECNFs, (d) MnO_2/ECNFs, and (e) enlarged MnO_2.

As a pseudocapacitive electrode, the MnO_2/ECNFs electrode possesses combined contribution of spacers and redox reaction, i.e., the electrochemical double layer capacitance and the pseudocapacitance from MnO_2 for energy storage. The former stores charge electrostatically due to the adsorption of ions at electrode surfaces and is mainly determined by the electrode surface area. While, for the latter, the energy is stored in virtue of highly reversible redox reactions (e.g. electron transfer reactions) between Mn(IV)/Mn(III) species and cation intercalation/de-intercalation at the MnO_2/electrolyte interfaces.[36,40,41] The charge storage mechanism of the MnO_2/ECNFs electrode involving the KOH electrolyte can be expressed as[36,40,42]:

$$Mn(IV)O_2 + mH^+ + nK^+ \leftrightarrow Mn(III)Mn(IV)OOH_mK_n \quad (3.13)$$

Equation 3.13 represents the successive multiple surface redox reactions between the Mn(IV)/Mn(III) complexes leading to the pseudo-capacitive charge storage mechanism.[42]

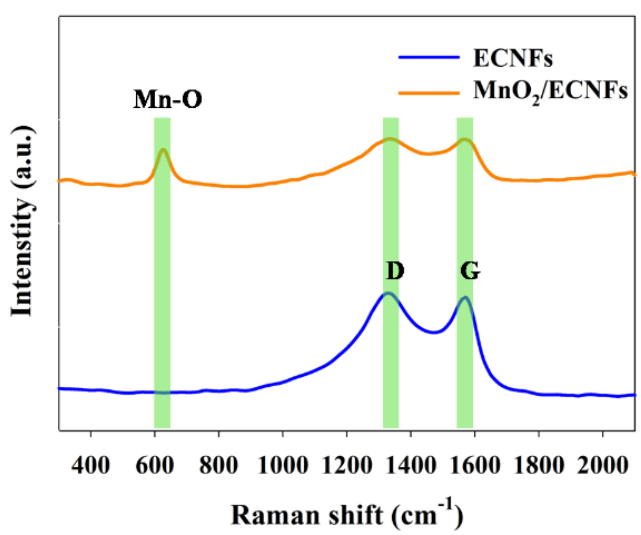

Figure 3.3 Raman Spectra of ECNFs and MnO_2/ ECNFs. At Raman shift of 1328 cm^{-1} and 1572 cm^{-1}. ECNFs shows D-band and G-band, respectively. While, for MnO_2/ECNFs, Mn-O presents at the Raman shift of 627 cm^{-1}.

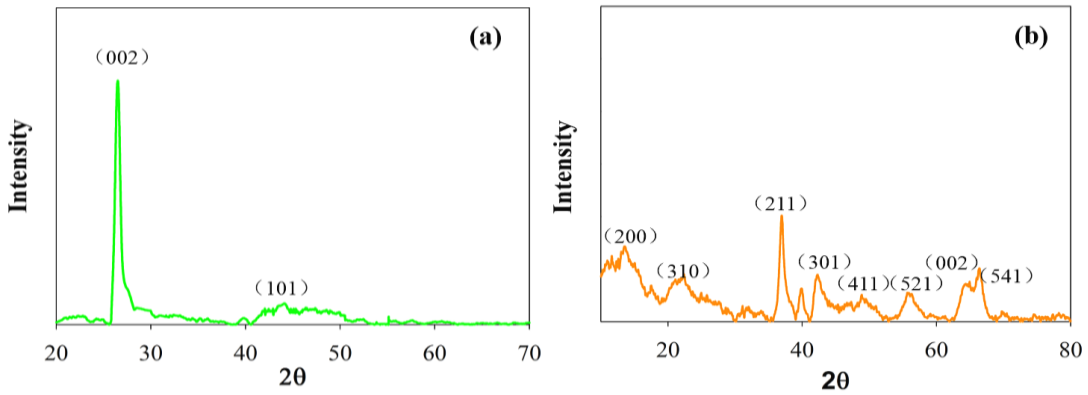

Figure 3.4 XRD Spectra of ECNFs (a) and MnO_2 (b). The well-resolved peak at 37.1° in the XRD pattern is attributed to MnO_2.[5]

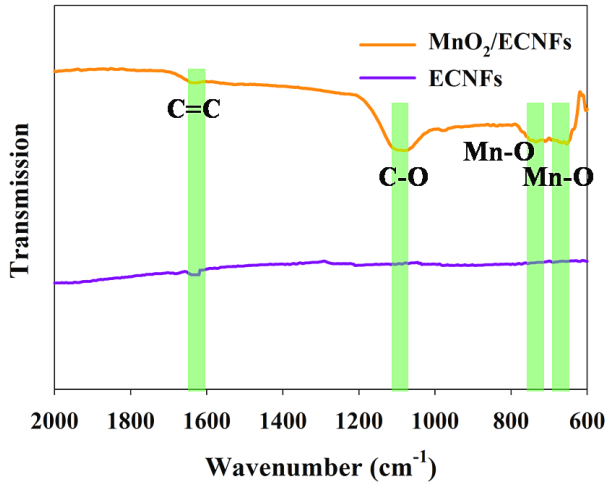

Figure 3.5 FTIR Spectra of ECNFs and MnO_2/ECNFs. At wavenumber of 1623 cm^{-1}, ECNFs shows C=C. While, for MnO_2/ECNFs, Mn-O present at the wavenumber of 648 cm^{-1} and 731 cm^{-1}. C-O presents at the Raman shift of 1104 cm^{-1}.[6]

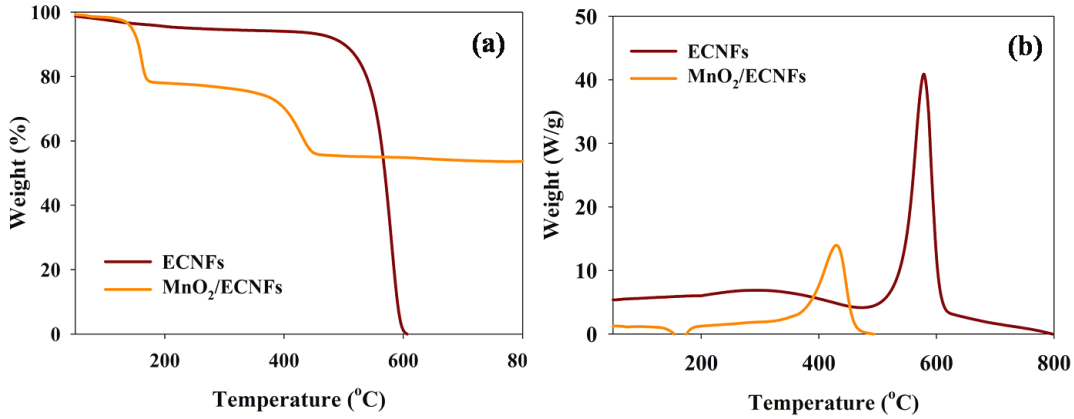

Figure 3.6 TGA and DSC of ECNFs and MnO_2/ECNFs to 800 ˚C in Air. Due to the residue solvent evaporation, the ECNFs shows a weight loss before 431 ˚C. And then ECNFs decomposes until 605 ˚C. Unlike ECNFs, the MNO_2/ECNFs still achieve about 53% after 605 ˚C. So the MnO_2/ECNFs comprise 53% MnO_2 and 47% ECNFs.

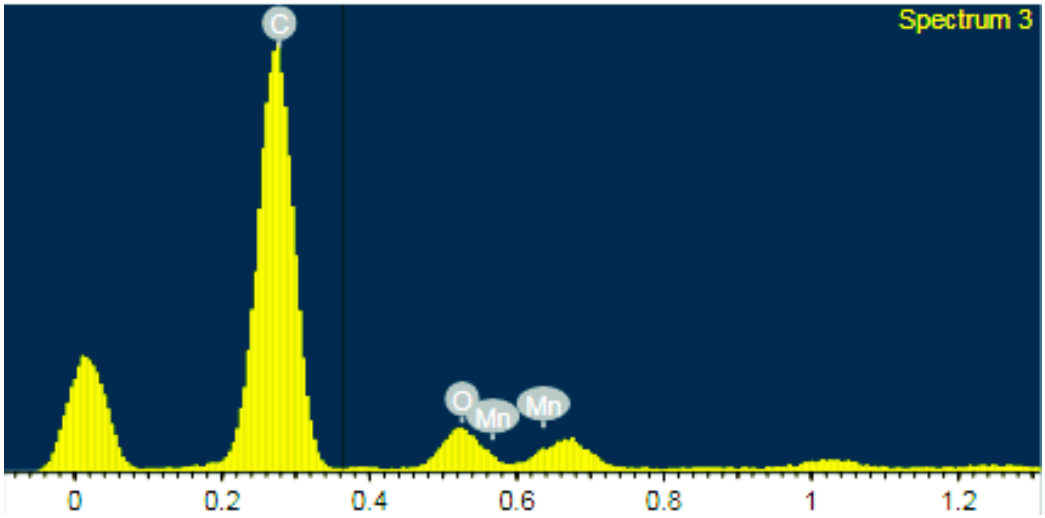

Figure 3.7 EDX of MnO_2/ECNFs. The weight% of C, O and Mn is 56.84%, 15.19%, 27.97% respectively. And the weight ratio of Mn: O is about 2:1. By averaging the EDX results of different spectrum zones, the average weight% of C, O and Mn is about 51.18%, 17.14%, and 31.68% respectively.

To measure the specific capacitance of the MnO_2/ECNFs electrode and magnetic field effect, CV was performed using the classical three-electrode method[43] in 6.0 M KOH electrolyte solution.

Figure 3.8 shows the representative, stable cyclic voltammetry (CV) loops with or without an external magnetic field, which present a combination of both double layer and pseudocapacitive behaviors within the scan voltage from 0.0 V to 0.8 V. There are a pair of peaks at the voltage between 0.4-0.5 V vs. Ag/AgCl which might be attributed to the redox reaction of the Mn(IV)/Mn(III) species in the form of K^+ intercalation.[41] The overall specific capacitance is calculated from the integrated area of the CV loops. In the absence of an external magnetic field, the specific capacitance of a MnO_2/ECNFs electrode was calculated to be 119.2, 105.8, 92.8, 71.0, 53.4 F/g at the voltage sweeping rates of 5, 10, 20, 50, and 100 mV/s, respectively. Compared to that of the ECNFs-only electrode (Figure 3.9a), MnO_2/ECNFs shows higher capacitance because of the higher relative dielectric constant of MnO_2 and its pseudo-activity. In the presence of 1.34 mT magnetic field, the capacitance of the MnO_2/ECNFs magneto-supercapacitor electrode was obtained to be 141.7, 125.9, 110.2, 86.5, 67.0 F/g at the same voltage sweeping rates of 5, 10, 20, 50, and 100 mV/s, respectively, which increased by about avg. 19% for all sweeping rates (Figure 3.8b-d, Figure 3.10). Since there is no measurable enhancement of capacitance of the ECNFs-only electrodes at the same range of voltage sweeping rates (Figure 3.9a-b) under the magnetic field, one can conclude that the magnetocapacitance enhancement of the

MnO_2/ECNFs electrode is resulted from the magnetic field effect on the MnO_2 at the ECNFs substrate.

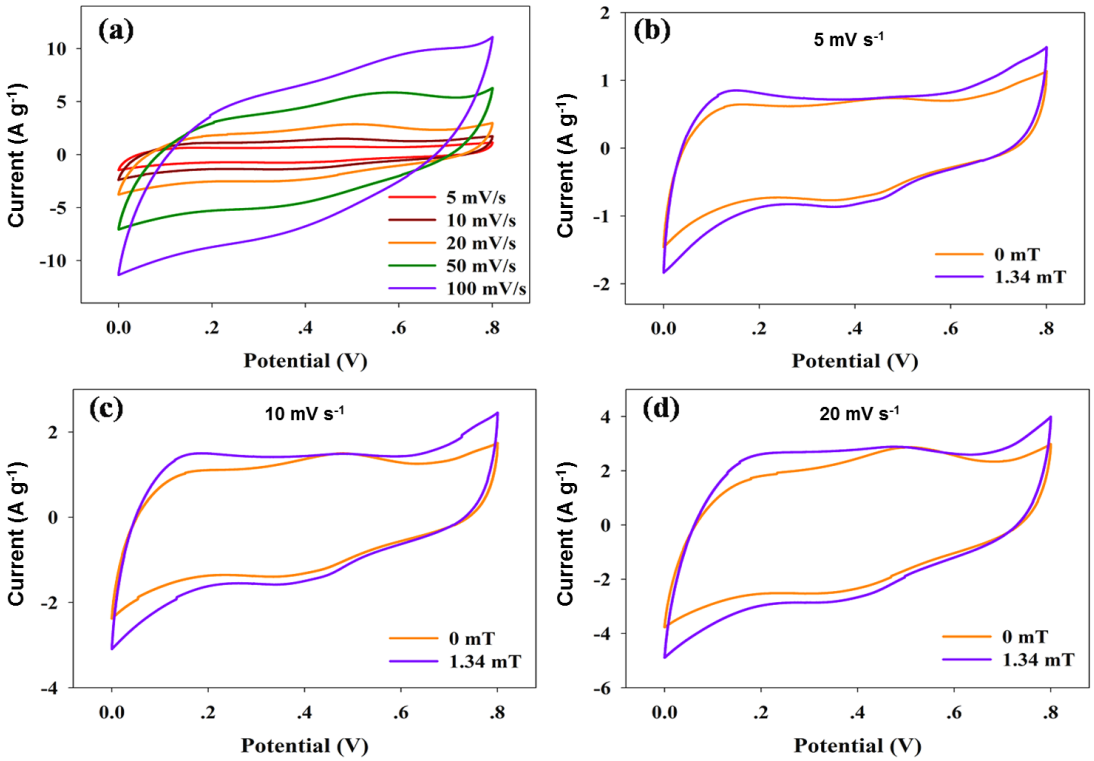

Figure 3.8. (a) Cyclic Voltammetry Loops of the MnO_2/ECNFs Electrodes Tested in the Absence of Magnetic Field (0 mT) at Different Voltage Sweeping Rates. Cyclic voltammetry loops of the MnO_2/ECNFs electrodes tested in the presence (1.34 mT)/ absence (0 mT) of magnetic field at different scan rates of 5 mV/s (b), 10 mV/s (c), 20 mV/s (d).

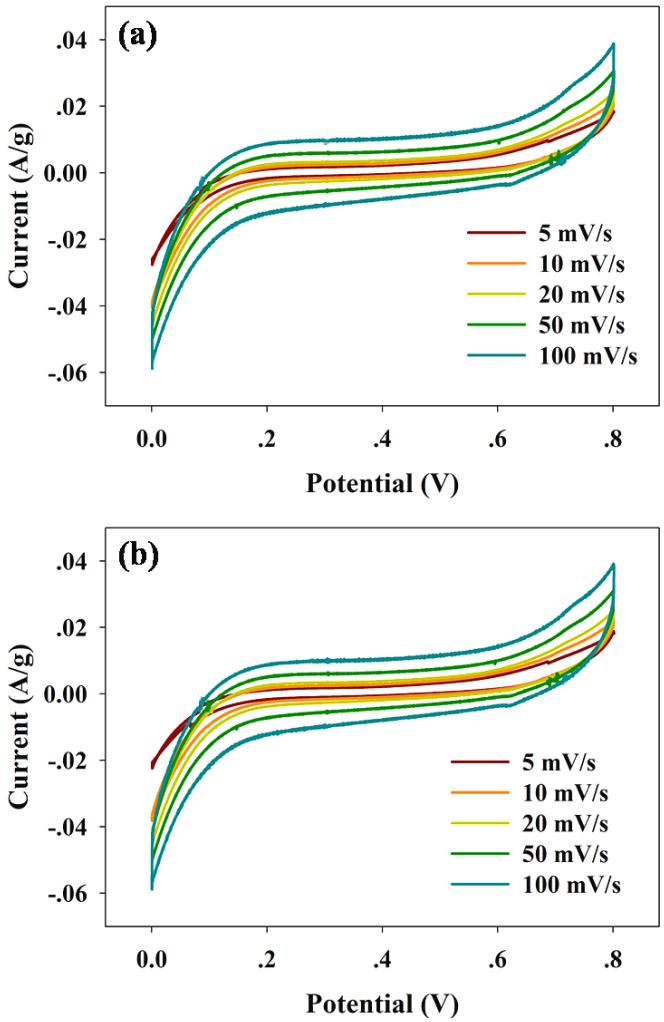

Figure 3.9 (a) Cyclic Voltammetry Loops of the ECNFs Electrodes Tested in the Absence of Magnetic Field (0 mT) at Different Scan Rates. (b) Cyclic voltammetry loops of the ECNFs electrodes tested in the presence of magnetic field (1.34 mT) at different scan rates.

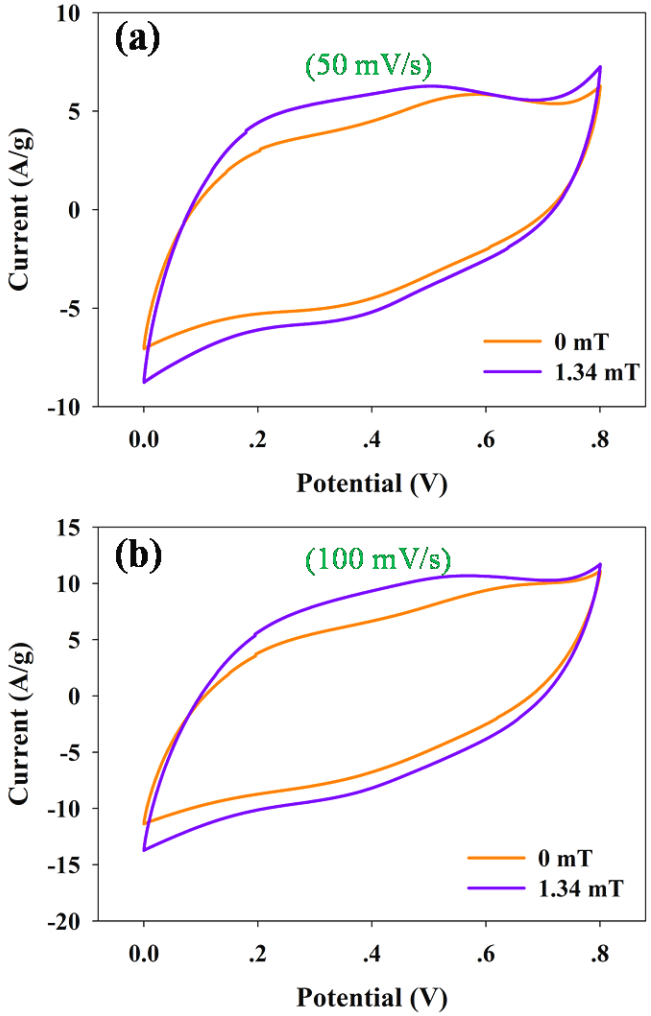

Figure 3.10 Cyclic Voltammetry Loops of the MnO_2/ECNFs Electrodes Tested in the Presence (1.34 mT) / absence (0 mT) of Magnetic Field at Different Scan Rates of 50 mV/s (a) and 100 mV/s (b).

The effect of magnetization on the galvanostatic charge/discharge performance of MnO_2/ECNFs was studied under different current densities (0.5-20 A/g, Figure 3.11a-c & Figure 3.12). The curvature of the charge step between the voltage of 0.0-0.4 V and larger growth of the discharge curve between the same range voltages suggest a combined contribution from pseudocapacitance and double layer capacitance,[44] which is consistent

with the observation from CV studies. With the applied magnetic field from 0.45 mT to 1.34 mT and the same current density, the charge/discharge time increases (Figure 3.11b-c, Figure 3.12) comparing to that of the absence of magnetic field. The charge/discharge time under smaller current density increases more significantly than that of the larger current density (e.g. 58.1% increase at 0.5 A/g vs. 13.6% at 1 A/g with 1.34 mT magnetic field), suggesting the magnetic field effects on both the pseudocapacitive electrolyte-electrode interface and double layer region, resulting in the magneto-capacitance enhancement.

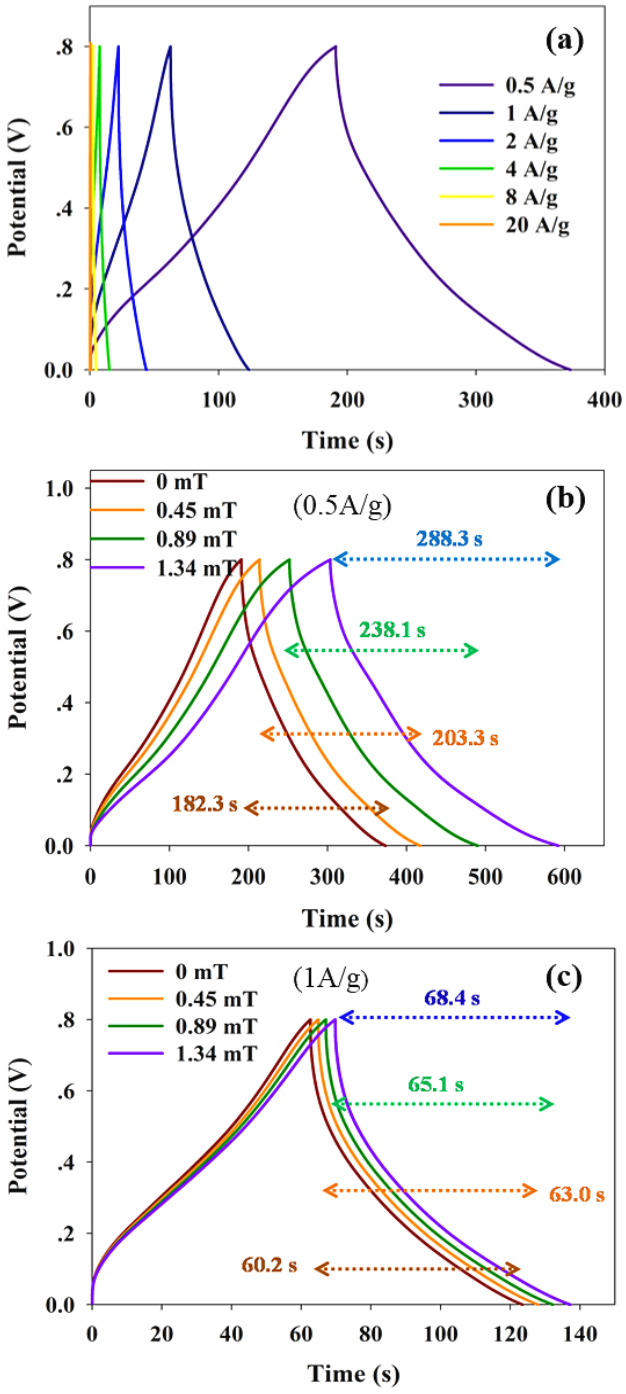

Figure 3.11. (a) Galvanostatic Charge/discharge Curves of the MnO_2/ECNFs Electrodes Tested in the Absence of Magnetic Field Under Different Current Densities. Galvanostatic charge/discharge curves of the MnO_2/ECNFs tested in the presence of different magnetic fields under different current densities of 0.5 A/g (b), and 1 A/g (c).

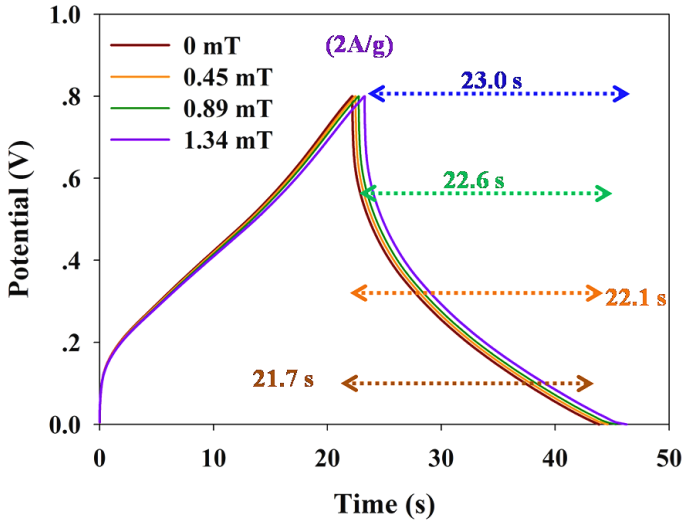

Figure 3.12 Galvanostatic Charge/discharge Curves of the MnO_2/ECNFs Tested in the Presence of Different Magnetic Fields Under the Current Density of 2 A/g.

From the charge/discharge curves, specific capacitance is calculated from the discharge curves,[45] i.e., $C = I \cdot t/(m \cdot \Delta E)$, in which I is the discharge current, t is the discharge time, and ΔE is the potential drop during discharge in V. It was found that, under the magnetic field of 1.34 mT, the electrode of MnO_2/ECNFs enhanced the capacitance by 58.1% (Figure 3.11b) at the current density of 0.5 A/g, by 13.6% under the current 1 A/g (Figure 3.11c) and 6% under 2 A/g (Figure 3.12), respectively. Moreover, to quantitatively analyze the pseudocapacitance contribution to the overall capacitance performance, the non-faradaic contribution from double layer capacitance and the faradaic contribution from pseudocapacitance were separated in galvanostatic charge-discharge curves.[44,46] By considering the area corresponding to faradaic contribution in MnO_2/ECNFs electrode, at current density of 0.5 A/g, the pseudocapacitance contribution from MnO_2 in overall

performance was approximately 56.5%, 61.0%, 62.4%, and 67.8% with the applied magnetic field of 0 mT, 0.45 mT, 0.89 mT, and 1.34 mT, respectively. The fraction of the pseudocapacitive contribution in energy storage increases along with the magnetic field strength, suggesting the more significant effect on pseudo-redox reaction at the MnO_2/ECNFs electrode than that on the non-faradaic contribution.

Next, the effect of magnetic field on the impedance of the MnO_2/ECNFs within the electrochemical cell (6 M KOH electrolyte) was investigated using EIS, which may provide understanding of the different electrochemical behaviors in the absence/presence of magnetic field. Figure 3.13 shows the performance of EIS for the MnO_2/ECNFs electrodes over the frequency range of 10 kHz to 0.01 Hz with the potential amplitude of 10 mV. Both the Nyquist plots of EIS spectra in the absence/presence of an external magnetic field show a semicircle arc in the high frequency region and a linear line in the low frequency region, indicating a low internal resistance of the MnO_2/ECNFs electrodes.[47] In the presence of 1.34 mT magnetic field, the capacitor system superficially seems to be a more ideal double layer supercapacitor, since the semicircle arc is more obvious and straight line seems to be little more vertical. Zhu, et al.[33,47] reported that additional Lorentz force acts on the moving ions in a perpendicular magnetic field flux density (magnetohydrodynamic phenomenon), which may promote the electrolyte convection in the bulk electrolyte. Hence, it is not surprising that the changes of the solution resistance (R_s ~1 Ohms) in bulky electrolyte, the charge transfer resistance (R_{ct}) at the electrode-electrolyte interface, and the

leakage resistance (R_{leak}) of the double layer region at low frequency are observed for MnO_2/ECNFs electrodes under magnetic field. Specifically, the solution resistance (Rs) with 1.34 mT magnetic field decreases about 0.1 Ohms from 1 Ohms. The resistance of charge transfer (R_{ct}) of the electrode reaction obtained from the diameter of the semicircle in the high frequency region (1.26 Ohms) decreased from 1.35 Ohms of the non-magnetized MnO_2/ECNFs electrode, indicating a faster contact and charge transfer which may result in an improved rate performance.[48] The low frequency leakage resistance (R_{leak})[34] in the double layer region increased for the MnO_2/ECNFs electrode with the presence of magnetic field, suggesting that leakage current flowing across the double layer at the electrode-electrolyte interface was better restricted, which may also improve the MnO_2/ECNFs electrode capacitance.

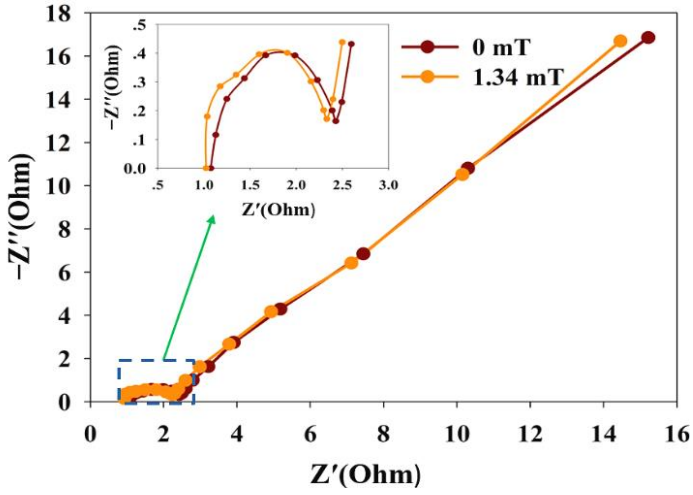

Figure 3.13. Nyquist Plots of the MnO_2/ECNFs Electrodes Tested in the Presence (1.34 mT) / absence (0 mT) of Magnetic Field.

The EIS analysis of this work agrees with the previous studies by Zhu, et al[33,47] on different metal oxide (Fe, Ni, Co)-carbon supercapacitors. The magnetohydrodynamic phenomenon is the major factor for the electrode internal resistance decrease and the magnetic induced electrolyte convection to reach extra electrode surfaces, which may help to generate larger specific capacitance of the electrodes, and build up a complete double layer that restricts the leakage of free electrons, thus improving the capacitance performance. However, in this study, much smaller magnetic field strength, i.e. 1.34 mT on MnO_2/ECNFs electrode and much smaller resistance change, achieved comparable capacitance enhancement of 72 mT magnetic field on metal-oxide (Fe, Ni, Co) nanocomposite electrodes.[33,47] It is known that MnO_2 has the paramagnetic property due to multiple unpaired electrons involving in the pseudo-active electron transfer reaction. Hence it may help to better understand the capacitance enhancement by measuring the

magnetization of the MnO_2/ECNFs electrodes. The magnetic susceptibility of the MnO_2/ECNFs was performed using the SQUID VSM at room temperature and Figure 3.14 shows the moment response of the MnO_2/ECNFs electrode under different magnetic field strength.

The magnetization, measured as the magnetic moment associated with electron's spin state, $\mu_{e,}$ at 1.34 mT magnetic field is found to be 4.23×10^{-4} emu/g of the MnO_2/ECNFs electrode and ~7.98×10^{-4} emu/g of the pure MnO_2 mass fraction (ca. 53%) in the electrode. The spin-dependent torque the MnO_2 experienced, representing the improved energy state of the electron, is 1.07×10^{-9} J/g (~93.0×10^{-9} J/mol) obtained by multiplying the magnetic field by the magnetic moment. The magnetic field induced spin-dependent torque on an electron with spin quantum number m_s=+1/2 and -1/2 causes the degeneracy, namely different energy levels of the "+" and "-" spin states,[49] which is expressed as, $h\nu=g\beta H$ where $h\nu$ is the quantum of energy corresponding to a characteristic frequency ν, g is dimensionless constant called the "electron g-factor", β is the electronic Bohr magneton (9.2740154×10^{-24} J T^{-1}), and H is the magnetic field strength. The enhanced energy state of the electrons will increase the electron transfer kinetics between the species of Mn(IV)/Mn(III), as well as the electron transportation efficiency at the electrolyte-MnO_2/ECNTs interfaces, hence contributes to the capacitance enhancement.

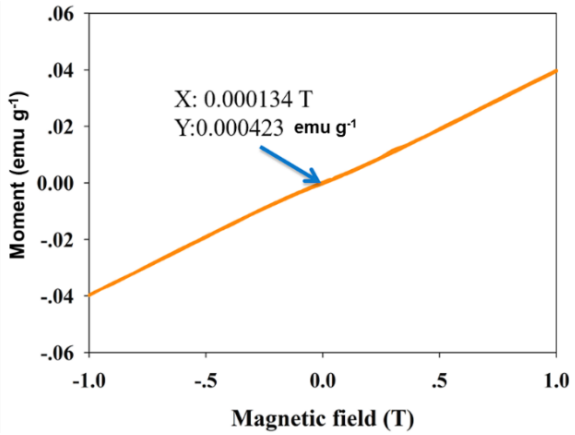

Figure 3.14. SQUID VSM Result of MnO_2/ECNFs at Room Temperature. The closely straight line shows the magnetization of MnO_2/ECNFs is 4.23×10^{-4} emu/g at 1.34 mT magnetic field. Since the weight ratio of MnO_2 in MnO_2/ECNFs is about 53%, the magnetization on pure MnO_2 is calculated to be 7.98×10^{-4} emu/g.

The magnetic field effect on the redox electron transfer kinetics of Mn(IV)/Mn(III) is further analyzed according to transition state theory by considering the contribution of the enhanced electron energy states to the activation energy due to magnetic field induced degeneracy. The rise of Zeeman energy, gβHS (S is spin), relative to the reactant energy when there is no applied field, of the unpaired electrons in MnO_2 with magnetic field contributes to the activation energy by reducing the net enthalpy of activation barrier and thus the reaction rate is facilitated. The redox electron transfer rate of Mn(IV)/Mn(III) at the electrode can be expressed in an Arrhenius form as :

$$k_m = A\exp\left[\frac{\Delta S_0^*}{k_b}\right]\exp\left[\frac{\Delta S_m^*}{k_b}\right]\exp\left[-\frac{\Delta H_0^*}{k_bT}\right]\exp\left[-\frac{\Delta H_m^*}{k_bT}\right] \qquad (3.14)$$

with $\Delta H_m^* = -gHS\beta$, A is the pre-factor depending on the convolution of a suitable weighted frequency (v_n) for crossing the activation barrier and the transmission coefficient or averaged transition probability for electron transfer per passage of the system through the intersection region from reactant to product, and in classical transition theory, A is taken as k_bT/h where k_b is Boltzmann's constant, T is absolute temperature, and h is Planck constant. With sufficient magnetic field for the energy degeneracy of single unpaired electron spin, the electron transfer rate can be doubled . The measured magnetic susceptibility response to the external magnetic field suggests that the MnO_2/ECNTs electrode is sensitive to magnetic field due to the multiple unpaired electron spins of MnO_2. While it is difficult to quantitatively analyze how the field impact the electron transfer in the electrode, these analyses suggest that the facilitated electron transfer kinetics of the pseudo-redox reaction in the MnO_2/ECNFs electrode contribute significantly in the energy storage performance with respect to the small magnetic field applied to the electrode.

Building upon the results and analysis, one can find that the mT magnetic field significantly enhances energy storage capacitance of the MnO_2/ECNFs electrodes with a comprehensive mechanism due to the combined contribution of both the double layer and pseudo-active capacitance. Firstly, the change of the electrode resistance in electrochemical cell, though small, indicate that the changes of dipole moment in the transition and vibrational states of electrolyte at the double layer area can enhance the conductivity and reduce the resistance (impedance effect), thus enhancing the electrochemical

adsorption/desorption of cations and anions at the electrode/electrolyte interfaces; Secondly, and more significantly in this case, the paramagnetic nature of the MnO_2 with multiple unpaired electrons and magnetic susceptibility may largely facilitate the Mn(IV)/Mn(III) pseudo-redox reaction and electron transfer to the electrolyte-electrode interfaces, which may result in higher charge density at the electrode interfaces, more efficiency of cation intercalation/de-intercalation, and thicker double layer, therefore the enhanced capacitance. Since both the impedance effect and the electron spin energy degeneracy depend on the strength of the magnetic field, the dissimilarity of the magneto-capacitance enhancement at different magnetic field during charge and discharge process is expected.

Finally, for practical purpose, the lifecycle performance of the MnO_2/ECNFs electrodes was performed by galvanostatic charge/discharge cycling in term of two important parts, i.e., cycling capability or capacitance retention, and total discharge time. As shown in Figure 3.15, in the absence of 1.34 mT magnetic field, 92.3% of the initial capacitance was maintained after 1000 cycles. With presence of 1.34 mT magnetic field, 90.6% of the initial capacitance was maintained after 1000 cycles. Note that with the same cycling, the total discharge time increased by 15.1% with presence of magnetic field (Figure 3.15 inserted) due to magnetic field induced discharge time extension.

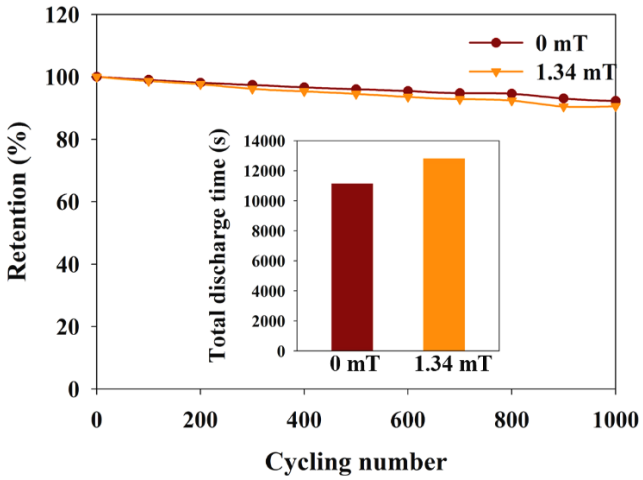

Figure 3.15. Cycling Performance of the MnO_2/ECNFs Electrodes Tested in the Presence (1.34 mT)/ absence (0 mT) of Magnetic Field Under the Current Density of 4 A/g.

Experimental performance and data analysis indicate that the magnetic susceptibility largely increases the charge transfer rate thus improves the pseudo-reactions of MnO_2 at the electrode and interfaces. A supercapacitor nanocomposite electrode composed of MnO_2 deposition on ECNFs exhibits significantly enhanced galvanostatic charge/discharge cycling at a 1.34 mT of magnetic field even under a high current density of 4 A/g, suggesting that the enhanced magneto-supercapacitive performance is mainly attributed to magnetic susceptibility of the MnO_2 in the electrode because of the improvement of the pseudocapacitive behavior at the electrode and the electrode/electrolyte interfaces.

III.VIII Discussion and Conclusion

In summary, after applying 1.34 mT magnetic field, MnO_2/ECNFs showed enhanced magneto-capacitance of 141.7 F/g at the cyclic voltage sweeping rates of 5 mV/s. The capacitance of MnO_2/ECNFs was increased by 58.1% at the current density of 0.5 A/g during the galvanostatic charge/discharge test. Meanwhile, in the presence of 1.34 mT magnetic field, the magneto-supercapacitor presented "low resistance shift" for bulk electrolyte and the MnO_2/ECNFs electrode. Longer charge/discharge time of the electrode is observed under magnetic field than that without magnetic field, while did not sacrifice its lifecycle stability. The insightful discussion of the potential mechanism suggests that the magneto-supercapacitance enhancement can be primarily attributed to the magnetic susceptibility of MnO_2 induced electron spin energy degeneracy for facilitated electron transfer reaction, the magnetohydrodynamic impact on electrolyte transportation and improved cation intercalation/de-intercalation under the mT magnetic field, thus resulting in higher charge density at the electrode/electrolyte interfaces, thicker double layer, and lower internal resistance. This study may pave a way to the development of sustainable metal oxide-based supercapacitors with magneto-capacitance enhancement by applying a low magnetic field.

III.IX References

[1] Choi, N.-S.; Chen, Z.; Freunberger, S. A.; Ji, X.; Sun, Y.-K.; Amine, K.; Yushin, G.; Nazar, L. F.; Cho, J.; Bruce, P. G. Angewandte Chemie International Edition **2012,** 51, (40), 9994-10024.

[2] Miller, J. R.; Outlaw, R. A.; Holloway, B. C. Science **2010,** 329, (5999), 1637.

[3] Itoi, H.; Nishihara, H.; Kogure, T.; Kyotani, T. Journal of the American Chemical Society **2011,** 133, (5), 1165-1167.

[4] Yu, G.; Hu, L.; Vosgueritchian, M.; Wang, H.; Xie, X.; McDonough, J. R.; Cui, X.; Cui, Y.; Bao, Z. Nano Letters **2011,** 11, (7), 2905-2911.

[5] Chun, S.-E.; Evanko, B.; Wang, X.; Vonlanthen, D.; Ji, X.; Stucky, G. D.; Boettcher, S. W. Nature Communications **2015,** 6, 7818.

[6] Choi, H.-J.; Jung, S.-M.; Seo, J.-M.; Chang, D. W.; Dai, L.; Baek, J.-B. Nano Energy **2012,** 1, (4), 534-551.

[7] Lian, C.; Liu, K.; Van Aken, K. L.; Gogotsi, Y.; Wesolowski, D. J.; Liu, H. L.; Jiang, D. E.; Wu, J. Z. ACS Energy Letters **2016,** 1, (1), 21-26.

[8] Wang, W.; Guo, S.; Lee, I.; Ahmed, K.; Zhong, J.; Favors, Z.; Zaera, F.; Ozkan, M.; Ozkan, C. S. Scientific Reports **2014,** 4, 4452.

[9] Jiang, Y.; Ling, X.; Jiao, Z.; Li, L.; Ma, Q.; Wu, M.; Chu, Y.; Zhao, B. Electrochimica Acta **2015,** 153, 246-253.

[10] Jiang, Y.; Wang, P.; Zang, X.; Yang, Y.; Kozinda, A.; Lin, L. Nano Letters **2013,** 13, (8), 3524-3530.

[11] Kumar, R.; Kim, H.-J.; Park, S.; Srivastava, A.; Oh, I.-K. Carbon **2014,** 79, 192-202.

[12] An, G.-H.; Ahn, H.-J. Carbon **2013,** 65, 87-96.

[13] Kim, C. H.; Kim, B.-H. Journal of Power Sources **2015,** 274, 512-520.

[14] Kim, B.-H.; Yang, K. S.; Yang, D. J. Electrochimica Acta **2013,** 109, 859-865.

[15] Zhi, M.; Xiang, C.; Li, J.; Li, M.; Wu, N. Nanoscale **2013,** 5, (1), 72-88.

[16] Yang, P.; Chen, Y.; Yu, X.; Qiang, P.; Wang, K.; Cai, X.; Tan, S.; Liu, P.; Song, J.; Mai, W. Nano Energy **2014,** 10, 108-116.

[17] Zhang, G.; Lou, X. W. D. Scientific reports **2013,** 3, 1470.

[18] Yu, X.; Lu, B.; Xu, Z. Advanced Materials **2014,** 26, (7), 1044-1051.

[19] Peng, L.; Peng, X.; Liu, B.; Wu, C.; Xie, Y.; Yu, G. Nano Letters **2013,** 13, (5), 2151-2157.

[20] Liu, Y.; Zeng, Z.; Wei, J. Front. Nanosci. Nanotech. **2016,** 2, (2), 78-85.

[21] Huang, Z.-M.; Zhang, Y. Z.; Kotaki, M.; Ramakrishna, S. Composites Science and Technology **2003,** 63, (15), 2223-2253.

[22] Zhang, L.; Aboagye, A.; Kelkar, A.; Lai, C.; Fong, H. Journal of Materials Science **2014,** 49, (2), 463-480.

[23] Tõnurist, K.; Jänes, A.; Thomberg, T.; Kurig, H.; Lust, E. Journal of The Electrochemical Society **2009,** 156, (4), A334-A342.

[24] Tõnurist, K.; Thomberg, T.; Jänes, A.; Kink, I.; Lust, E. Electrochemistry Communications **2012,** 22, 77-80.

[25] Tõnurist, K.; Thomberg, T.; Jänes, A.; Romann, T.; Sammelselg, V.; Lust, E. Journal of Electroanalytical Chemistry **2013,** 689, 8-20.

[26] Yang, C.; Jia, Z.; Guan, Z.; Wang, L. Journal of Power Sources **2009,** 189, (1), 716-720.

[27] Janakiraman, S.; Surendran, A.; Ghosh, S.; Anandhan, S.; Venimadhav, A. Solid State Ionics **2016,** 292, 130-135.

[28] Hao, J.; Lei, G.; Li, Z.; Wu, L.; Xiao, Q.; Wang, L. Journal of Membrane Science **2013,** 428, 11-16.

[29] Yanilmaz, M.; Lu, Y.; Zhu, J.; Zhang, X. Journal of Power Sources **2016,** 313, 205-212.

[30] Tõnurist, K.; Vaas, I.; Thomberg, T.; Jänes, A.; Kurig, H.; Romann, T.; Lust, E. Electrochimica Acta **2014,** 119, 72-77.

[31] Ye, W.; Amar, B.; Ruyan, G. Materials Research Express **2016,** 3, (3), 036102.

[32] Bund, A.; Koehler, S.; Kuehnlein, H. H.; Plieth, W. Electrochimica Acta **2003,** 49, (1), 147-152.

[33] Zhu, J.; Chen, M.; Qu, H.; Luo, Z.; Wu, S.; Colorado, H. A.; Wei, S.; Guo, Z. Energy & Environmental Science **2013,** 6, (1), 194-204.

[34] Wang, G.; Xu, H.; Lu, L.; Zhao, H. Journal of Energy Chemistry **2014,** 23, (6), 809-815.

[35] Wu, Q.; Chen, M.; Chen, K.; Wang, S.; Wang, C.; Diao, G. Journal of Materials Science **2016,** 51, (3), 1572-1580.

[36] Toupin, M.; Brousse, T.; Bélanger, D. Chemistry of Materials **2004,** 16, (16), 3184-3190.

[37] Wang, Y.; Song, Y.; Xia, Y. Chemical Society Reviews **2016,** 45, (21), 5925-5950.

[38] Wang, T.; Song, D.; Zhao, H.; Chen, J.; Zhao, C.; Chen, L.; Chen, W.; Zhou, J.; Xie, E. Journal of Power Sources **2015,** 274, 709-717.

[39] Dubal, D. P.; Dhawale, D. S.; Salunkhe, R. R.; Lokhande, C. D. Journal of The Electrochemical Society **2010,** 157, (7), A812-A817.

[40] Pang, X.-F.; Deng, B. Physica B: Condensed Matter **2008,** 403, (19–20), 3571-3577.

[41] Mai, L.; Li, H.; Zhao, Y.; Xu, L.; Xu, X.; Luo, Y.; Zhang, Z.; Ke, W.; Niu, C.; Zhang, Q. Scientific Reports **2013,** 3, 1718.

[42] Simon, P.; Gogotsi, Y. Nat Mater **2008,** 7, (11), 845-854.

[43] Liu, Y.; Dolidze, T. D.; Singhal, S.; Khoshtariya, D. E.; Wei, J. The Journal of Physical Chemistry C **2015,** 119, (27), 14900-14910.

[44] Chen, S.; Zhu, J.; Wu, X.; Han, Q.; Wang, X. ACS Nano **2010,** 4, (5), 2822-2830.

[45] Zang, J.; Li, X. Journal of Materials Chemistry **2011,** 21, (29), 10965-10969.

[46] Tian, W.; Gao, Q.; Qian, W. ACS Sustainable Chemistry & Engineering **2016**.

[47] Zhu, J.; Chen, M.; Wei, H.; Yerra, N.; Haldolaarachchige, N.; Luo, Z.; Young, D. P.; Ho, T. C.; Wei, S.; Guo, Z. Nano Energy **2014,** 6, 180-192.

[48] Singh, R. K.; Devivaraprasad, R.; Kar, T.; Chakraborty, A.; Neergat, M. Journal of The Electrochemical Society **2015,** 162, (6), F489-F498.

[49] Eremin, I.; Chubukov, A. V. Physical Review B **2010,** 81, (2), 024511.

CHAPTER IV

SELF-SUSTAINABLE SEPARATOR-FREE CONFIGURATION FOR A METAL-OXIDE FILM SUPERCAPACITOR

This chapter has been submitted as: **Y. Liu**, Z. Zeng, J. Wei*, Self-sustainable separator-free configuration for a metal-oxide film supercapacitor. *ACS Applied Materials & Interfaces*, **2017**, Submitted.

IV.I Introduction

Supercapacitors have been studied for decades and considered as one of the most promising energy storage systems.[1-3] Electric double layer capacitance (EDLC) capacitors utilize carbon or derivatives as electrode followed with activation treatment to introduce pores and increase the specific surface area (SSA).[4-7] Pseudocapacitance comes from the desolvated-adsorbed ions when active materials (usually transition metal oxides) are deposited onto EDLC electrodes, showing higher capacitance compared to EDLC.[8] Manganese dioxide (MnO_2) is demonstrated to be one of the most promising electrode materials for high pseudocapacitance,[9-13] magneto property,[14] ecofriendly, and low cost.[15] However, unstable MnO_2 loading inhibits the overall performance of a cell since the mass ratio of MnO_2/cell is very small. Researchers have tried to enhance the whole cell performance by increasing the mass concentration of MnO_2 in the cell.[16-18] Some studies offered solutions toward commercial level of the mass loading,[19] however,

the accumulation of MnO_2 will suffer from its low proton diffusion constant ($\sim 10^{-13}$ $cm^2/(V\ s)$) and low electrical conductivity ($\sim 10^{-5}$ S/cm) which can lower their galvanic charge-discharge efficiency.[20-22] A separator between two electrodes is a critical component in both lithium-ion batteries and supercapacitors. Its function is to apply high resistance between two electrodes while allowing free ions to flow. They usually are polymeric membrane or non-woven fabric mat with thicknesses ranging from 25 μm to 200 μm.[23-26] However the thicknesses of a typical supercapacitor electrode from leading studies range from 100 nm to 120 μm,[27,28] indicating that too much space (9.6 % to 50 %) inside the cells was taken by the separator (Figure S1), which adversely affects their energy storage performance. Therefore, we propose to utilize the electronic resistance of massive MnO_2 film loading to function as a separator while introducing high pseudocapacitance energy storage to the system.

In this work, a separator-free configuration in which ultra-thick MnO_2 layers functions as both the pseudo-material and separator was presented. This novel design may save the space of a separator and simplify the assembly procedure in the supercapacitor assembling. SA-ECNFs were synthesized by a facial electrospinning setup with alignment (Figure S2). Different deposition settings were applied to explore their separator-functioning capability by electrodepositing uniform ultra-thick crystalline α-MnO_2 layers (around 200 nm ~ 2000 nm) onto SA-ECNFs as the cathode of the asymmetrical cell.

IV.II Electrospun of SA-ECNFs

The fabrication technique for the super-aligned ECNFs is based on a facile electrospinning method with a self-designed sample collector. Different from a normal cylinder design, four steel poles were welded on a plate in order to collect the ECNFs without any substrates. In details, 10 wt.% polyacrylonitrile (PAN, Mw = 150,000, Aldrich) solution in dimethylformamide was electrospun onto a fast rolling (2000 revolutions per minute) collector to form a SA-ECNFs fabric. The obtained sheet was stabilizing with a heat rate of 1 °C/min from 20 °C to 280 °C in air flow, the temperature was kept for 6 h and then cooled down. The carbonization was controlled at a rate of 5 °C/min from 20 °C to 1200 °C in N_2 atmosphere, then it was maintained for 1 h before cooled down to room temperature.

IV.III MnO_2 Electrodeposition on SA-ECNFs

The SA-ECNFs were cut into 2×1 cm^2 SA-ECNFs then half dipped in the electrolyte to electrodeposite MnO_2 by a galvanostatic method with a three-electrode setup using charging currents from 20 μA to 80 μA. Here, a gold electrode attached with SA-ECNFs, platinum electrode, and Ag/AgCl were used as working electrode, counter electrode, and reference electrode, respectively. To assure that the deposition of MnO_2 took place uniformly and firmly at the SA-ECNFs' surfaces, the SA-ECNFs electrode was treated with 4 M HNO_3 solution at 70 °C for 2 h to introduce –OH and –COOH groups to

facilitate the deposition. The depositions were protected in an inert N_2 atmosphere with an aqueous solution containing 50 mM $MnSO_4$ and 100 mM Na_2SO_4 as supporting electrolyte. After the deposition, the working electrodes were washed with deionized water and then dried at 80 °C for 2 h.

IV.IV Materials Characterization

Field emission scanning electron microscope (FESEM) (Carl Zeiss Auriga-BU FIB FESEM Microscope) was performed to study the morphological properties of MnO_2/SA-ECNFs. X-ray powder diffraction (XRD) (Agilent Technologies Oxford Germini X-Ray Diffractometer) was employed to study the crystal structures of MnO_2/SA-ECNFs (Cu Kα radiation: wavelength 0.15418 nm) operating at 40 kV and 40 mA; the step is 0.02, and the speed is 1 deg min^{-1}). Energy-dispersive X-ray spectroscopy (EDX) (Hitachi S-4800-I FESEM w/Backscattered Detector & EDX) was performed to study the atomic ratio on MnO_2/SA-ECNFs. X-ray photoelectron spectroscopy (XPS, Thermo Fisher ESCALAB 250 Xi) was used to determine the elemental composition of MnO_2/SA-ECNFs.

IV.V Electrochemical Measurements

Electrochemical performance of the as-prepared electrodes was performed on a bio-logic® VMP3 electrochemical workstation using two types of setup. Three-electrode system with MnO_2/SA-ECNFs as the working electrode, a platinum electrode as the

counter-electrode and Ag/AgCl as the reference electrode was used in cyclic voltammetry (CV) tests in a 6 M KOH electrolyte solution; Two-electrode asymmetrical system with MnO_2/SA-ECNFs as the cathode, carbon nanotubes (CNT) paper as the anode in a standard testing platform (provided by colleagues for supercapacitor testing[30,32]) consists of two stainless plates, rubber O-ring, insulator (3M vinyl electrical tape), with /without membrane filter separator (MF-Millipore, cellulose, 0.22 micron pore size) and steel holder was used in electrochemical impedance spectroscopy (EIS) and galvanostatic charge/discharge tests in a 6 M KOH electrolyte solution. The voltammetry was scanned from a potential of 0.0 V to 0.8 V vs Ag/AgCl at different scan rates (5 mV/s – 50 mV/s), EIS was performed from 100 kHz to 0.01 Hz, and galvanic charge/discharge tests were performed at different current densities (2.5 A/g to 10 A/g).

IV.VI Calculation Section

From the charge/discharge curves, the specific capacitance was calculated using the following equation:

$$C = \frac{It}{m(E_2 - E_1)} \qquad (4.1)$$

where C is the specific capacitance (F/g), m is the mass of the MnO_2 (g), (E_2-E_1) is the potential window (V), I is the discharge current (A), and t is the discharge time in the potential window (s).

The energy density (D_e) of the capacitors was calculated using the following equation:

$$D_e = C(E_2 - E_1)^2 / 2 \qquad (4.2)$$

where C is the specific capacitance (F/g), m is the mass of the MnO_2 (g), (E_2-E_1) is the potential window (V). Specific capacitance and specific energy density were calculated based on the mass of active material.

IV.VII Results

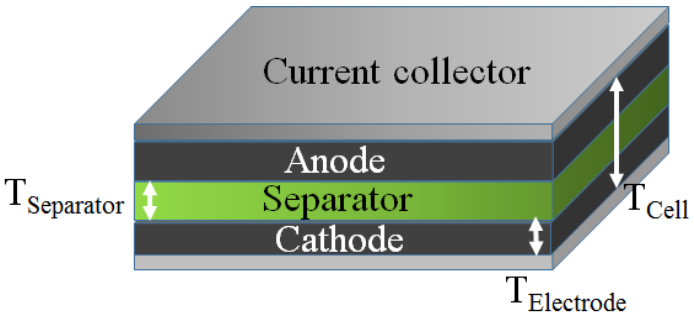

Figure 4.1. Schematic Illustration of Typical Lithium-ion Battery/supercapacitor Electrode. The cell is assembled is layer by layer with indication of thickness of cell (T_{Cell}), separator ($T_{Separator}$) and electrode ($T_{Electrode}$).

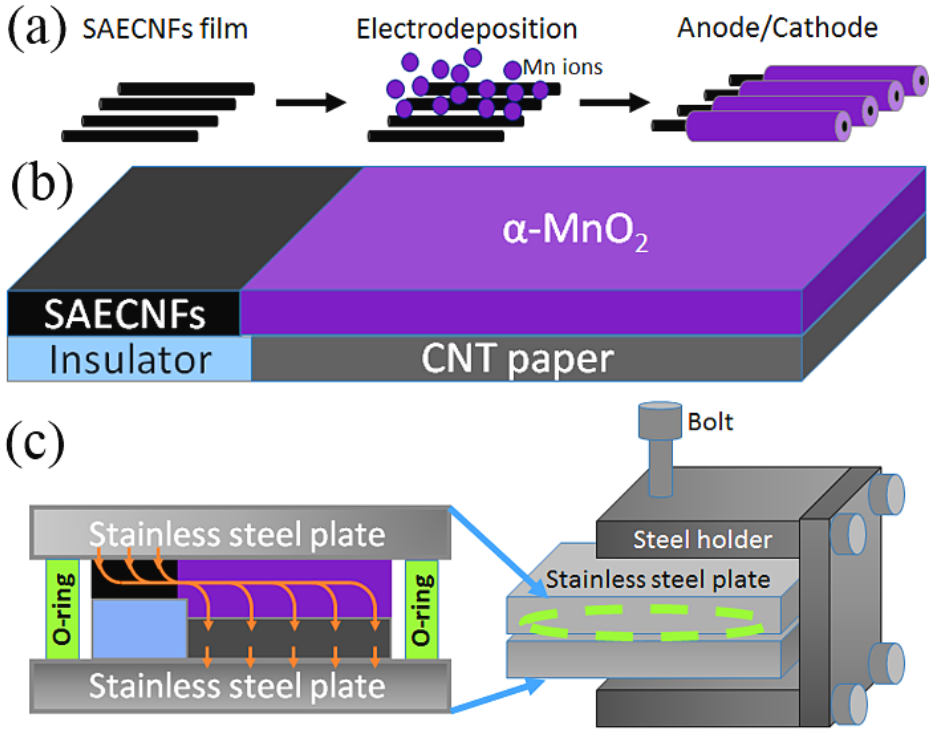

Figure 4.2. Schematic Processes of Electrodeposition of MnO_2 on SA-ECNFs as a Cathode (a). Counter with CNT paper anode as an asymmetrical cell (b) and schematic illustration of a self-sustainable separator-free supercapacitor configuration consisting of anode, cathode, current collectors and cell holder (c). (Orange arrows indicate the electron flows inside the cell)

Figure 4.2a-c illustrate a non-separator design consisting of MnO_2/SA-ECNFs hybrid film as a cathode, CNT paper as an anode and insulator to prevent undesired circuit electron flows. Modified half-film electrochemical deposition method along with an insulator setup was used to better analyze the electrochemical performance of this configuration. Note that the orange arrows display electron flows from current collector on the cathode side to the other side (Figure 4.2b). The device assembly is described as follows. The SA-ECNF film was cut into 2×1 cm^2 pieces and half-immersed in the electrolyte for electrodeposition. The as-prepared MnO_2/SA-ECNFs hybrid film, CNT paper, and insulator were transfer into a glovebox then were assembled in a standard testing platform (Figure 4.2c).[22] The thicknesses of these films were carefully measured to ensure the good contact between the current collector and electrodes (Figure 4.3).

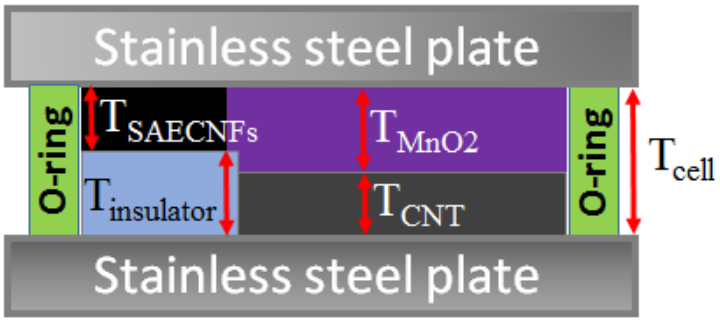

Figure 4.3. Schematic Illustration of the Self-sustainable Separator-free Configuration. It includeS stainless steel plates as current collector, MnO_2/SA-ECNFs as cathode, CNT paper as anode, insulator to prevent undesired current flow, and rubber O-ring. Red double-headed arrows indicating T_{cell} is 260 µm ± 70 µm, $T_{SA\text{-}ECNFs}$ is 80 µm ± 27 µm, T_{MnO2} is 120 µm ± 35 µm, $T_{insulator}$ is around 170 µm, and T_{CNT} is 110 ± 15 µm.

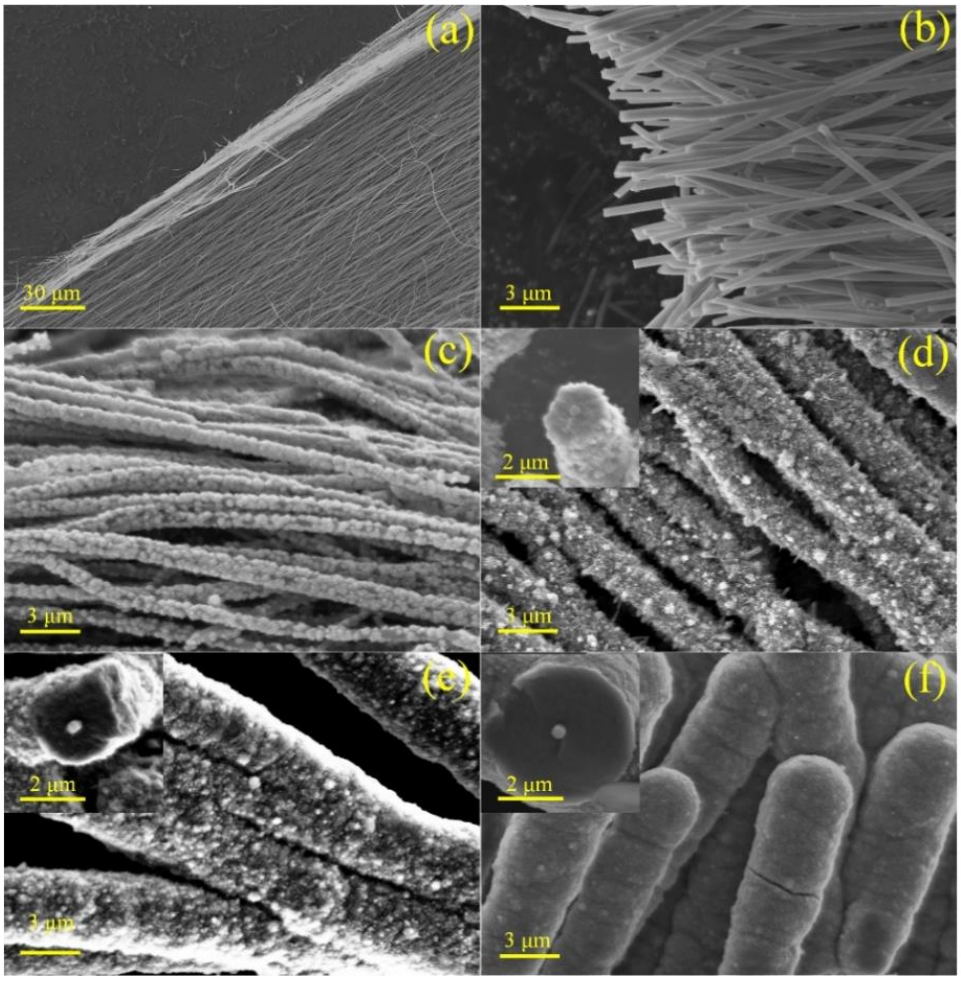

Figure 4.4. SEM Images of SA-ECNFs (a-b) and MnO_2/SA-ECNFs (c-f) for Different Electrodeposition Conditions. Insets are enlarged images to show the MnO_2 coating on SA-ECNFs films (c-f).

Table 4.1. Electrochemical Deposition Settings of SA-ECNFs at Different Current (20 µA – 80 µA) and Different Times (0.5 h – 12 h). Highlighted cells are the deposition times at which MnO_2 mass loadings were reaching the limit at different currents (the mass loading as Figure 4.15 shows).

Current (µA)	Time (h)							
20 µA	1	2	3	4	6	8	10	12
40µA	0.5	1	1.5	2	3	4	5	6
60 µA	0.5	1	1.5	2	3	4		
80 µA	0.5	1	1.5	2	2.5	3		

Figure 4.4ab shows the low and high magnification scanning electron microscopy (SEM) images. The as-prepared pure SA-ECNFs are aligned in an ordered structure. Our recent study indicates that the alignment of ECNFs can lead to a more uniform electrodeposition process. Furthermore, it is concluded that the growth of MnO_2 on SA-ECNFs follows a three-steps mechanism based on the electrodeposition time under an electrodeposition current of 40 μA. Therefore, various low currents (from 20 μA to 80 μA) were applied by an electrochemical workstation for different time ranging from 0.5 h to 12 h to reach the maximum film thickness (details in Table 4.1). The composites' structure and morphology were characterized by SEM (Figure 4.4c-f, Figure 4.5).

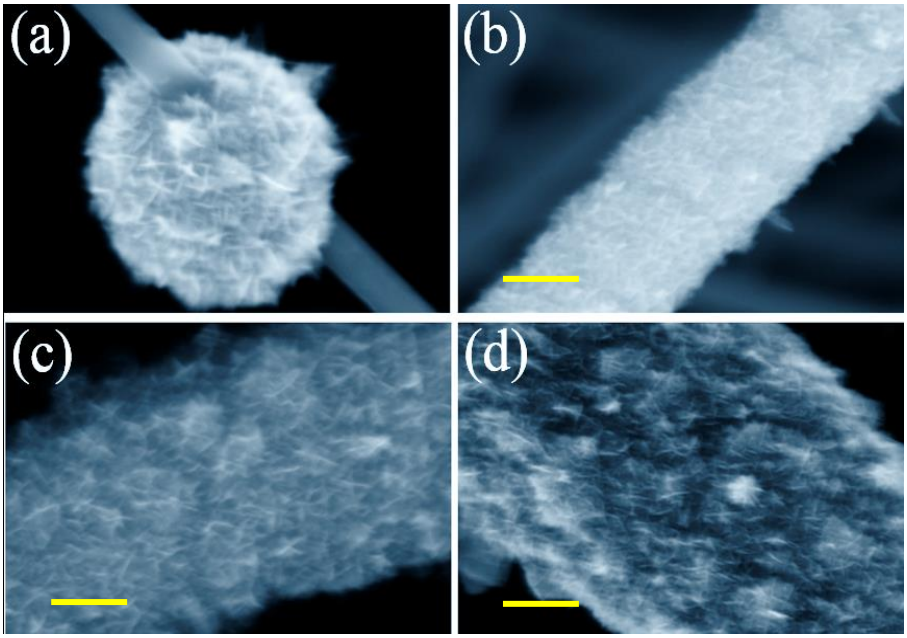

Figure 4.5. SEM Images show the Detailed Structures of MnO_2 on SA-ECNFs at Different Electrodeposition Currents of 20 μA (a), 40 μA (b), 60 μA (c) and 80 μA (d) Under Electrodeposition for 12 h, 4 h, 3 h, and 2.5 h, Respectively. (scale bars are 1 μm)

As discussed in our recent study, MnO_2 keeps growing as electrodeposition time increases until growth stop at a certain time point. A similar mechanism was observed at different deposition current from 20 μA to 80 μA (Figure 4.4c-f). MnO_2 stops growing when the SA-ECNFs surface was mostly covered with MnO_2 clusters at 20 μA electrodeposition while currents higher than 40 μA leading to a thick coating. That is probably due to the increasing resistance on the MnO_2-electrolyte interface. The 20 μA electrodeposition could not achieve a uniform coating (Figure 4.4c). When the electrodeposition current was higher than 20 μA, the current flow could keep depositing MnO_2 onto SA-ECNFs after all activation sites were occupied. Clusters merge with one another to form small balls around the SA-ECNFs then the "kebab"-like structures keep growing until the fibers are fully covered. Figure 4.4d-f show the fully covered structure of MnO_2/SA-ECNFs with single layer thicknesses ranging from 897 nm to 1971 nm under a current ranging from 40 μA to 80 μA.

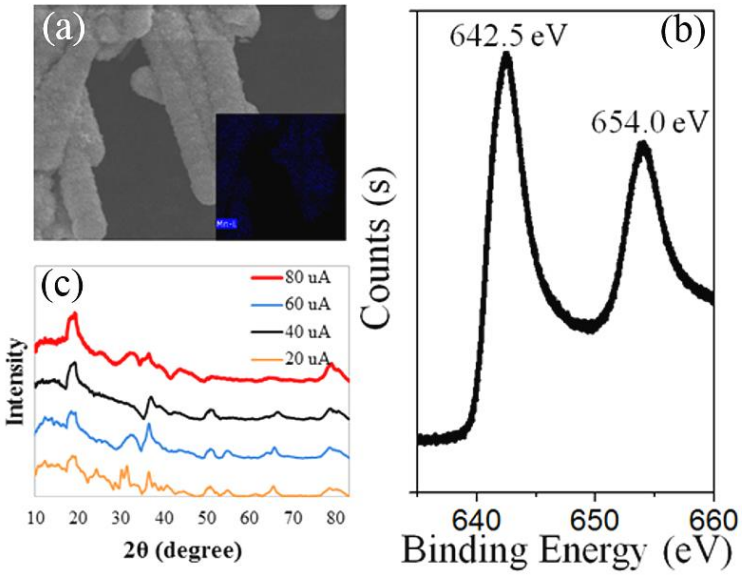

Figure 4.6. (a) SEM Associated with EDX Mapping Analysis. (b) XPS spectrum of Mn signal of the MnO_2/SA-ECNFs at 40 μA electrodeposition for 4 h. (c) XRD analysis of the MnO_2/SA-ECNFs at 20 μA, 40 μA, 60 μA and 80 μA electrodeposition for 12 h, 4 h, 3 h, and 2.5 h, respectively.

The as-prepared MnO_2/SA-ECNFs films were also been characterized to study their chemical composition. The energy dispersive X-ray (EDX) spectrum (Figure 4.6a, Figure 4.7) show that the surface composition of the electrochemically deposited electrodes is composed of the elements C, O, and Mn. The atomic ratio of O and Mn is close to 2:1, which implies the formation of MnO_2. The chemical composition of the MnO_2/SA-ECNFs sample was also investigated by X-ray Photoelectron Spectroscopy (XPS). The high-resolution Mn 2p spectra for MnO_2/SA-ECNFs is presented in Figure 4.6b. Two strong peaks at 642.5 and 654.0 eV can be clearly seen, corresponding to the Mn $2p_{3/2}$ and Mn $2p_{1/2}$ spin–orbit peaks of MnO_2, respectively.[23,24] The pronounced peak in the O 1s XPS spectrum (Figure 4.8) at 530.3 eV is assigned to Mn−O−Mn in the composite, and the peak

at 531.2 eV can be assigned to Mn-OH formation.[25,26] To investigate the MnO_2 crystal structure, the as-prepared MnO_2/SA-ECNFs materials were examined by X-ray diffraction (XRD) (Figure 4.6c). Compared to the results of SA-ECNFs only (Figure 4.9), The XRD patterns could be fully indexed to α-MnO_2 (JCPDS No. 44-0141),[27] and become more distinct with higher electrodeposition current. Hence the MnO_2 film is dominant with α-MnO_2 crystal structure.

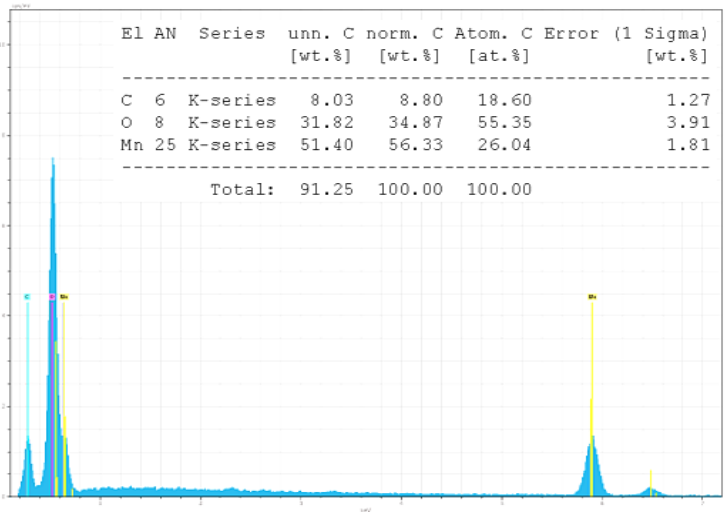

Figure 4.7. EDX of MnO_2-ECNFs After Electrodeposition for 4 Hours at 40 μA. The atom% of C, O and Mn is 18.60%, 55.35%, 26.04% respectively.

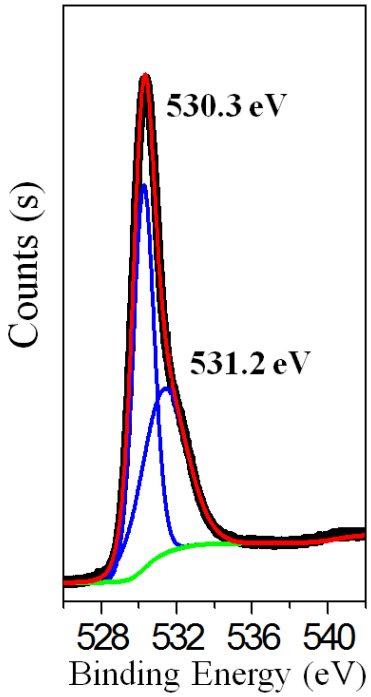

Figure 4.8. XPS Spectrum of the MnO_2/SA-ECNFs at 40 μA Electrodeposition for 4 h. Two strong peaks of O 1s XPS spectrum at 530.3 eV and 531.2 eV can be clearly seen, can be assigned to Mn−O−Mn in the composite, and to Mn-OH formation, respectively.

The resistance of MnO_2/SA-ECNFs electrodes with 40 μA (charge transfer resistance of about 330 Ohms), 60 μA (charge transfer resistance of about 511 Ohms) and 80 μA (charge transfer resistance of about 709 Ohms) electrodeposition was deduced from the electrochemical impedance spectroscopy (EIS) Nyquist plots from 100 kHz to 0.01 Hz (Figure 4.10a) and a Randles circuit model. These plots consist of a semicircle in the high-frequency region, which display an increase in charge transfer resistance with an increase in electrodeposition current.[28,29]

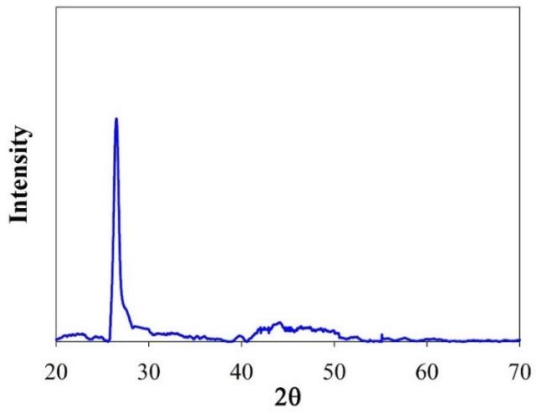

Figure 4.9. XRD Spectrum of the Pure SA-ECNFs.

Galvanic charge-discharge tests of different electrodes were performed at current densities of 2.5 A/g, 5 A/g and 10 A/g with of the configuration using MnO_2/SA-ECNFs electrodes without the use of cellulose separator in the supercapacitor prototype. The results are shown in Figure 4b-f. Note that cyclic voltammetry tests (Figure S9) of the electrodes were also conducted in a three-electrode cell (an Au electrode taped with MnO_2/SA-ECNFs, platinum wire, and Ag/AgCl were used as working electrode, counter electrode, and reference electrode, respectively). Shortcut happens during the charge-discharge of the 20 μA electrode in the separator free configuration testing due to the less thickness of MnO_2. The capacitance of the MnO_2/SA-ECNFs with 40 μA, 60 μA and 80 μA deposition is 141 F/g, 69 F/g, 38 F/g, respectively. And the energy density is 45.2 Wh/kg, 22.7 Wh/kg, and 12.1 Wh/kg, respectively. Note that a higher deposition current (MnO_2 thickness) leads to lower specific capacitance and energy density, which is in accordance with a reported phenomenon of high mass loading of MnO_2[18] A shape change of bulged

triangle to concaved triangle between the MnO_2/SA-ECNFs with 40 µA and 60 µA/80 µA deposition was observed, it may correlate to the resistance incensement based on other reports of MnO_2 hybrid electrodes.[14,41-43]

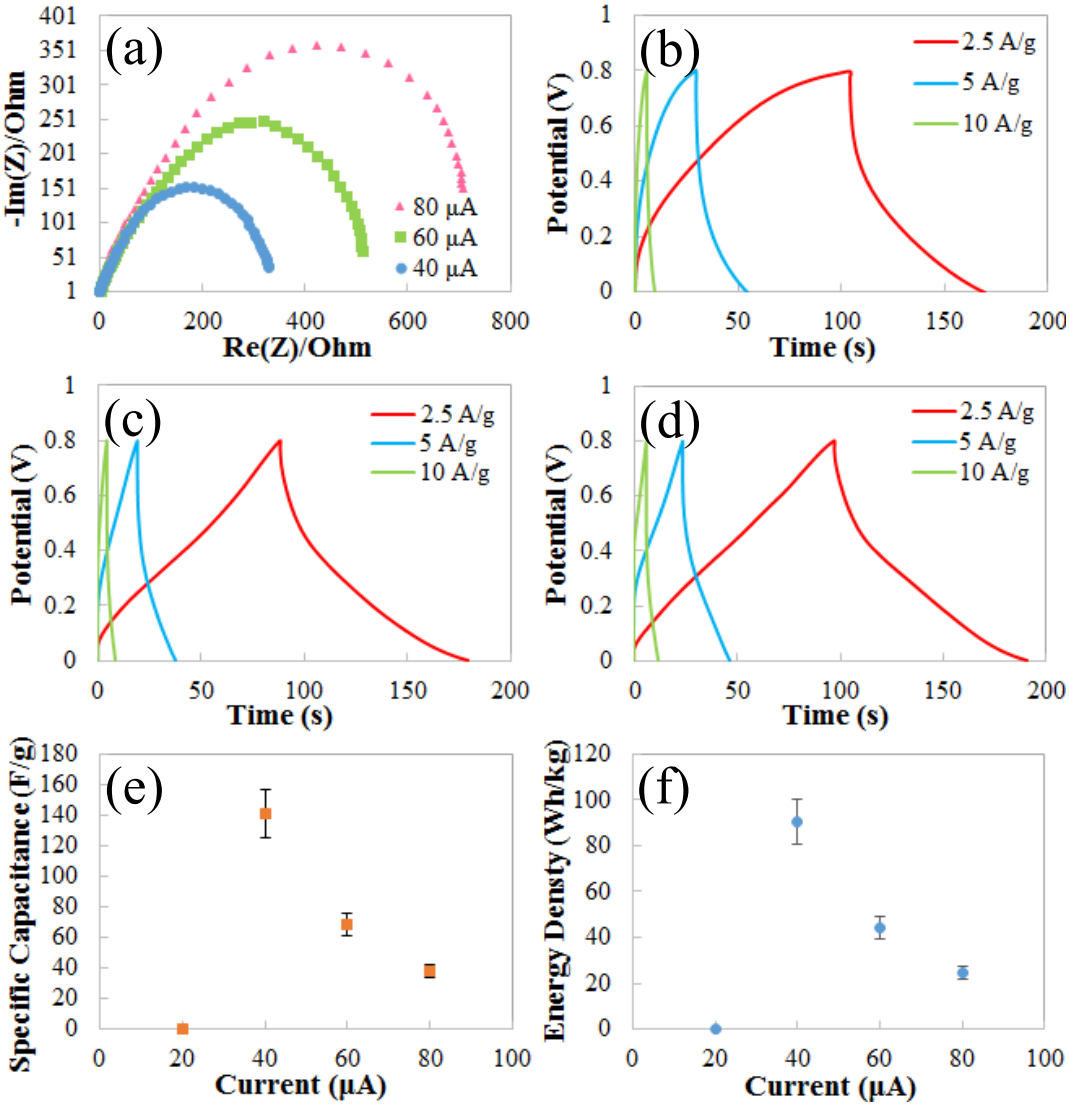

Figure 4.10. Electrochemical Characterization of the Electrodes without Separator. EIS from 100 kHz to 0.01 Hz (a) and galvanic charge-discharge profiles at different current density (2.5 A/g, 5 A/g and 10 A/g) of MnO_2/SA-ECNFs under 40 µA (b) 60 µA (c) and 80 µA (d) electrodeposition; and their energy storage performance: specific capacitance (e) and energy density (f).

Shortcut happens during the charge-discharge of the 20 μA electrode in the separator free configuration testing due to the less thickness of MnO_2. The capacitance of the MnO_2/SA-ECNFs with 40 μA, 60 μA and 80 μA deposition is 141 F/g, 69 F/g, 38 F/g, respectively. And the energy density is 45.2 Wh/kg, 22.7 Wh/kg, and 12.1 Wh/kg.

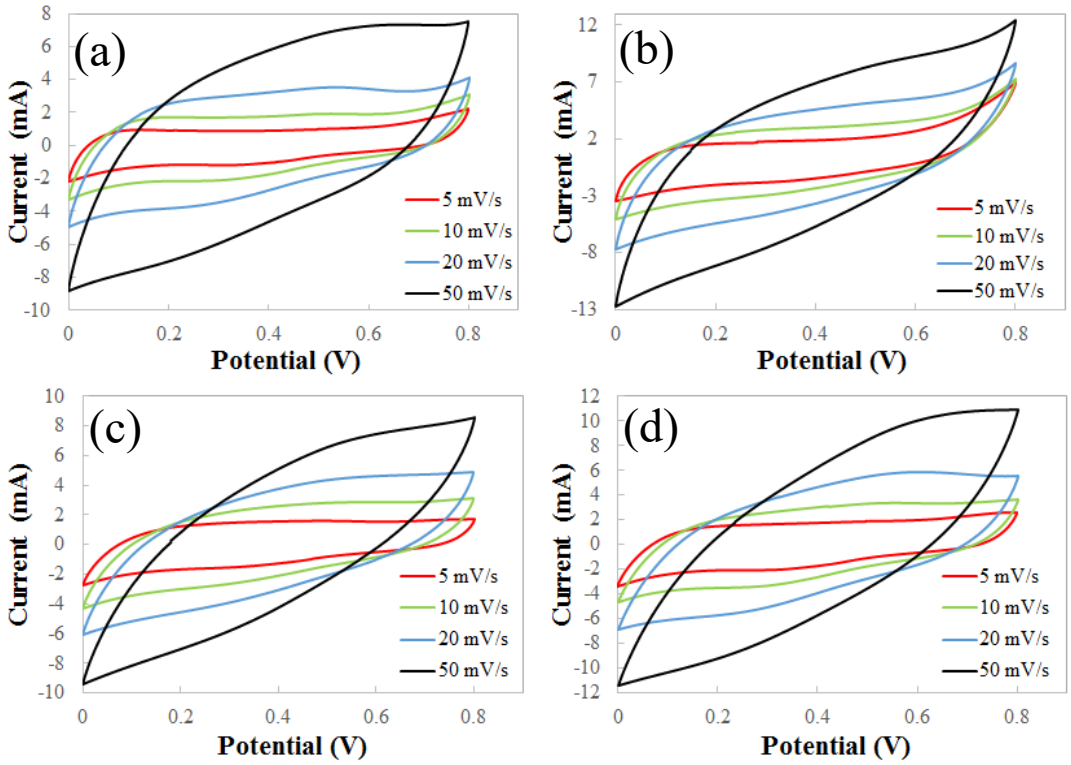

Figure 4.11. Cyclic Voltammetry Tests of the 20 μA, 40 μA, 60 μA and 80 μA MnO_2/SA-ECNFs Films Under 12 h, 4 h, 3 h and 2.5 h Deposition, Respectively.

The pseudo-capacitance depends on the reversible redox reactions between Mn(IV)/Mn(III) species and K^+ intercalation/de-intercalation at the MnO_2/electrolyte interfaces.[30-32]

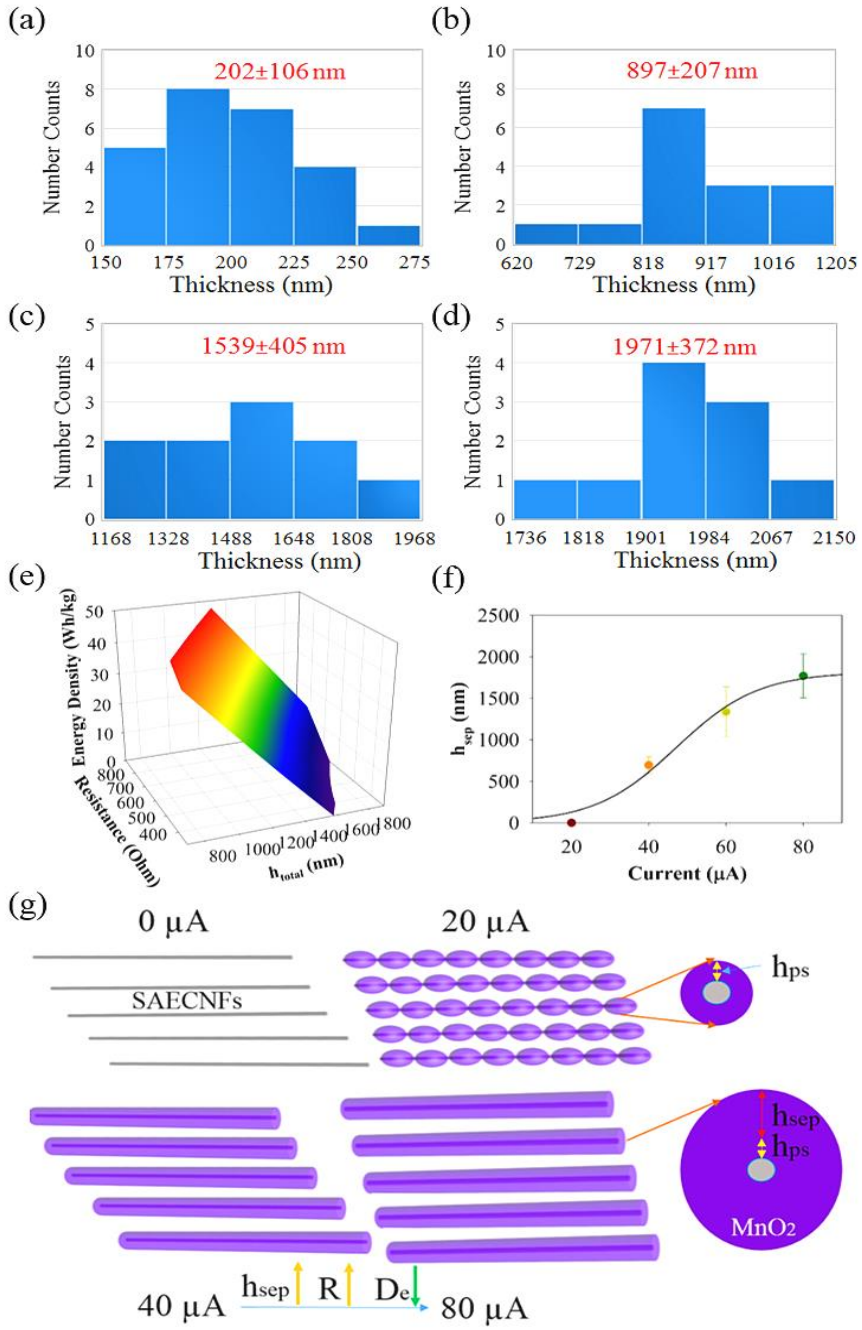

Figure 4.12. Histograms of MnO_2 Saturation Thickness (h_{total}) Distribution of 20 μA-12 h (a), 40 μA-4 h (b), 60 μA-3 h (c), and 80 μA-2.5 h (d) Electrodes. (e) 3D plot of the correlation of the energy density (D_e) with resistance and MnO_2 saturation thickness. (f) The dependence of MnO_2 thickness as a separator role (h_{sep}) on the electrodeposition current. (g) A schematic description of MnO_2 thickness as a pseudocapatance role (h_{ps}) and as a separator role (h_{sep}).

After a competing retention test at a current density of 2.5 A/g with and without the use of cellulose separator, the non-separator configuration shows an acceptable loss of energy density (Figure 4.13). Therefore, we concluded that the electrodeposition with 40 μA current results in a relatively thick MnO_2 dielectric layer while keeping a high energy density, which is able to survive 500 charge-discharge cycles without the use of a separator.

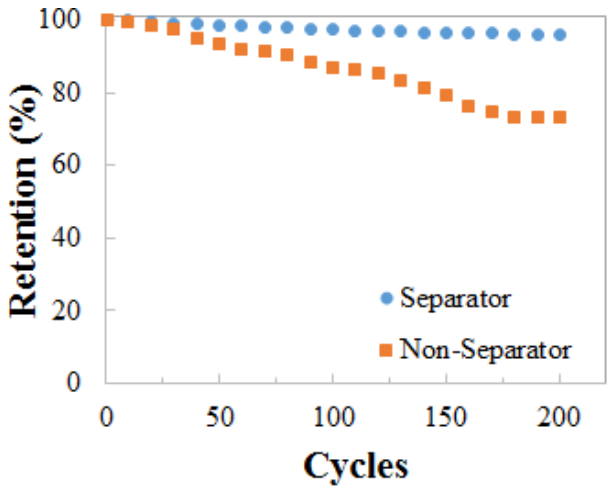

Figure 4.13. Retention Studies of MnO_2/SA-ECNFs at 40 μA Under 4 h Deposition with and without the Installation of a Typical Cellulous Separator.

As an outstanding type of carbon fibers, SA-ECNFs have a horizontally aligned structure, which highly facilitates the electron flow through the fiber arrays for a uniform electrodeposition. SA-ECNFs with diameters of 305 ± 53 nm (Figure 4.14) were synthesized with a standard electrospinning method followed with stabilization and carbonization.[33] Then preferred MnO_2 can be deposited onto the SA-ECNFs to form a thick layer and its thickness (Figure 4.12 a-d) and mass (Figure 4.15) were measured.

According to the measured resistance (Figure 4.10a) and calculated energy density above, higher MnO_2 saturation thickness (h_{total}) leads to larger resistance (directly) and lower energy density (indirectly) (Figure 4.12e). For the first time, we found the relationship between the thickness of deposited metal oxide and energy density generated from the electrode. To elucidate this, the important factor, h_{total}, should be divided into two parts: MnO_2 thickness as a pseudocapatance role (h_{ps}) and as a separator role (h_{sep}) (Figure 4.12 f,g). Herein, h_{ps} contributes to the reversible redox reactions between Mn(IV)/Mn(III) species and K^+ intercalation/de-intercalation at the MnO_2/electrolyte interfaces while h_{sep} applies high resistance between two electrodes while allowing free ions to flow. Furthermore, since the h_{sep} is ascribed to different electrodeposition currents, to balance the pseudocapacitance role with the separator role of MnO_2, an optimal electrodeposition current (I_{opt}) should be modeled. Considering the energy density (D_e) results, Figure 4.12f shows a best fit of the h_{sep} versus electrodeposition current data (I) by the equation:

$$h_{sep} = \frac{h_{sep}(\max)}{1 + e^{-\left(\frac{I - I_{opt}}{D_e}\right)}} \tag{4.3}$$

with an I_{opt} of about 47 μA, which highly supports our result of 40 μA-electrode achieving a highest energy density of 45.2 Wh/kg. Galvanic charge-discharge tests indicate MnO_2/SA-ECNFs electrodes with a separator exhibit higher specific capacitance and energy density (Figure S13). The data of figure S13 indicates there is an inverse

proportional relation between the energy losses and MnO_2 thickness. The energy losses can be ascribed to the deactivation of h_{ps}. In the absence of a separator, some of h_{ps} will be changed into h_{sep}, resulting in lower energy density. In our nest research, we will focus on the ratio of h_{sep}/h_{ps} change in the conditions of with/without a separator.

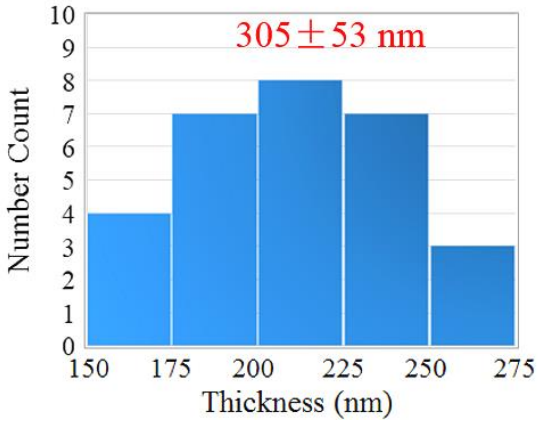

Figure 4.14. Bar Diagram of Analysis of Size Distribution of Pure SA-ECNFs with the Mean Thickness Value and Error.

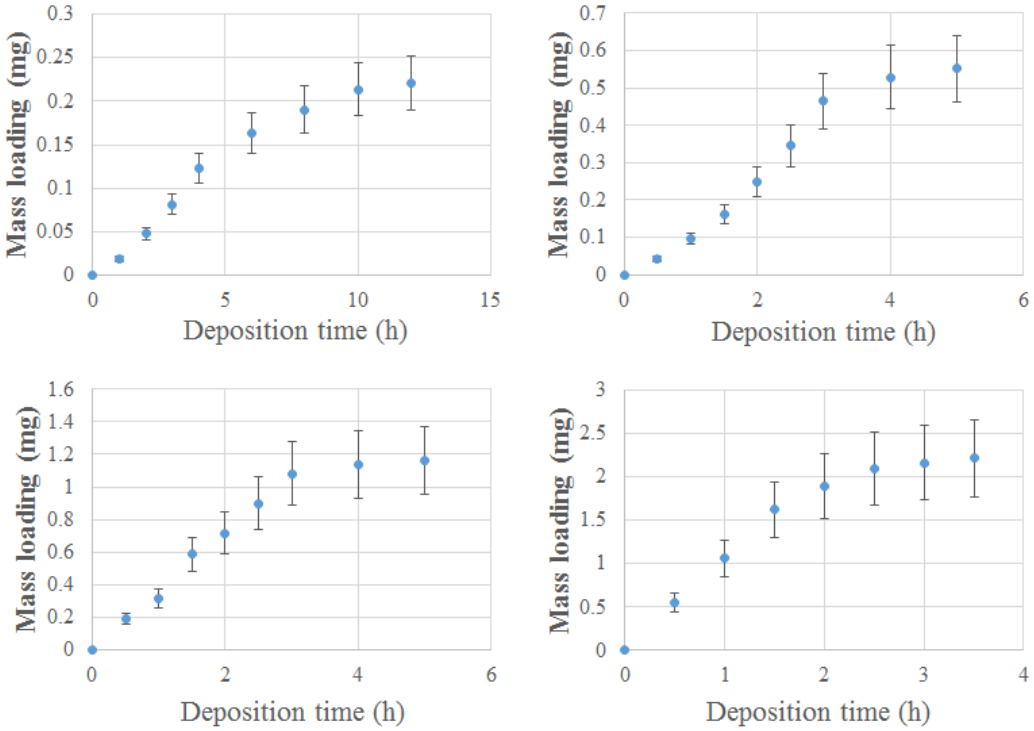

Figure 4.15. Mass Loading of SA-ECNFs at 20 μA, 40 μA, 60 μA and 80 μA Under Different Deposition Time with Error Bar.

IV.VIII Conclusions

This work demonstrates a novel configuration of supercapacitor free of separator by uniformly electrodepositing MnO_2 on aligned SA-ECNFs and the feasibility of MnO_2 layer functioning as separator in different thickness with the electrodeposition current was explored. From the electrochemical performance, MnO_2/SA-ECNFs with 40 μA electrodeposition display a high capacitance of 141 F/g and a specific energy density of 45.2 Wh/kg. This research presents a potential revolution of traditional metal oxide/carbonaceous nanomaterial-based pseudocapacitance energy storage by simply

increasing the thickness of the metal oxide as replacement of a separator to reduce the manufacturing process for practical applications.

IV.IX References

[1] Burke, A. Journal of power sources **2000,** 91, (1), 37-50.

[2] Miller, J. R.; Burke, A. F. The Electrochemical Society Interface **2008,** 17, (1), 53.

[3] Zhang, L.; Yang, X.; Zhang, F.; Long, G.; Zhang, T.; Leng, K.; Zhang, Y.; Huang, Y.; Ma, Y.; Zhang, M. Journal of the American Chemical Society **2013,** 135, (15), 5921-5929.

[4] Wu, Y.; Zhang, T.; Zhang, F.; Wang, Y.; Ma, Y.; Huang, Y.; Liu, Y.; Chen, Y. Nano Energy **2012,** 1, (6), 820-827.

[5] Liu, Y.; Zeng, Z.; Wei, J. Frontiers in Nanoscience and Nanotechnology **2016,** 2, (2), 78-85.

[6] Zhu, G.; He, Z.; Chen, J.; Zhao, J.; Feng, X.; Ma, Y.; Fan, Q.; Wang, L.; Huang, W. Nanoscale **2014,** 6, (2), 1079-1085.

[7] Zeng, Z.; Liu, Y.; Zhang, W.; Chevva, H.; Wei, J. Journal of Power Sources **2017,** 358, 22-28.

[8] Liu, J.; Jiang, J.; Cheng, C.; Li, H.; Zhang, J.; Gong, H.; Fan, H. J. Advanced Materials **2011,** 23, (18), 2076-2081.

[9] Hu, L.; Chen, W.; Xie, X.; Liu, N.; Yang, Y.; Wu, H.; Yao, Y.; Pasta, M.; Alshareef, H. N.; Cui, Y. Acs Nano **2011,** 5, (11), 8904-8913.

[10] Lv, P.; Feng, Y. Y.; Li, Y.; Feng, W. Journal of power sources **2012,** 220, 160-168.

[11] Hou, Y.; Cheng, Y.; Hobson, T.; Liu, J. Nano letters **2010,** 10, (7), 2727-2733.

[12] Cheng, Y.; Lu, S.; Zhang, H.; Varanasi, C. V.; Liu, J. Nano letters **2012,** 12, (8), 4206-4211.

[13] He, Y.; Chen, W.; Li, X.; Zhang, Z.; Fu, J.; Zhao, C.; Xie, E. ACS nano **2012,** 7, (1), 174-182.

[14] Lei, Z.; Zhang, J.; Zhao, X. Journal of Materials Chemistry **2012,** 22, (1), 153-160.

[15] Bélanger, D.; Brousse, L.; Long, J. W. The Electrochemical Society Interface **2008,** 17, (1), 49.

[16] Zhang, S. S. Journal of Power Sources **2007,** 164, (1), 351-364.

[17] Ozoemena, K. I.; Chen, S. Nanostructure science and technology **2016**.

[18] Subramania, A.; Sundaram, N. K.; Kumar, G. V. Journal of power sources **2006,** 153, (1), 177-182.

[19] Appetecchi, G.; Croce, F.; Scrosati, B. Journal of power sources **1997,** 66, (1), 77-82.

[20] Lang, X.; Hirata, A.; Fujita, T.; Chen, M. Nature Nanotechnology **2011,** 6, (4), 232-236.

[21] Chmiola, J.; Largeot, C.; Taberna, P.-L.; Simon, P.; Gogotsi, Y. Science **2010,** 328, (5977), 480-483.

[22] Lu, Y.; Zhang, F.; Zhang, T.; Leng, K.; Zhang, L.; Yang, X.; Ma, Y.; Huang, Y.; Zhang, M.; Chen, Y. Carbon **2013,** 63, (Supplement C), 508-516.

[23] Lee, S. W.; Kim, J.; Chen, S.; Hammond, P. T.; Shao-Horn, Y. ACS Nano **2010,** 4, (7), 3889-3896.

[24] Zilong, W.; Zhu, Z.; Qiu, J.; Yang, S. Journal of Materials Chemistry C **2014,** 2, (7), 1331-1336.

[25] Yuan, L.; Lu, X.-H.; Xiao, X.; Zhai, T.; Dai, J.; Zhang, F.; Hu, B.; Wang, X.; Gong, L.; Chen, J.; Hu, C.; Tong, Y.; Zhou, J.; Wang, Z. L. ACS Nano **2012,** 6, (1), 656-661.

[26] Wang, J.-G.; Yang, Y.; Huang, Z.-H.; Kang, F. Journal of Materials Chemistry **2012,** 22, (33), 16943-16949.

[27] Yu, P.; Zhang, X.; Wang, D.; Wang, L.; Ma, Y. Crystal Growth & Design **2009,** 9, (1), 528-533.

[28] Shang, C.; Dong, S.; Wang, S.; Xiao, D.; Han, P.; Wang, X.; Gu, L.; Cui, G. ACS Nano **2013,** 7, (6), 5430-5436.

[29] Xu, J.; Gai, S.; He, F.; Niu, N.; Gao, P.; Chen, Y.; Yang, P. Dalton Transactions **2014,** 43 (30), 11667-11675.

[30] Liu, C.; Yu, Z.; Neff, D.; Zhamu, A.; Jang, B. Z. Nano letters **2010,** 10, (12), 4863-4868.

[31] Fan, Z.; Yan, J.; Wei, T.; Zhi, L.; Ning, G.; Li, T.; Wei, F. Advanced Functional Materials **2011,** 21, (12), 2366-2375.

[32] Dong, X.; Wang, X.; Wang, J.; Song, H.; Li, X.; Wang, L.; Chan-Park, M. B.; Li, C. M.; Chen, P. Carbon **2012,** 50, (13), 4865-4870.

[33] Aboagye, A.; Elbohy, H.; Kelkar, A. D.; Qiao, Q.; Zai, J.; Qian, X.; Zhang, L. Nano Energy **2015,** 11, 550-556.

CHAPTER V

CONCLUDING REMARKS

Energy storage systems such as supercapacitors and lithium-ion battery have erupted in popularity due to their high energy/power density, low-toxicity, long lifecycles, and low cost. Supercapacitors and lithium-ion battery have been widely discovered in nanoscale synthesis, reaction, modification, structures and morphology control of cathode materials since the early 21st century. Upcoming demand will be focusing on new energy storage system (e.g. aluminum ion battery), growth mechanism of cathode materials (e.g. MnO_2, $LiMnO_2$, $LiCoO_2$), novel configurations (e.g. separator-free, current collector-free), magenetic enhancement, etc.

From this thesis work, the following conclusions can be drawn: (1) CNM-based structures, such as CNTF, TGF, ECNF, possess extensive options of chemical modification and optimal mechanical property, which are used as substrates to stabilize active MO layers. Among these candidates, ECNF combined with electrochemical deposition for pseudo-active materials coating is a promising route for synthesizing large-scale energy storage cells with high performance and low cost. (2) A new strategy for uniformly electrodepositing MnO_2 on aligned ECNFs and the change in the mechanism of MnO_2 growth with the electrodeposition time was demonstrated. In contrast to earlier studies with

a much higher current, the reported electrodeposition was conducted with a constant low-current of 40 μA. Film growth proceeds by a three-stage kinetic process with a halfway growth time of 2.78 h. These findings represent a significant improvement in stable metal oxide/carbonaceous nanomaterial-based pseudocapacitance energy storage. (3) In summary, after applying 1.34 mT magnetic field, MnO_2/ECNFs showed enhanced magneto-capacitance of 141.7 F/g at the cyclic voltage sweeping rates of 5 mV/s. The capacitance of MnO_2/ECNFs was increased by 58.1% at the current density of 0.5 A/g during the galvanostatic charge/discharge test. Meanwhile, in the presence of 1.34 mT magnetic field, the magneto-supercapacitor presented "low resistance shift" for bulk electrolyte and the MnO_2/ECNFs electrode. Longer charge/discharge time of the electrode is observed under magnetic field than that without magnetic field, while did not sacrifice its lifecycle stability. The insightful discussion of the potential mechanism suggests that the magneto-supercapacitance enhancement can be primarily attributed to the magnetic susceptibility of MnO_2 induced electron spin energy degeneracy for facilitated electron transfer reaction, the magnetohydrodynamic impact on electrolyte transportation and improved cation intercalation/de-intercalation under the mT magnetic field, thus resulting in higher charge density at the electrode/electrolyte interfaces, thicker double layer, and lower internal resistance. This study may pave a way to the development of sustainable metal oxide-based supercapacitors with magneto-capacitance enhancement by applying a low magnetic field. (4) A novel configuration of supercapacitor free of separator by

uniformly electrodepositing MnO_2 on aligned SAECNFs and the feasibility of MnO_2 layer functioning as a separator in different thickness with the electrodeposition current was demonstrated. This research presents a potential revolution of traditional metal oxide/carbonaceous nanomaterial-based pseudocapacitance energy storage by simply increasing the thickness of the metal oxide as replacement of a separator to reduce the manufacturing process for practical applications.